A SYSTEMATIC EVALUATION OF COBALT-FREE NICKEL-RICH CORE-SHELL STRUCTURED POSITIVE ELECTRODE MATERIALS

by

Yulong Liu

Submitted in partial fulfilment of the requirements
for the degree of Doctor of Philosophy

at

Dalhousie University
Halifax, Nova Scotia
January 2022

Dalhousie University is located in Mi'kma'ki,
the ancestral and unceded territory of the Mi'kmaq.
We are all Treaty people.

To the end of a journey

Table of Content

List of Tables

List of Figures

Abstract

Layered Co-free Ni-rich (>80%) oxide positive electrode materials have attracted significant attention in recent years due to the high demand for lower cost and higher energy density lithium-ion batteries. The main difficulty in the development of high specific capacity Ni-rich materials primarily lies in obtaining excellent charge-discharge cycle life. Utilizing a core-shell structure with a Ni-rich core and a lower Ni content shell can be an excellent design strategy to balance specific capacity and cycle life. A low Ni content shell of long cycle life may prevent direct electrolyte contact with the high specific capacity Ni-rich core, enabling the core-shell material to have improved cycle life compared to the Ni-rich core alone.

The first part of the thesis explores a systematic series of Co-free Ni-rich core-shell materials with various core/shell compositions, core diameters, shell thickness and lithiation temperatures. A relationship between the cycling performance of core-shell materials and the lithiation temperature during synthesis is proposed which considers the crystallinity of the material, the average percentage of Ni in the Li layer and the presence or absence of the shell phase after the heating step. The “best” core-shell material demonstrates comparable performance with commercial-grade Co-containing materials in terms of capacity retention, powder electrical resistance and cell internal impedance, highlighting the potential of Co-free core-shell materials as promising alternative positive electrode materials.

The second part of the thesis focuses on the evaluation of the “best” core-shell material in commercial-grade pouch cells. Two versions of the core-shell material, washed and unwashed, were obtained from a reputable vendor. The charge-discharge cycling performance of the core-shell pouch cells is worse than commercial-grade single crystal $LiNi_{0.8}Mn_{0.1}Co_{0.1}O_2$ and $LiNi_{0.5}Mn_{0.3}Co_{0.2}O_2$ cells in terms of capacity retention and impedance growth. Cross-section SEM/EDS showed particle microcracking of core-shell materials due to calendering which is detrimental to the cell performance. Washing core-shell materials worsened the mechanical and electrochemical performance of the material.

List of Abbreviations and Symbols Used

AG	Artificial graphite
ARC	Accelerating rate calorimetry
BET	Brunauer-Emmett-Teller
CCCV	Constant current constant voltage
CMC	Carboxyl methyl cellulose
C	C as in C-rate
CS	Core shell
d	Interlayer spacing
DCR	Direct current resistance
DEC	Diethyl carbonate
DMC	Dimethyl carbonate
DTD	Ethylene sulfate
EC	Ethylene carbonate
EDS	Energy dispersive *X*-ray spectroscopy
EIS	Electrochemical impedance spectroscopy
EMC	Ethyl methyl carbonate
F	Structural factor
f	Atomic scattering factor
FEC	Fluoroethylene carbonate
FM	Formation
FWHM	Full width half max
HF	Hydrogen fluoride
(*hkl*)	Miller indices
HWS	Heat-wait-search
IRC	Irreversible capacity
λ	Wavelength
LDH	Layered double hydroxide
LFO	Lithium difluorophosphate
LFP	Lithium iron phosphate
$LiBF_4$	Lithium tetrafluoroborate
LiBOB	Lithium bix(oxalate)borate
$LiPF_6$	Lithium hexfluorophosphate
LiTFSi	Lithium bis(trifluoromethanesulfonyl)imide
LMO_2	Lithium metal oxide
LUMO	Lowest unoccupied molecular orbital
MA	Methyl acetate
NCA	$Li[Ni_{0.8}Co_xAl_{0.2-x}]O_2$
Ni_{Li}	Ni atom in the Li layer

NMC	Lithium nickel manganese cobalt oxide
NMP	N-methyl-2-pyrrolidone
OCV	Open circuit voltage
ODTO	1,2,6 – oxadithiane 2,2,6,6 – tetraoxide
PC622	Polycrystal $Li[Ni_{0.6}Co_{0.2}Mn_{0.2}]O_2$
PC811	Polycrystal $Li[Ni_{0.8}Co_{0.1}Mn_{0.1}]O_2$
PVDF	Polyvinylidene fluoride
Q	Capacity
R_b	Bragg R factor
R_{ct}	Charge-transfer resistance
SBR	Styrene butadiene rubber
SC532	Single crystal $Li[Ni_{0.5}Mn_{0.3}Co_{0.2}]O_2$
SC811	Single crystal $Li[Ni_{0.8}Co_{0.1}Mn_{0.1}]O_2$
SEI	Solid electrolyte interphase
SEM	Scanning electron microscopy
SHR	Self-heating rate
SOC	State of charge
UCV	Upper cut-off voltage
VC	Vinylene carbonate
ΔV	Voltage polarization
XPS	*X*-ray photoelectron spectroscopy
XRD	*X*-ray diffraction
(*xyz*)	Fractional atomic position

Acknowledgements

This thesis cannot be completed without the help of many people.

I would like to gratefully thank Dr. Haohan Wu from Hunan Zoomwe for providing all the commercial grade precursors. I want to give my sincere thanks to Chad Bowling and Dr. Jim Li from Tesla Inc. for material scaling up and LiFun Technology Dr. Jian Tu and Dr. Xiongwen Xu who made the pouch cells and suggested the oxalic acid slurry formulation. I would like to thank Dr. Obrovac for using his ion-milling machine. I'm indebted to Divya Rathore and Dongxu Ouyang who directly contributed to this work especially during Covid outbreak in Nova Scotia. I would like to thank Michel Johnson and Patricia Scallion for their technical support. I would like to thank my committee members Dr. Ian Hill and Dr. Kermanshahi-pour as well as all the staff from both Physics and Chemical Engineering Departments for their help and support. I want to gratefully acknowledge all the Dahn group members for the great working environment and being so supportive. I want to say thank you to my supervisor Dr. Jeff Dahn for his tremendous support and guidance throughout my Ph.D study. I feel very privileged to have such an excellent opportunity to build pouch cells with my own material. Years I spent in the Dahn lab will stay as one of the most memorable parts of my life.

Last but not the least, I would like to thank my parents, aunt May and uncle Evan, cousin Helena for their support over the years and my girlfriend Jingting for staying with me during Covid.

Chapter 1 Introduction

1.1 Motivation

In the past decade, battery technology has been identified as a crucial enabler to reduce the dependency on fossil fuel and accelerate the transition to renewable energy.[1,2] The lithium-ion battery presents a potential candidate to be such an enabler due to its high energy density, excellent rate capability and relatively long life time, compared to other types of batteries such as lead-acid, nickel cadmium, nickel metal hydride, etc.[1,2] Encouraged by all its merits, currently lithium-ion batteries have been widely adopted as power sources for portable devices and electric vehicles, and are expected to be massively used as energy storage devices for intermittent energy sources such as wind and solar energy. The lithium-ion battery has experienced a rapid cost reduction per kWh largely due to the upscaling of production and the advancement of automation and manufacturing processing in the industry during recent years.[3–5] However, a further cost reduction of lithium-ion batteries, as well as a simultaneous improvement of energy density and life time, is still highly desirable for an even broader market adoption as sustainable power source and energy storage device.

From an academic standpoint, energy density increase, life time improvement and cost reduction can be tackled from various aspects. To increase the energy density of a lithium-ion cell, the most straightforward method is to simply increase the upper cut-off voltage when sufficient negative electrode capacity is provided. An electrolyte blend must be carefully chosen to lower the side reactions between the positive electrode material and the electrolyte so that a lithium-ion cell can obtain acceptable lifetime even when charged to a high voltage. The Ni-rich Co-free layered lithium metal oxide positive electrode materials provide another options to further increase the energy density because of their high specific capacities. There are many reasons to eliminate Co, such as its scarcity, high price and the use of child labor during Co mining.[6,7] The use of cheaper Ni to replace Co also helps lower the cost of lithium-ion cells. However, though Ni-rich materials bring higher specific capacity, the charge-discharge capacity retention of Ni-

rich materials is inferior which calls for a cost-effective method to improve the capacity retention of Ni-rich materials.[8,9] Reducing the number of steps in large-scale material production is also very beneficial to lower the cost of a lithium-ion cell. Typical production of Ni-rich materials requires a washing/reheating step to remove surface lithium residuals that cause slurry gelation.[10,11] A method to solve the slurry gelation problem caused by the unwashed Ni-rich material will be highly desirable.

This Ph.D work focused on the development of Ni-rich Co-free core-shell positive electrode materials as a method to increase the energy density and lower the cost of a lithium ion cell. The use of core-shell structure with a Ni-rich core and a lower Ni content shell is expected to retain the high specific capacity of the Ni-rich material but with improved capacity retention due to the lower Ni content shell. The elimination of Co also allows for a cost reduction compared to other Ni-rich Co-containing materials. One of the best core-shell materials developed was further evaluated in commercial-grade pouch cells and its performance was compared to single crystal $LiNi_{0.5}Mn_{0.3}Co_{0.2}O_2$ (SC532) and $LiNi_{0.8}Mn_{0.1}Co_{0.1}O_2$ (SC811). Lastly, the use of oxalic acid to solve the slurry gelation problem from the unwashed core-shell material was explored and the performance was evaluated and compared with the washed material in pouch cells with various electrolyte blends.

1.2 Thesis Outline

Chapter 1 of this thesis gives a general introduction to the lithium-ion cell and its major components. Chapter 2 provides a brief literature review on the Ni-rich Co-free core-shell positive electrode materials, the washing/reheating impact on the Ni-rich materials, and the electrolyte additives used in the Ni-rich Co-free core-shell pouch cells for long-term charge-discharge cycling. Chapter 3 describes the experimental methodology and the apparatus/equipment used to complete this Ph.D work.

Chapter 4 provides a preliminary investigation of three Ni-rich Co-free hydroxide core-shell precursors that were lithiated at various temperatures and then examined physically

and electrochemically. The lithiated materials were compared to the corresponding uniform “core” and “shell” materials lithiated at the same temperatures.

Chapter 5 focuses on a comparison of the “best” core-shell material from Chapter 4 with some commercial-grade Ni-rich Co-containing materials in terms of the charge-discharge cycling performance, electrical resistivity, and direct current resistance (DCR), suggesting that Co may not be essential.

Chapter 6 presents a screening of a wide range of Co-free Ni-rich core-shell precursors with different core/shell compositions, core sizes and shell thicknesses heated at various temperatures. In all cases, the shell phase had a larger Mn content than the core phase. A relationship between the cycling performance and heating temperature was proposed. The reactivity of the charged material with electrolyte was also explored.

Chapter 7 examines the impact of washing on the best core-shell material. The physical and electrochemical performance of the washed and unwashed powder was compared. Their charge-discharge cycling performance and gas formation during cycling were also compared in commercial-grade pouch cells.

Chapter 8 compares the charge-discharge cycling performance of pouch cells with single crystal $LiNi_{0.5}Mn_{0.3}Co_{0.2}O_2$ (SC532), $LiNi_{0.8}Mn_{0.1}Co_{0.1}O_2$ (SC811). and the washed best core-shell material made by a reputable vendor. Two upper cut-off voltages (UCVs) per cell type were chosen to either include or exclude the remnant of the “H2-H3 phase transition” region, if present, in each positive electrode material.

Chapter 9 concludes this thesis and proposes future work that might be of importance to the lithium-ion battery community.

1.3 Lithium-ion Cells

A lithium-ion battery is comprised of two or more lithium-ion cells connected in series and/or parallel. Figure 1.1 shows a schematic of a discharging lithium-ion cell (not to

scale) which consists of a positive electrode, a negative electrode and a separator (made of a microporous polyolefin) between them. All these components are porous and soaked by electrolyte.

Both the positive and negative electrodes are made by casting a slurry consisting of an active material, a conducting agent, a binder and solvent onto a current collector foil, followed by solvent evaporation. This process produces porous electrodes. Finally, the as-prepared electrodes are calendered to improve the coating/current collector contact and to shorten electron/ion transport pathway for better performance. Most importantly, the calender process allows one to pack more active material into the cell to increase its volumetric energy density. The typical active material of the positive electrode, such as a layered structure lithium metal oxide, and the negative electrode, typically graphite, will be discussed in detail in the next section. The conducting agent in the electrode is typically carbon black which helps to conduct electrons in the electrode during the cell charging and discharging. For the positive electrode, the typical binder and solvent are polyvinylidene fluoride (PvdF) and N-methylpyrrolidone (NMP), respectively. The typical binder and solvent used for the negative electrode are carboxyl methyl cellulose/ styrene butadiene rubber (CMC/SBR) and water, respectively. The current collector for the positive electrode is aluminum foil. The current collector for the graphite negative electrode is typically copper foil as using aluminum causes lithium alloying with aluminum at low voltage, leading to current collector pulverisation.[12]

Both the positive and negative electrode active materials are lithium-ion hosts that allow lithium-ions to move in (intercalate) and out (detercalate) of the structure and, concurrently, combine (during Li-ion intercalation) and release (during Li-ion detercalation) electrons to maintain charge neutrality. During lithium-ion cell discharging, the lithium-ions detercalate from the negative electrode active material, typically graphite, and are carried by the electrolyte in the pores to the positive side. At the same time, electrons are released and move via the external circuit to power the load. Eventually, the lithium-ion and electrons meet on the positive side, and the lithium-ion is intercalated into the positive electrode active material, such as a transition metal oxide, which

completes the discharging process of a lithium-ion cell. The charging process follows the exact opposite path of the discharging process.

The half and overall reactions in lithium-ion cells with a layered structure transition metal oxide ($LiMO_2$) positive electrode and a graphite (C) negative electrode are as the follows:

Positive electrode reaction:

$$LiMO_2 \underset{dis.}{\overset{cha.}{\rightleftarrows}} xLi^+ + xe^- + Li_{1-x}MO_2 \qquad (1\text{-}1)$$

Negative electrode reaction:

$$yC + xe^- + xLi^+ \underset{dis.}{\overset{cha.}{\rightleftarrows}} yLi_{x/y}C \qquad (1\text{-}2)$$

Overall reaction:

$$LiMO_2 + yC \underset{dis.}{\overset{cha.}{\rightleftarrows}} Li_{1-x}MO_2 + yLi_{x/y}C \qquad (1\text{-}3)$$

In the above equations, the value of x is between 0 and 1. When x = 0, the layered structure transition metal oxide is fully lithiated and the graphite contains no lithium-ions, whereas when x = 1, the layered structure transition metal oxide has completely delithiated and the graphite can be fully lithiated, depending on the value of y.

The voltages of the positive and negative electrodes are also given by the corresponding degree of lithiation or delithiation given by x or x/y, respectively. When x = 0, the layered structure transition metal oxide has the lowest voltage, whereas when x = 1, the voltage is the highest. On the contrary, the graphite negative electrode has the lowest voltage when x/y = 1/6 and the highest voltage when x/y = 0.

The difference in the positive and negative electrode voltages determines the open circuit voltage of a "full cell" shown below.

$$V_{OCV}(x) = V_{pos}(x) - V_{neg}(x/y) \qquad (1\text{-}4)$$

Where V_{ocv} is the open circuit voltage of a full cell, V_{pos} and V_{neg} are the voltages of positive and negative electrodes, respectively, with respect to a lithium reference electrode (vs. Li/Li^+). The full cell voltage V_{ocv} is the highest when $x = 1$ and the lowest when $x = 0$.

In a "half cell" configuration, either the positive or the negative electrode is replaced by lithium metal as a voltage reference electrode. Therefore in the positive "half cell" case, the voltage of the half cell is reported with respect to the lithium reference electrode (vs. Li/Li^+). The positive "half cell" configuration is a widely used test vehicle to focus on the study of the positive electrode material.

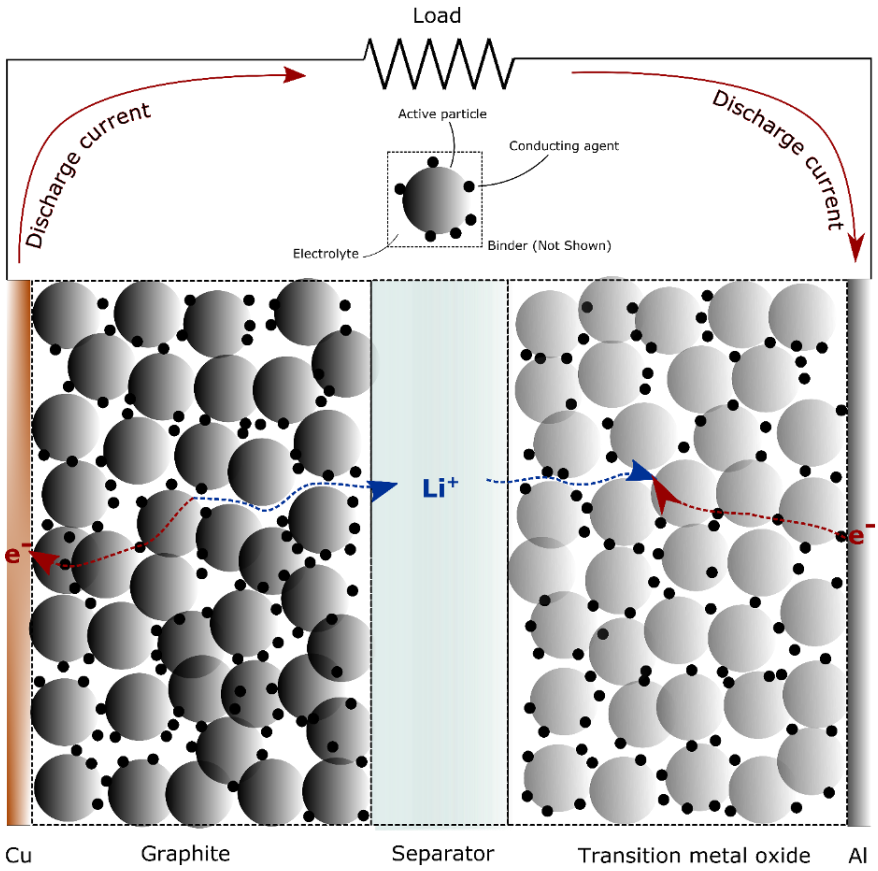

Figure 1.1 Schematic of a lithium-ion cell with a graphite negative electrode and a transition metal oxide as postive eletrode.

1.3.1 Positive Electrode Material

Most widely used positive electrode materials are olivine structure lithium iron phosphate, spinel structure lithium manganese oxide, or layered structure lithium metal oxide ($LiMO_2$).[13–15] They are the so-called active materials in the positive electrode shown in Figure 1.1 which are typically made of ca. 95 wt.% of the coating.

This Ph.D work focused on the study of layered structure $LiMO_2$ which can have many variations depending on the choice and compositions of the element. For example, $LiNi_{0.8}Co_{0.1}Mn_{0.1}O_2$ is among the most widely used layered structure materials in electric vehicles.[8,16–18] The metal ions in the layered structure serve as redox centres for charge balance when Li-ion moves in and out of the structure. When the Li-ion is totally removed from the structure, the average oxidation state of the metal ions increases from

3+ to 4+. The specific capacity of the layer structure LMO_2 as a function of delithiation degree, *x*, is given by the equation below.

$$Q = \frac{xF}{M} \qquad (1\text{-}5)$$

Where *Q* is the specific capacity, *x* is the degree of delithiation per chemical formula, *F* is the Faraday constant, and *M* is the molar mass. When $x = 1$, the material is completely delthiated and this gives the theoretical specific capacity of the material which is around 275 mAh/g for $LiNi_{0.8}Co_{0.1}Mn_{0.1}O_2$. In most all cases, the complete delithiation damages the reversibility of Li intercalation/detercalation which lowers the charge-discharge cycle life of the material in a lithium-ion cell. For example, $Li_{1-x}CoO_2$ limits the delithiation to around $x = 0.7$ in order to provide a reasonable charge-discharge cycle life.[19,20]

Figure 1.2 shows the (110) projection of the fully lithiated $LiMO_2$ crystal structure. This crystal structure belongs to the R-3m (#166) space group where the lithium is on the 3a site, the metal is on the 3b site and the oxygen is on the 6c site. The number represents the multiplicity at the specified site. The sites are named in alphabetical order. This crystal structure is also referred as the O3 structure as there are three metal oxide "slabs" in the unit cell and the lithium is sandwiched between the metal oxide slabs in octahedral sites. The stacking sequence of the atoms is also shown in Figure 1.2, where the Greek letters denote the Li position, the lower case letters denote the metal position and the upper case letters denote the oxygen position. This stacking sequence is called A-B-C stacking.[20] During delithiation, the material may undergo a series of phase changes depending on the degree of delithiation and the metal element and the composition. For examples, $Li_{1-x}CoO_2$ undergoes a series of phase changes from O3 to O6 and finally O1 when the material is completely delithiated.[21] Repeated phase transitions can damage the crystal structure and cause reduced cycling life.

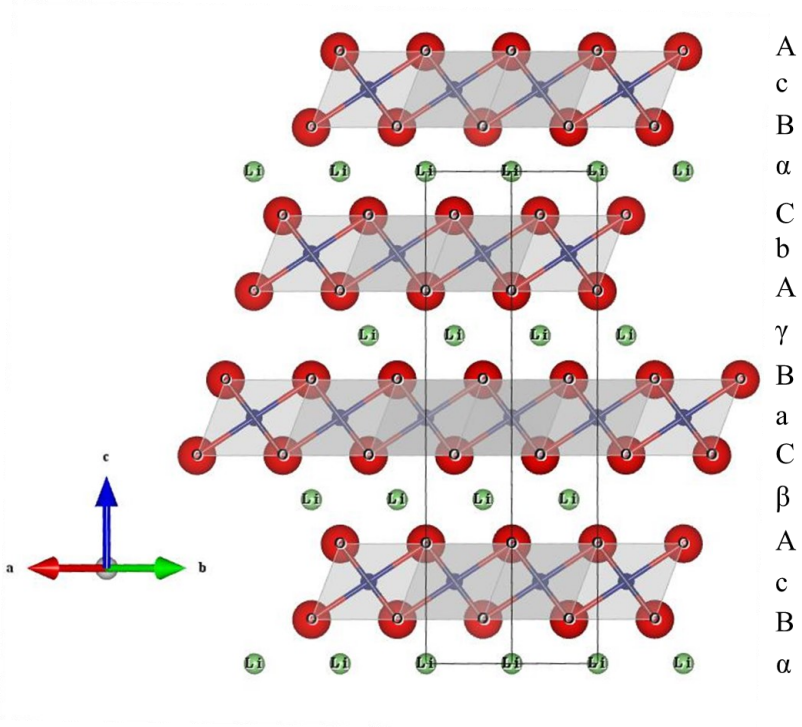

Figure 1.2 A (110) projection of the crystal structure of $LiMO_2$. The red, blue and green atoms represent oxygen, metal, and lithium respectively. The alignment of the atoms with the symbols shows the stacking sequence, where the Greek letters denote the Li position, the lower case letters denote the metal position and the upper case letters denote the oxygen position.

1.3.2 Negative Electrode Material

Carbonaceous materials, particularly artificial graphite or natural graphite, can be considered as the state-of-the-art negative electrode material in lithium-ion batteries for electrical vehicles. The theoretical capacity of graphite is 372 mAh/g when fully lithiated which gives a chemical formula of LiC_6. Graphite consists of many layers of graphene sheets stacked either in ABABAB sequence, namely 2H stacking, or ABCABC stacking, namely 3R stacking. In real world situation, the graphene sheets can have some stacking faults, called turbostratic misalignment, which reduces the reversible capacity of graphite.[22,23]

The graphite used in this work is artificial graphite (AG). Compared to natural graphite, the AG shows a higher level of purity as well as more stable quality.[3] The synthesis of AG starts with precursor material such as coke. Briefly, the precursor is first calcinated at

800-1200°C to convert into graphitizable carbon called soft carbon. The soft carbon is further treated by crushing and griding followed by graphitized at temperatures higher than 2500°C. To finalize the synthesis, graphite was further subjected to classifying, grinding and coating.[3]

1.3.3 Electrolyte Systems

The electrolyte used in a lithium-ion cell is typically an organic electrolyte which has a wider electrochemical window than an aqueous electrolyte. To obtain good performance, typical organic electrolytes used in lithium-ion cells consist of three components – the Li salt, carbonate solvent/co-solvent, and additives.[24,25] Figure 1.3 shows the chemical structures of a lithium salt $LiPF_6$ and some commonly used solvents.

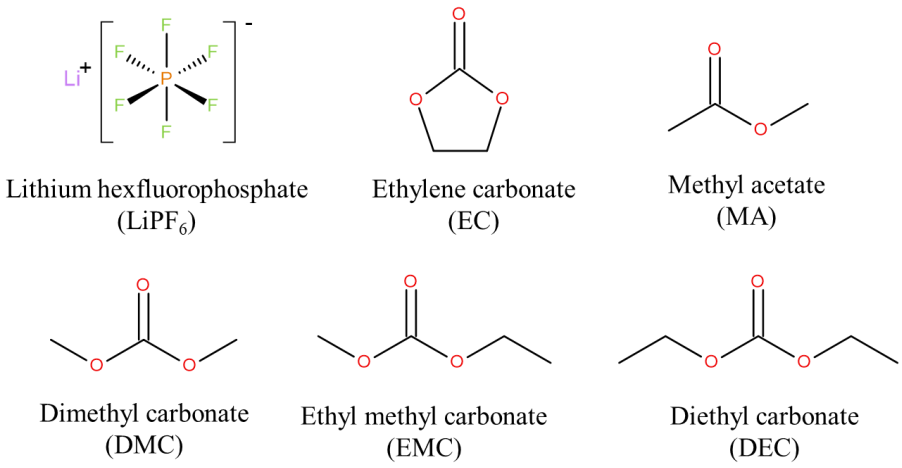

Figure 1.3 Chemical structures of Li-salt and solvent EC and co-solvents MA, DMC, EMC and DEC.

$LiPF_6$ can be considered as the state-of-the-art Li salt which provides reasonable lithium-ion conductivity in carbonate solvents.[26] Since $LiPF_6$ is very sensitive to moisture to form corrosive hydrogen fluoride (HF), a dry room or a glove box is required when handling.[27] Other Li salts have also been studied in the literature such as lithium tetrafluoroborate ($LiBF_4$),[28] lithium bix(oxalate)borate (LiBOB),[29] and lithium bis(trifluoromethanesulfonyl)imide (LiTFSi).[30,31]

The electrolyte solvent is required to dissociate the lithium salt (requires high dielectric constant) as well as to provide sufficient mobility for ion transport (requires low viscosity).[32] Ethylene carbonate (EC) has a high dielectric constant, but it is in solid form at room temperature. It is therefore necessary to mix/dissolve EC with other low viscosity carbonate co-solvents such as diethyl carbonate (DEC), dimethyl carbonate (DMC) or ethyl methyl carbonate (EMC), even though these co-solvents have low dielectric constants.[32] In recent years, methyl acetate (MA) was explored to be an electrolyte co-solvent. The very low viscosity of MA is reported to enhance the rate capability of the lithium-ion cell.[33–35]

The life time of lithium-ion cells are closely related to the electrolyte. This is due to side reactions between the electrolyte and the charged electrodes. In fact, even organic electrolytes are not thermodynamically stable within the operating voltage ranges of Li-ion cells. Almost all the lithium salt/carbonate solvent electrolyte systems used in current lithium-ion cells will be reduced at the graphite negative electrode during its initial intercalation.[36–38] This is because of the very low potential of lithiated graphite.[39,40] Fortunately, sometimes the reduction products are able to passivate the graphite surface to significantly hinder further reduction. This passivation layer, termed the solid electrolyte interphase (SEI), allows the continued operation of a lithium-ion cell. The quality of the SEI, in terms of its resistance and mechanical robustness, etc., is also critical in determining the cell performance.[36–38] The use of electrolyte additives at only a few weight percentages can effectively improve the SEI. In addition, many electrolyte additives are also used to minimize side reactions between the positive electrode and the electrolyte, especially when the lithium-ion cells are charged to high voltage to obtain more energy.[41–45]

Chapter 2 Background

2.1 Co-free Layered Structure $LiMO_2$

Many previous studies have reported the benefit of the inclusion of Co in layered structure lithium metal oxide (LMO_2) to reduce cation disorder, lower irreversible capacity, and increase rate capability.[9,46–50] However, due to the rapid price increase of Co driven by large-scale production all over the world and the relative scarcity of Co,[6,51] the minimization or even complete elimination of Co in Li-ion cells is desired.

Many researches have tried to completely remove Co from the layered structure by doping with low cost and abundant elements, such as Mg,[52] Mn,[47,53,54] Al,[53,54] Zn,[55] W,[56] etc. These materials have shown promising performance without any Co. Besides showing the cycling performance of these Co-free materials, emphasis was given to the rate capability of these Co-free materials. The removal of Co was shown to have no significant impact on the material rate capability. From another perspective, H. Li et al.[57] explored the impact of the Co and other metals on the phase transitions that occur in Li_xNiO_2. Repeated phase transitions can cause lattice damage to the material and significantly impact the material charge-discharge cycling performance. A series of $LiNi_{0.95}M_{0.05}O_2$ materials (where M = Mg, Al, Mn, Co) was prepared and phase changes were examined by *in-situ* XRD. The experiment results showed 5% of Co cannot suppress phase transitions unlike the other metals. H. Li et al.[57] also demonstrated that the presence of Co in layered transition metal oxides brings little or no value to NCA-type materials with high Ni content. These works encouraged more studies on Co-free materials.

In addition to the layered structure oxides, the use of Co-free olivine materials such as lithium iron phosphate (LFP) provides an alternative solution. Besides containing no Co and being relatively easy to make, LFP is commercially available and already used in electric vehicles.[58] LFP is also a very safe material and is able to provide a long life time.[59,60] The drawbacks of this material are the low operating voltage and low volumetric capacity which limit its gravimetric and volumetric energy density.[59,60]

2.2 Ni-rich Layered Structure $LiMO_2$

2.2.1 General Comments

Improving Ni-rich layered structure materials where Ni content ≥ 80% is an area of active research. The Ni-rich material can deliver high specific capacity with relatively high average voltage. Because of their high Ni content, the use of Co can be lowered which is another advantage of Ni-rich materials. However, in the extreme case where the Ni content is 100%, the resulting $LiNiO_2$ is not a practical material for lithium-ion battery application. Though having a very high specific capacity and containing zero Co, $LiNiO_2$ undergoes a series of phase transitions that yield a very low cycle life.[61] In addition, charged Li_xNiO_2 is very reactive with electrolyte at elevated temperature leading to Li-ion cells that are very difficult to make safe enough for commercial uses.[8,59,62]

Increasing the Ni-content brings high specific capacity and lowers the Co content, however increasing the Ni-content may also decrease the charge-discharge cycle life of the material.[8,9,63] Figure 2.1 shows the initial specific capacity vs. cycle life of various Ni-rich (≥ 80%) materials with different compositions collected by various Dahn group members over the years. The materials were cycled with either 4.3 or 4.4 V upper cut-off voltages. All the data points were measured at 30°C in coin half cells. The trend of these data points indicates the difficulties of simultaneously having high specific capacity and long charge-discharge cycle life. The ultimate goal is to find a material containing zero Co that can reach the upper right corner of this graph.

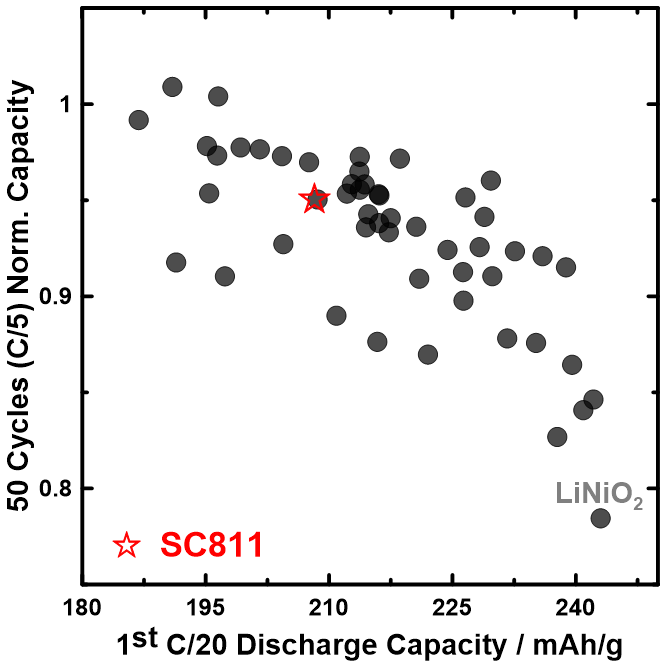

Figure 2.1 The 50th C/5 cycle normalized capacity vs. initial C/20 discharge capacity of Ni-rich (≥ 80%) materials with and without Co measured at 30°C in coin half cells. The half cell configuration is shown in Figure 3.3. All electrodes have 94% active material, 3% conductive agent and 3% binder. The electrolytes used in the coin cells were either 1.0 M $LiPF_6$ in EC:DEC (1:2 v/v) or 1.2 M $LiPF_6$ in FEC:DMC (1:4 v/v). The upper cut-off voltages were either 4.3 V or 4.4 V. The lower cut-off voltages were 3 V. Commercial-grade single crystal $LiNi_{0.8}Mn_{0.1}Co_{0.1}O_2$ (SC811) is shown in red star.

2.2.2 Degradation Mechanism and Solutions

When the material is at high state of charge, the highly oxidizing Ni^{4+} has been suggested to be responsible for electrolyte oxidation.[64–67] Previous studies have also shown surface structural reconstruction to spinel and/or rock-salt phases occurs when electrolyte is in contact with the Ni-rich materials during cycling.[68,69] All these factors contribute to the cell impedance growth that degrades the cell performance. In addition, many literature reports[42,70–75] have shown that microcracks developed within the polycrystalline particles during cycling are one of the main reasons for the capacity loss and impedance increase that cells display during long-term testing. These microcracks, from anisotropic unit cell volume change of each crystallite in a polycrystalline particle, can cause active materials to lose electric-connection and allow electrolyte infiltration into particle interiors

inducing more side reactions that increase cell impedance. The formation of microcracks on polycrystalline materials further exacerbates the side reactions between the electrolyte and the Ni-rich materials.[76,77]

Many methods have been proposed to resolve particle microcracking issues. Constraining the depth of discharge window is effective to alleviate microcracking.[69,78] However, cell energy density has to be sacrificed in exchange for prolonged cycle life. Introducing dopant atoms has been suggested to suppress/delay or even eliminate the H2 to H3 phase transition.[72,76] However, according to H. Li et al.,[63] doped materials will still suffer from anisotropic unit cell volume change at high voltage and inevitably microcracks will still develop. Others have suggested to use a surface coating to prevent particle microcracking,[78,79] but it is hard to imagine a surface layer of only several nanometers can effectively prevent microcracks from developing within a secondary particle of several micrometer diameter. Single crystal materials have been shown to be very robust against microcracking. Figure 2.2shows some cross-section SEM images of heavily-cycled single crystal SC532(ca. 4600 cycles), SC622(ca. 4100 cycles) and SC811(ca. 1300 cycles) electrodes retrieved from pouch cells (left column).[80] All cells were cycling at 20ºC with 1C CCCV mode during charge and 1C discharge. SC532 and SC622 cells were cycled between 3 and 4.3 V (ca. 4.4 V vs. Li/Li^+). SC811 cells were cycled between 3 and 4.2 V (ca. 4.3 V vs. Li/Li^+). Figure 2.2 also shows the cross-section SEM images of polycrystalline NMC622 (PC622) that did not undergo heavy cycling (right column). The electrodes were extracted from positive symmetric cells that underwent a series of voltage holds (50 hours in total) at ±0.9 V (4.455 V vs. Li/Li^+).[42] All cells were dissembled at top of charge. Figure 2.2 indicates that the single crystal materials are robust to particle microcracking whereas the polycrystalline particles are susceptible to microcracking when charged to high voltage.

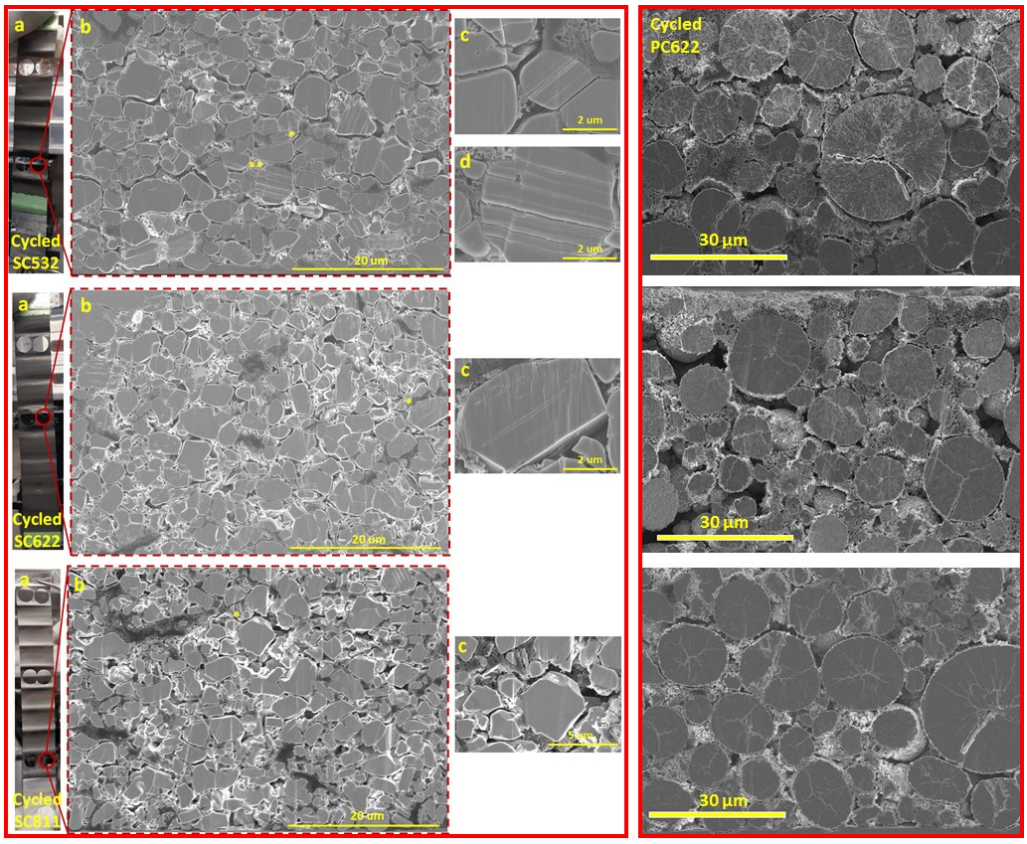

Figure 2.2 (Left column) Cross-section SEM images of heavily-cycled single crystal SC532, SC622 and SC811 retrieved from pouch cells.[80] (Right column) Cross-section SEM images of PC622 retrieved from symmetric cells that underwent 50 hours of total voltage hold at ±0.9 V (4.455 V vs. Li/Li$^+$) at 55ºC. The protocol was shown in detail in reference 42. Briefly, symmetric cells were charged at C/30 and held to 0.9 V for 10 h, then discharged at C/30 and held at -0.9 V for another 10 h. This process was repeated 4 more times. All cells were dissembled at top of charge.

Besides using single crystal material, surface modification by coating an inactive but protective nano-size layer has been shown to effectively extend the charge-discharge cycle life of NMC materials by lowering the rate of side reactions between the electrolyte and the material.[19,81–83] The adoption of core-shell structure where the Ni-rich high capacity core is protected by a lower capacity but more stable shell which contacts the electrolyte has also shown promising results to mitigate the poor cycling performance of Ni-rich materials.[84–86] This will be extensively discussed in the next section.

2.3 Core-shell Materials

2.3.1 Motivation

As discussed in previous section, the improved specific capacity of materials with increased Ni content is compromised by decreased capacity retention during charge-discharge cycling compared to lower Ni-content materials.[9] Surface coatings acting as a barrier to prevent the direct contact of the positive electrode materials with the electrolyte may improve the cycle life of Ni-rich materials especially at high voltage.[14,87] However, conventional coating materials such as Al_2O_3, TiO_2, etc.[65,82,88] suffer from low Li^+ and electronic conductivity and do not contribute to any capacity in a lithium-ion cell, therefore lowering the specific capacity and potentially increasing the impedance of the cell.[87] Additionally, coating these "inactive" materials onto lithiated layered transition metal oxides is an extra step in a large-scale industrial synthesis process that will inevitably increase the cost of production. Therefore, a more cost-effective approach is required to improve the cycle life of Ni-rich materials.

An alternative to coating is using a core-shell structure where the shell acts as a coating to the core.[85,89–91] By utilizing such a structure, a core-shell material with a Ni-rich core and a lower Ni content shell can be an excellent design strategy to balance energy density, cycle life, electronic/ionic conductivity and cost. A low Ni content shell of long cycle life may prevent direct electrolyte contact with the Ni-rich core of high specific capacity, enabling the core-shell material to have improved cycle life compared to the Ni-rich core alone. In addition, core-shell structures are easily synthesized by the co-precipitation method without any extra post-lithiation coating steps. Based on these merits, core-shell structures with a Ni-rich core and a lower Ni content shell show promise as high specific capacity and long cycle life materials.

2.3.2 Interdiffusion and the Choice of Element in the Shell

Zhang et al.[84] prepared a series of Ni-rich core-shell precursors with Mg-, Al- or Mn-containing shells. During heat treatment with $LiOH{\bullet}H_2O$ at 700°C, interdiffusion of metal atoms between core and shell occurred to different extents depending on the metals. After heating it was found that Mg was uniformly distributed in the particles. Only a small

portion of Al stayed localized on the surface whereas most of the Mn tended to stay near the shell region. J. Li et al.[92] measured the interdiffusion coefficients of Ni^{3+}/Co^{3+}, Co^{3+}/Mn^{4+} and Ni^{3+}/Mn^{4+} couples and showed that, at 900ºC, the Ni^{3+}/Mn^{4+} couple has the lowest inter-diffusivity. These studies demonstrated that a careful selection of the non-Ni element for the shell and the lithiation temperature are critical to prepare the exact core-shell one desires. Based on the relative rates of interdiffusion, Mn is a more favorable to use in the shell than Mg and Al in order to maintain the core-shell structure after heating.

Figure 2.3 compares two core-shell precursors lithiated with $LiOH•H_2O$ in oxygen for 20 hours at high temperature by cross-section energy-dispersive X-ray spectroscopy (EDS) mapping and line scans. Both core-shell precursors have a 17 μm $Ni(OH)_2$ core and a 0.5 μm thickness shell. One core-shell precursor has a $Ni_{0.8}Al_{0.2}(OH)_2$ shell, whereas the other core-shell precursor has a $Ni_{0.8}Mn_{0.2}(OH)_2$ shell. When both core-shell precursors were heated to 700ºC, the Al-containing shell has diminished which implied the core-shell structure has become a uniform structure. On the other hand, a Mn-containing shell still remained even after 20 hours heating at 750ºC. The EDS results match the conclusions in the literature that Al undergoes interdiffusion more rapidly than Mn.

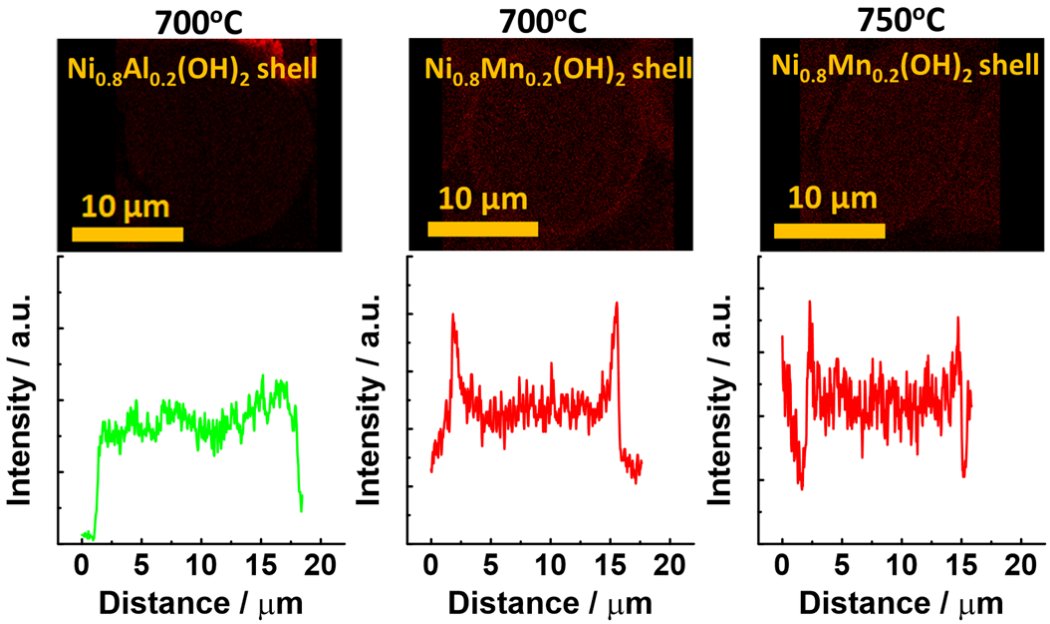

Figure 2.3 The EDS mapping (top row) and line scans (bottom row) of the $Ni(OH)_2$ core with either a $Ni_{0.8}Al_{0.2}(OH)_2$ shell or a $Ni_{0.8}Mn_{0.2}(OH)_2$ shell lithiated at 700°C or 750°C for 20 hours in oxygen with $LiOH{\bullet}H_2O$. The core diameter is 17 µm and shell thickness is 0.5 µm.

In addition to considering the impact of interdiffusion, incorporation of Mg^{2+} increases the average oxidation state of Ni which lowers material specific capacity,[57] and Al^{3+} introduces layered double hydroxide (LDH) phase in the precursor with anions such as SO_4^{2-}, CO_3^{2-}, which releases toxic gas during lithiation.[93–95] The LDH phase can be removed but requires an extra washing step as reported by A. Liu et al.[96] Other reports show the Li_5AlO_4 impurity phase is prone to form at high lithiation temperature.[97,98]

Though it is commonly believed by the lithium-ion battery community that Co is closely associated with the rate capability of the layered lithium transition metal oxides,[9,46] it has not been demonstrated so far, from an engineering perspective (reasonable electrode loadings, practical electrode formulations, etc.), that the presence of Co benefits electrode rate capability in Ni-rich positive electrode materials. The rate capability of Co-free core-shell material will be examined and compared to commercial-grade Co-containing layered structure materials in Chapter 5.

From a material safety perspective, H. Li et al.[57] showed that Mn substitution for Ni reduced the reactivity of the charged electrode materials with electrolyte at elevated temperature which implies a shell of Mn-containing material should improve battery safety. The reactivity of charged electrode materials with electrolyte was measured in Chapter 6 using accelerating rate calorimetry experiments to explore the influence of shell composition and thickness, heating temperature, etc.

2.4 Material Washing and Reheating

The typical large-scale production of layered materials is a multiple step process where the layered metal hydroxide precursor is first synthesized via the co-precipitation method.[3,99] In the following lithiation process, a slightly higher than the stoichiometric amount of lithium is mixed with the precursor to produce the desired layered lithium metal oxide by calcination in air or oxygen. The slight excess of lithium helps lower the cation mixing in the layered structure as well as compensating for potential lithium source loss during heating at a high temperature.[100] Regardless of lithium excess, it is inevitable to have some amount of unreacted lithium remaining on the surfaces of some particles. The surface lithium residuals introduce difficulties to slurry mixing and coating processes as a result of "slurry gelation" which is thought to be caused by polyvinylidene fluoride (PVDF) binder degradation in a basic environment.[10,11] Additionally, many reports have shown the surface lithium residuals, such as LiOH and Li_2CO_3, cause gas evolution and even electrolyte degradation that are detrimental to the safety and performance of lithium-ion cells.[101–105]

To remove the lithium residuals, one widely adopted method in the industry is washing the lithiated material with neutral or slightly basic water followed by a drying/reheating process.[106] However, even though the lithium residuals can be successfully removed, this method is not without any drawbacks. In addition of generating lots of waste water from a large-scale production standpoint, Xiong et al.[107] showed that water washing improved the cycling performance and structural stability of $LiNi_{0.8}Co_{0.1}Mn_{0.1}O_2$, but its capacity was also lowered and the washed material was more susceptible to water and CO_2 when stored in air. Park et al.[108] reported that the washing process removed the surface lithium

residuals as well as the lithium in the material structure of $LiNi_{0.91}Co_{0.06}Mn_{0.03}O_2$. Huang et al.[109] synthesized a series of $Li_{1+z}Ni_{0.815}Co_{0.15}Al_{0.035}O_2$ (z = 0.01, 0.03, 0.05 and 0.1) samples and reported the simultaneous loss of Li^+ and Al^{3+} from the particle surface during water washing which led to deteriorated electrochemical performance and structural stability. Hamam et al.[110] showed that the Li^+/H^+ ion-exchange occurred in the Ni-based lithium transition metal oxides in high pH aqueous solutions with little to no material dissolution, but both lithium deintercalation and metal dissolution occurred in low pH aqueous solutions. Pritzl and Teufl et al.[111] showed that a MOOH-like phase can be formed in the near-surface region of $LiNi_{0.85}Co_{0.1}Mn_{0.05}O_2$ as a result of Li^+/H^+ exchange upon washing. This structure decomposed into a less conductive spinel-like M_3O_4 structure then to a highly resistive rock-salt like MO surface layer as drying temperature increase. Full cell results showed cells with material dried at 300ºC had worse capacity retention than cells with material dried at 80ºC.

It is economically desirable to reduce the steps of large-scale material synthesis by removing the washing/heating steps. Methods proposed in the literature to solve the lithium residual problem focused primarily on the surface treatment of the unwashed positive electrode material particles.[81,112–114] Other reports have suggested using material doping to reduce/prevent the generation of surface lithium residual.[115,116] Though all these reported methods have been shown to be effective, to the best of our knowledge, very few studies have tackled this problem from the slurry mixing perspective with the unwashed material. In Chapter 7, the electrodes of the unwashed Co-free Ni-rich core-shell positive electrode materials were successfully made with oxalic acid incorporated in the electrode formulation. The electrochemical performance of the washed and unwashed Co-free Ni-rich core-shell materials therefore could be compared in commercial-grade pouch cells. The material performance evaluation in pouch cells facilitate the quantitative comparison of gas formation before and after long-term cycling for the washed and unwashed materials as a function of electrolyte additives.

2.5 Electrolyte Additives

Careful selection of electrolyte additives can significantly boost cell lifetime with minimum impact on the manufacturing process. The typical function of additives is sacrificial.[24,117] Additives are preferentially reduced or oxidized at different potentials compared to the control electrolyte to which they are added. The decomposition products serve as a protective layer, such as solid-electrolyte interphase (SEI), to lower side reactions between the charged electrode and electrolyte.

Figure 2.4 shows the chemical structures of additives used in Chapter 7 and Chapter 8. The electrolyte blends used in the core-shell pouch cells are based on the previous experience on SC532 and SC811 materials.[43,45,118,119] Electrolyte blends which yield long lifetimes were selected. The solvent blend used in the study of this work was EC (25%): EMC (5%): DMC (75%) by volume. All electrolytes used were either 1.2 M or 1.5 M $LiPF_6$ salt from either BASF or Shenzen Capchem. A control electrolyte is a blend of solvent and $LiPF_6$ salt only. Electrolyte additives were added to the control electrolyte with respect to the total electrolyte weight. The electrolyte blends used in this work are:

1. 2% VC and 1% DTD, abbreviated as 2VC1DTD, promoted by J. Li et al.[43]
2. 2% FEC and 1% LFO, abbreviated as 2FEC1LFO, promoted by L. Ma et al.[120]
3. 1% LFO, abbreviated as 1LFO, promoted by L. Ma et al.[119]
4. 1% LFO and 1% ODTO abbreviated as 1LFO1ODTO, promoted by X. Ma et al.[118]

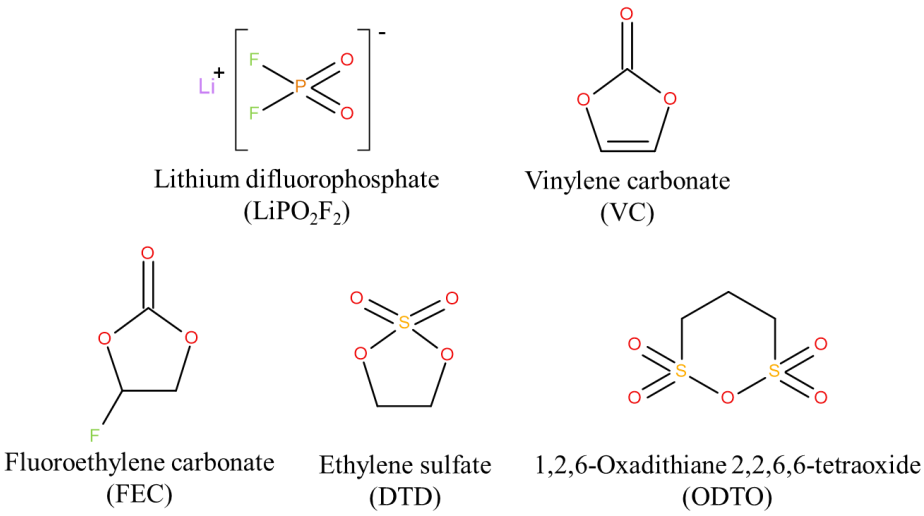

Figure 2.4 Chemical structures of additives used in this thesis.

The underlying working mechanisms of some additives in use is not exactly clear and are subject to debate.[121,122] Vinylene carbonate (VC) is the best-known additive for lithium-ion cells and has been intensively studied as a SEI-forming additive on the graphite negative electrode.[123] However, many reports have indicated its influence on positive electrode materials as well. Ouatani et al.[124] stated that VC can react with both negative and positive electrodes through a radical polymerization mechanism. Xiong et al.[125] and Burns et al.[126] believed that VC had a significant effect on the positive electrode, by reducing the rate of electrolyte oxidation, than on the negative electrode.

Ethylene sulfate (DTD) and 1,2,6 – Oxadithiane 2,2,6,6 – tetraoxide (ODTO) are sulfur-containing additives. The replacement of the carbonyl carbon with a sulfur atom lowers the energy of the lowest unoccupied molecular orbital (LUMO).[127,128] Therefore the sulfur-containing additives are generally easier to reduce than organic carbonates which is a desired feature for SEI-forming additive. To the best of the author's knowledge, the use of DTD was first reported by A. Sano et al.[129] (2009) as a SEI former in propylene carbonate electrolyte to decrease the initial irreversible capacity of graphite. In recent years, DTD has been heavily studied in commercial-grade pouch cells with various layered structure positive electrode materials, such as $LiCoO_2$,[130] $LiNi_{1/3}Mn_{1/3}Co_{1/3}O_2$,[131] $LiNi_{0.5}Mn_{0.3}Co_{0.2}O_2$[43] and $LiNi_{0.8}Mn_{0.1}Co_{0.1}O_2$.[45] The performance enhancement when

DTD was used singly is quite limited, but when used together with 2 wt.% of VC, the electrolyte blends have significantly increased the life time of single crystal $LiNi_{0.5}Mn_{0.3}Co_{0.2}O_2$ (SC532)/graphite cell by lowering side reactions with the charged positive electrode.[43] ODTO was first proposed by X. Ma et al.[118] Similar to DTD, the single use of ODTO in SC532/graphite cell had worse capacity retention than in combination with 1% LFO.

Fluoroethylene carbonate (FEC) and lithium difluorophosphate (LFO) are all fluorine-containing chemicals. C. Wang and K. Xu et al.[132] emphasized the benefit of having fluorine in the interphase and further pointed out the importance of how the fluorinated species exists, such as the morphology, valence, and distribution in the interphase, etc. FEC was considered for lithium-ion battery applications as early as in the 1990s.[122,133] FEC has shown significant performance improvement for Si negative electrode over conventional organic carbonates.[122,134] Yet there is no consensus as to how the exact underlying mechanism has occurred.[117,122] For graphite negative electrode, FEC was studied as a SEI-forming additive.[133,135,136] Some reports have also shown FEC participates in the formation of surface films on positive electrodes that improve the full cell performance when charged to high voltage.[137,138] LFO gained its popularity in recent years. Non-stoichiometric $Li_xPO_yF_z$ was detected in both the positive and negative electrode interphases from *X*-ray photoelectron spectroscopy (XPS).[139–141] The LFO is one of the products when $LiPF_6$ reacts with water. Interestingly, Burns et al.[142] showed that 1000 ppm of intentionally added water in $LiCoO_2$/graphite pouch cell with 1M $LiPF_6$ was beneficial compared to no water. Though not stated explicitly by Burns et al.[142], it could be possible that the formation of LFO by $LiPF_6$ reacting with water is responsible for the improved cell performance. LFO has been shown to improve both the positive and negative electrode performance in the literature.[140,143]

Chapter 3 Experimental Techniques

3.1 Synthesis of Ni-rich Co-free Core-shell Materials

As discussed in Section 2.3, Mn is more resistant to interdiffusion at high temperature than Al and Mg. Therefore, all the core-shell materials explored in this thesis contain only Ni and Mn in the shell phase. All core-shell precursors were provided by Hunan Zoomwe Zhengyuan Advanced Material Trade Company, Ltd., Changsha 410000, China (Zoomwe). The Zoomwe precursors were synthesized via the co-precipitation method. However, the detailed synthesis conditions were not revealed to the author of this thesis. The synthesis of core-shell precursor via the co-precipitation method is well documented in the literature.[84,144–147] Briefly, the core and shell aqueous stock solutions (such as metal sulfate – MSO_4) were first prepared separately. The core solution is gradually discharged to a tank reactor along with chelating agent such as ammonium hydroxide. Sodium hydroxide (NaOH) is used to control the pH of the reaction. Once the core phase has finished the reaction, the shell solution is added to the reactor and the pH is adjusted accordingly. The precipitates were filtered, rinsed, and collected for lithiation. The size of the core and the thickness of the shell depend on the amount of solution which participated in the reaction.

For the lithiation process,[8,17,148] the as-received Zoomwe core-shell precursors were mixed with ground $Li(OH)_2 \cdot H_2O$ (FMC) powder by a mortar and pestle until homogenous texture was reached. The mixed powder has a lithium to transition metal molar ratio of 1.02. The lithiation process was started by initially heating the mixed powder in oxygen in a tube furnace at 480^{o}C for 3 hours with ramping rate of 10^{o}C/min. This step allows $Li(OH)_2 \cdot H_2O$ to melt and react initially with the precursors. The preheated powder was then taken out of the furnace and ground to eliminate areas of local lithium excess. The ground powder was heated again in oxygen to various temperatures for either 10 or 20 hours with the same ramping rate. The tube furnace was allowed to cool down naturally and the collected samples were ground again and stored in argon-filled glove-box for further use.

3.2 Material Characterizations

3.2.1 Powder *X*-ray Diffraction (XRD)

3.2.1.1 **Bragg's Law**

Figure 3.1 shows a schematic of *X*-ray diffraction by two atoms on two planes of a crystal with an interlayer spacing *d*. The two incident *X*-ray beams with wavelength λ are diffracted by atom A and C to the direction shown in the schematic. The path difference of the two incident beams is BC. The path difference of the two diffracted beams is CD. The total path difference BC + CD can be expressed by trigonometry as $2d\sin\theta$.

For a constructive interference to occur, the total path difference must be a multiple of the wavelength λ. Bragg's law describes this relationship and is shown below,[149]

$$n\lambda = 2d\sin\theta \qquad (3\text{-}1)$$

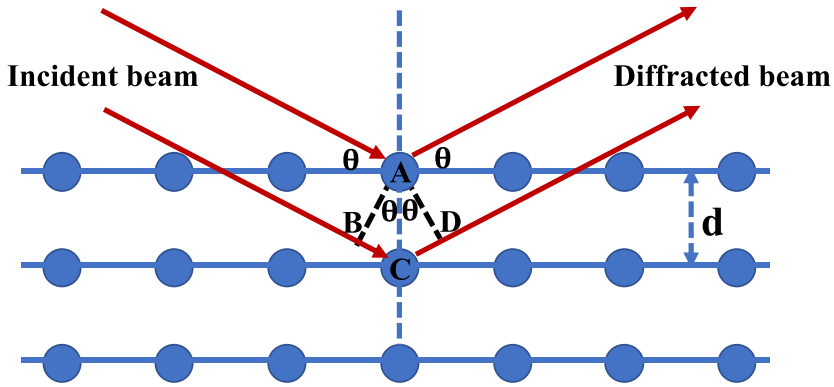

Figure 3.1 A schematic of *X*-ray diffraction

3.2.1.2 **Intensity of diffraction**

The intensity of powder diffraction peaks is determined by many factors. In this work, the three most important factors that impact the peak intensities are the multiplicity factor, Lorentz-polarization factor, and the geometric structure factor.[149]

The multiplicity factor indicates the number of equivalent *(hkl)* places that contribute to the diffraction at a given angle. The Lorentz factor accounts for the randomly oriented planes in a powder sample. The polarization factor accounts for the unpolarized incident beam. The Lorentz-polarization factor is a function of Bragg angle. If a monochromator is used, the Bragg angle for the monochromator is included in the polarization factor. The structure factor describes the diffracted intensity of a set of planes (*hkl*) that is dependent of fractional atomic position (*x, y, z*) in a unit cell. The structure factor is expressed as the follows,[149]

$$F_{(hkl)} = \sum_{j=1}^{N} n_j f_j e^{2\pi i(hx_j+ky_j+lz_j)} \qquad (3\text{-}2)$$

Where f_j is the atomic scattering factor of atom j at fractional coordinate (x_j, y_j, z_j) in a unit cell. n_j represents the occupancy of atom j at this coordinate.

For an ideal stoichiometric $LiNiO_2$ sample with no cation mixing, the fractional coordinates for Li and Ni are (0,0,0) and (0,0, ½), respectively.[61] The oxygen atom coordination is approximately (0, 0, ~¼). According to the formula above, the structure factor for the (104) plane is:

$$F_{(104)} = f_{Li}e^{2\pi i(0)} + f_{Ni}e^{2\pi i(2)} + 2f_O e^{2\pi i(1)} \qquad (3\text{-}3)$$

$$F_{(104)} = f_{Li} + f_{Ni} + 2f_O \qquad (3\text{-}4)$$

The atomic scattering factor of Li, Ni and O can be found in the literature.[149] The intensity of the (*hkl*) powder diffraction peak in a XRD pattern is proportional to $|F_{(hkl)}|^2$.

3.2.1.3 **Diffractometer**

Figure 3.2 shows an image of a diffractometer and its schematic with major components labeled. The *X*-ray beam was first generated from a Cu-target *X*-ray tube that passes

through a divergence slit. The *X*-ray beam then interacts with the powder sample. The diffracted beam passes through an anti-scattering slit that helps remove the air scattering and reduces the background. After passing through the receiving slit, the diffracted beam was filtered by the monochromator to remove any wavelengths other than the desired-K_α wavelength.[150] The slit sizes are adjustable. Large-size slits increase the intensity but at the cost of resolution.

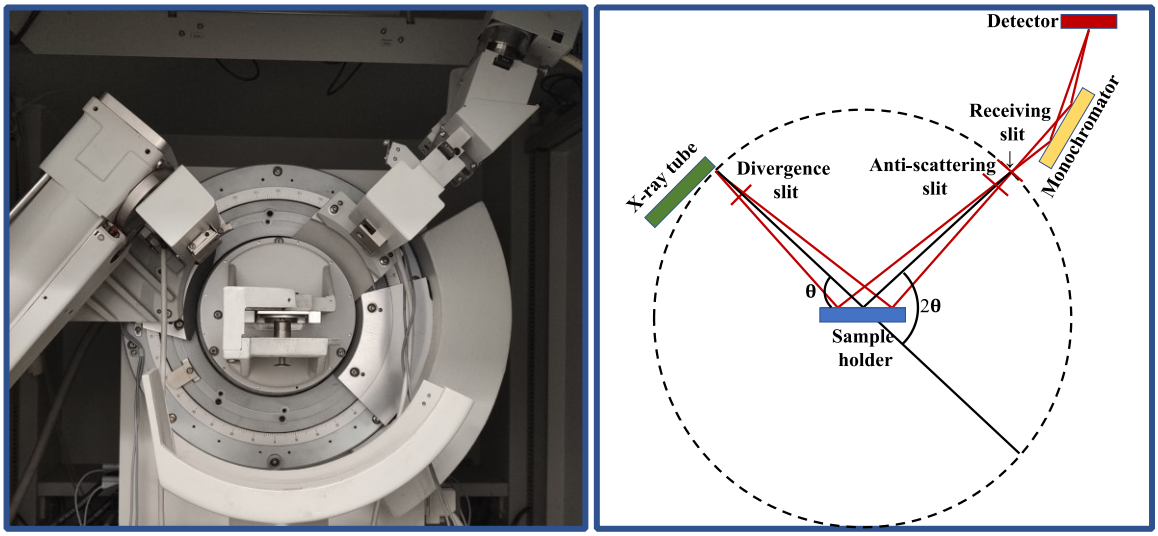

Figure 3.2 A diffractometer (left) and its schematic (not to scale) with major components labeled (right)

3.2.1.4 **Data collection**

In this thesis, powder XRD was measured using a Bruker D8 diffractometer equipped with a Cu target X-ray tube and a diffracted beam monochromator. Samples were measured in a scattering angle (2Θ) range from 15° to 90° for 3 s at intervals of 0.02° with a 1° divergence slit, a 1° anti-scattering slit and a 0.2 mm receiving slit.

3.2.1.5 **Rietveld refinement**

The XRD pattern profile was conducted via Rietveld refinement. The Rietveld refinement is basically a least-square method to fit the measured data with a calculated pattern based on the proposed structure model so that key structural parameters, such as lattice parameters, fractional atomic positions, etc., can be extracted and compared.

Rietveld refinement in this work was conducted using Rietica Software.[151] The refinements assumed the R-3m space group (#166) with Li in 3a sites, Ni and Mn in 3b sites and oxygen in 6c sites. Neutral atom scattering factors were used. The model used for the refinement is $[Li_{1-x}Ni_x]_{3a}[Ni_{1-x}Li_x]_{3b}O_2$ (*i.e.* $LiNiO_2$) to account for cation mixing. Cation mixing is assumed to only occur between Ni and Li in this thesis. The exchange of Ni and Li atoms between 3a and 3b sites was allowed with constraints to extract cation mixing, Ni_{Li}, information and to obtain a better fitting. The constraints were set up to have a total composition of 3a site Li and 3b site Li equal to 1.0, and a sum of 3b site transition metal and 3a site Ni equal to 1.0. The XRD refinement for the NCA powder (Umicore) assumes a composition of $Li[Ni_{0.8}Co_{0.1}Al_{0.1}]O_2$.

The fitting quality of this work is measured by Bragg-*R* factor, R_b. A very high quality of fit has $R_b < 2$. Other *R* factors are also used in the literature to examine the fitting quality, such as R_{wp}, where *wp* stands for weighted pattern.[152,153]

3.2.2 Ion-milling

Ion-milling is a process of bombarding the top surface of a sample with high-energy ion gun to create a clean surface. In this work, an ion-mill was used to create cross sections of various core-shell particles with an Ar-ion beam. The core-shell particles need to be first prepared in an electrode in order to be ion-milled by the JEOL IB-19530CP cross-section polisher. The preparation of electrodes is described in Section 3.3.1. Electrodes were milled with an Ar-ion beam for 50 minutes using a 6 kV coarse step followed by a 5 minutes/4 kV fine step.

3.2.3 Scanning Electron Microscopy (SEM) and Energy Dispersive X-ray Spectroscopy (EDS)

The SEM uses a focused high energy electron beam to investigate a sample. The most commonly used modes for imaging samples are the backscattered electron mode and secondary electron mode.[154,155] The backscattered electron mode is able to give a compositional contrast in the image. Heavier atoms scatter more electrons which are brighter in the images. Secondary electron mode is useful to show morphology and

topography information. The secondary electrons are generated via atom ionization when the electron beam interacts with the sample. The secondary electrons come from the near surface region of the sample.[154,155] In this thesis, the secondary electron mode with a "mixed" detector mode was used for imaging. This mode combines portions of the signals from the upper and lower detectors. Though the imaging was in the secondary electron mode, the lower detector was still able to show image contrast based on atomic numbers of different elements according to the machine manufacturer.

EDS utilizes the characteristic *X*-ray of an element to provide elemental/compositional information about a sample.[149,154,155] When a high energy electron beam interacts with an atom, its inner shell electron can be excited and ejected from the atom. Once this happen, an outer shell electron may fall into the inner shell and simultaneously emit an *X*-ray. Since the energy of this *X*-ray is unique to each element, it is termed as the characteristic *X*-ray which is used to identify the presence of certain element in the sample.[149,154,155]

Together with the ion-mill, cross-section SEM can be used to examine the particle microcracking before/after long-term cycling as described in Section 2.2.2, and the cross-section EDS can be used to confirm the core-shell structure after heating at various temperatures. In this thesis, cross-section SEM images and EDS mapping/line scans were measured using a Hitachi S-4700 cold field emission SEM with an integrated Oxford Inca EDS system. The SEM images for examining particle structural integrity before/after charge-discharge cycling were obtained using an accelerating voltage of 5 kV and a current of 15 μA. The cross-section EDS Mn mapping/line scans were obtained with an accelerating voltage of 15 kV and a current of 15 μA to produce Mn Kα characteristic X-rays. The EDS data was collected for between 5 and 8 mins.

3.2.4 Powder Electrical Resistivity

Powder electrical resistivity measurements were conducted using an in-house-built pellet press. 200 mg of powder was loaded between two stainless steel rods that fit into a Teflon-lined cylindrical sleeve. The rods had a diameter of 1 cm^2 and pressure was applied using a manual hydraulic press. The bulk electrical resistance of the pressed

powder was recorded as a function of true pressure using a 4-wire measurement with a Keithley-2700 multimeter. The SC811 powder was obtained by scraping the pouch cell electrodes. Each measurement was carried out three times and the average resistance and standard deviation was calculated and reported.

3.2.5 Powder Crush Test

To examine the mechanical properties of the synthesized materials, the material powders were crushed using an Enerpac hand press. To do so, 0.1 g of material powder was put in a pelletizer with a 4.72 mm diameter. The pelletizer was then inserted into the hand press. A pressure of 700 MPa was used to crush the materials which corresponded to an oil pressure of 1566 psi on the press gauge. The sample was held under 700 MPa for 90 seconds before releasing. The overall process was done twice. The pelletizer was cleaned with acetone between runs. The crushed samples were collected for the SEM examination.

3.2.6 Accelerating Rate Calorimetry (ARC)

The ARC is operated in a heat-wait-search (HWS) mode.[156,157] The sample is first heated to the initial temperature. After thermal equilibrium, the system starts to search for the temperature increase greater than the set sensitivity. If the rate of temperature increase is lower than the set sensitivity after the search, the system will heat up again to the next set temperature and the HWS sequence will start again. This process is repeated until an exothermic reaction is detected or the stop temperature is reached. If an exothermic reaction is detected, the system will track this reaction by maintaining the adiabatic condition until the reaction is completed.

The ARC is used in this thesis to explore the exothermic reaction between the charged core-shell material and the electrolyte.[8] To prepare the charged material, lithiated materials were first mixed with PVDF and Super-S carbon black with a mass ratio of 92:4:4 in NMP. The as-obtained slurry was dried in vacuum overnight and then lightly ground. Approximately 280 mg of powder was obtained. The powder was then transferred into a hardened steel die to make a pellet at 2000 psi pressure for 90 s. The pellet was used as a positive electrode in a half cell and slowly charged (at C/100) to 4.3

V vs. Li/Li^+ for delithiation. The half cell was then opened in glove box and the pellet was harvested and ground. The ground powder was then rinsed with DMC to remove residual electrolyte and dried in vacuum for 24 h.[158]

The ARC tests were performed using sealed tubes containing delithiated material and fresh 1.5 M $LiPF_6$ in EC/DMC (3:7 v/v) electrolyte with 2% VC. To ensure the results are comparable, the capacities of different materials were controlled to be 10 mAh in each tube and a powder/electrolyte mass ratio of 3:1 was used. The ARC starting temperature was set to be 100°C. ARC tests were tracked under adiabatic conditions when the sample self-heating rate (SHR) exceeded 0.02°C/min. Experiments were stopped at 350°C or when the SHR exceeded 20°C/min. To test the reproducibility of the ARC sample preparation and measurement, two nominally identical ARC samples were made and tested. The ARC experiments in this thesis were conducted by Dongxu Ouyang.

3.3 Coin Half Cell Building and Testing

3.3.1 Electrode Preparation

Core-shell electrodes for charge-discharge cycling were prepared by mixing 92 wt% of the as-synthesized core-shell material, 4 wt% of Kynar polyvinylidene fluoride (PvdF) binder and 4 wt% of Super S carbon black in N-methyl-2-pyrrolidone (NMP) in a planetary mixer. The mixture was coated on Al foil with a 150 μm notch bar spreader. The resulting electrode was dried in a convection oven at 110°C, then calendared. The electrode was further punched into small circular electrodes with a diameter of 1.275 cm for coin cell building. The electrode loading was ca. 10 mg/cm^2. Electrodes for direct current resistance (DCR) measurement were prepared similarly as those for cycling, but the core-shell and NCA electrodes have a loading of ca. 21 mg/cm^2 and a formulation of 94:3:3 (active material: binder: carbon black). PC and SC811 electrodes of ca. 21 mg/cm^2 loading and 94% active material were directly punched from the single-side-coated region of commercial-grade pouch cell's positive electrodes.

3.3.2 Coin Half Cell Assembly and Electrolyte

Figure 3.3 shows a schematic of a standard 2325 coin cell and its components. All coin cells were assembled in argon-filled glovebox in this work. Each coin cell has one positive (diameter ca. 1.275 cm) and one Li foil negative electrode with two pieces of Celgard 2300 separators. Electrolyte for coin half cell cycling was 1.2 M $LiPF_6$ in FEC/DMC (1:4 v/v). This is the standard coin cell electrolyte used in this thesis unless otherwise specified.

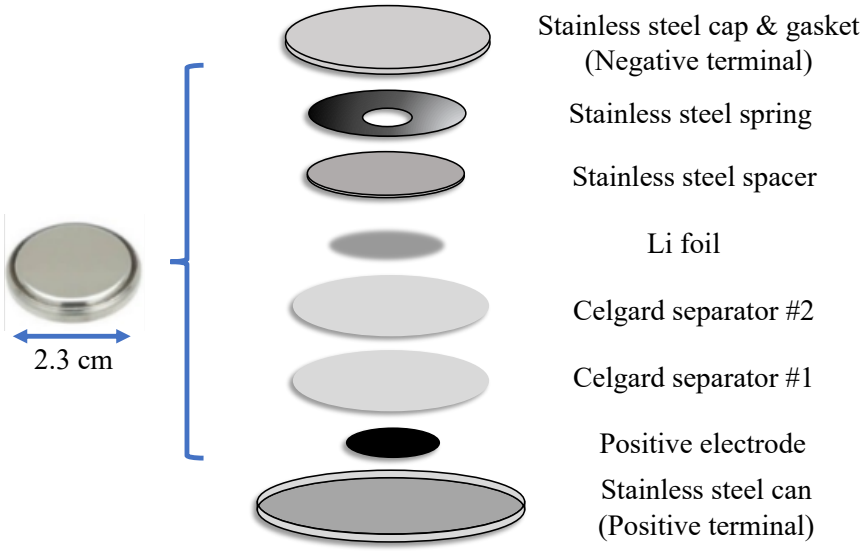

Figure 3.3 A schematic of a standard 2325 (2.3 cm diameter, 2.5 mm height) coin cell and its components.

3.3.3 Direct Current Resistance (DCR) Measurement

The DCR measurement was conducted using a Maccor series 4000 battery charger at 40°C. The coin cell half cells first underwent 1.5 C/20 cycles from 3 to 4.3 V. The open-circuit potentials (OCV) of coin cells were monitored for 30 mins and then coin cells were discharged at C/2 for 30 s. The DCR was calculated by the voltage difference between OCV and the cell voltage at 10 s divided by the current at C/2. This gives the DCR at this voltage during discharging. Similarly, coin cells were charged at C/2 for 30 s after the OCV step and the DCR was calculated exactly the same way. This process was repeated from 0 to 100% state-of-charge during both discharging and charging. The cells

were further allowed to run at C/10 for 30 cycles and the DCR was measured again with an identical procedure as before cycling.

3.3.4 Long-term Charge-discharge Cycling

Galvanostatic charge/discharge cycling was conducted with E-one Moli Energy Canada battery testing systems at 30ºC. Coin cells were cycled from 3 to 4.3 V vs. Li/Li^+ with 2 initial C/20 cycles and then continued cycling with C/5 for 100 cycles unless otherwise specified. Two C/20 cycles were run after the 50th C/5 cycles and another 2 C/20 cycles after the 100th C/5 cycles. Unless otherwise specified, this is the standard cycling protocol used.

3.4 Pouch Cell Formation and Testing

3.4.1 Positive Electrode Materials

Coated single crystal SC532 was provided by Vendor 1 and is the same material featured in reference [159]. Uncoated single crystal SC811 was provided by Vendor 2 and is the same material featured in reference [45].The polycrystalline Co-free core-shell material has an average composition of $LiNi_{0.94}Mn_{0.06}O_2$. The core shell hydroxide precursor has a 16 μm $Ni(OH)_2$ core and a 1 μm thick $Ni_{0.8}Mn_{0.2}(OH)_2$ shell and was obtained from Hunan Zoomwe Zhengyuan Advanced Material Trade Company, Ltd., Changsha 410000, China. This is the core-shell precursor explored in Chapter 4 toChapter 6. The final core-shell oxide was prepared by reacting $LiOH•H_2O$ with the hydroxide precursor at elevated temperature by vendor 3. The material obtained right after the lithiation process was named as the “unwashed” material. The washing/reheating process was carried out by vendor 3 on the “unwashed” material to obtain the “washed” material. The detailed washing/reheating process was not revealed to the author of this thesis. The 0.7 wt.% of oxalic acid was added to the slurry formation of the “unwashed” material to alleviate gelling of the slurry so that the unwashed core-shell material could also be made into pouch cells.

3.4.2 Cell Specifications and Formation Protocol

402035 size machine-made pouch cells were built by LiFun Technology (Xinma Industry Zone, Golden Dragon Road, Tianyuan District, Zhuzhou City, Hunan Province, PRC, 412000) with artificial graphite from Kaijin (China). All pouch cells were vacuum sealed in a dry room without electrolyte and then shipped to Dalhousie University in Canada. Table I shows the positive and negative electrode specifications of SC532/AG, SC811/AG, washed core-shell/AG, and unwashed core-shell/AG pouch cell.

Table 3.1 Electrode specifications of SC532/AG, SC811/AG, washed core-shell/AG, and unwashed core-shell/AG pouch cells. The unwashed core-shell positive electrode slurry had 0.7 wt.% of oxalic acid in the formulation.

		SC532	SC811	Core-shell (washed)	Core-shell (unwashed)
Positive Electrode	Loading (mg/cm^2)	21	21	19	22
	Active material fraction (%)	94	94	94	94
	Density (g/cm^3)	3.5	3.5	3.2	3.1
	Reversible capacity (mAh/g)	180	210	220	220
	Total coating mass (g)	1.5	1.19	1.06	1.5
Negative electrode	Loading (mg/cm^2)	12	15	14	15.5
	Active material fraction (%)	95.4	95.4	95.4	95.4
	Density (g/cm^3)	1.55	1.55	1.5	1.5
	Reversible capacity (mAh/g)	350	350	350	350
	Total coating mass (g)	0.9	1	0.9	1.2

The formation protocol for the SC532 pouch cells has been described in many previously published papers.[43,118,119] The SC532 pouch cells were formed at 40ºC under C/20 CCCV mode (constant current charging to top of charge followed by constant voltage hold) to

either 4.1 V or 4.3 V. The CV time was set to be 1 hour. The cells were then discharged to 3.8 V for gas and impedance measurement.

The formation protocol for the SC811 pouch cells was described in the paper published by W. Song et al.[45] The SC811 pouch cells were formed at 40ºC under C/20 CCCV mode to either 4.1 V or 4.2 V. The CV time was set to be 1 hour. The cells were then discharged to 3.8 V for gas and impedance measurement.

The washed and unwashed core-shell pouch cells were formed by one full C/20 (with respect to the washed core-shell pouch cell capacity) CC cycle to either 4.1 V or 4.3 V unless otherwise specified at 40ºC.with a 3.0 V lower voltage cut-off. The cells were then charged to 3.8 V for gas and impedance measurements.

3.4.3 Gas Measurement

The gas measurement was conducted based on Archimedes' principle developed by C.P.Aiken et al.[160] Briefly, the weight of each pouch cell submerged in DI water was measured before/after formation and long-term charge-discharge cycling. The weight difference is proportional to the gas volume generated.

3.4.4 Electrochemical Impedance Spectroscopy (EIS)

Cell impedance was measured at 3.8 V via electrochemical impedance spectroscopy on a Biologic VMP-3 instrument. Pouch cells were allowed to thermally equilibrate for 1 hour at 10ºC before measurement. Alternating current impedance spectra were collected with ten points per decade from 100 kHz to 10 mHz with a signal amplitude of 10 mV. The charge-transfer resistance R_{ct} is defined herein as the span of the convoluted "semicircle" from high to low frequency for simplicity of discussion.

3.4.5 Long-term Charge-discharge Cycling

The long-term charge-discharge cycling of pouch cells were all measured on Neware (Shenzen, China) chargers at 20 and 40ºC. Two upper cut-off voltages (UCVs) were selected for each positive material. The SC532 cells were cycled from 3.0 to either 4.1 V

or 4.3 V. The SC811 cells were cycled from 3.0 to either 4.06 V or 4.2 V. The washed and unwashed core-shell cells were cycled from 3.0 to either 4.04 V or 4.18 V. The SC532 and SC811 cells were measured with C/3 CCCV mode at 40ºC and 1C CCCV mode at 20ºC. All the core-shell cells were measured with C/3 CCCV mode at both 20ºC and 40ºC.

Chapter 4 Initial Synthesis and Evaluation of Co-free Ni-rich Core-shell Materials

4.1 Introduction

This chapter discuses the initial attempts to synthesize and evaluate of Co-free Ni-rich core-shell materials. All three core-shell precursors in this chapter have $Ni(OH)_2$ core and only Ni and Mn in the shell phase.

For an excellent core-shell material, it is expected that it will have a comparable specific capacity to its Ni-rich "core" material, but its capacity retention will be much better because of the lower Ni-content "shell". Therefore, the uniform "core" and "shell" materials were also prepared and their performances were compared to the corresponding core-shell materials.

The impacts of heating temperature, shell composition and shell thickness on the physical properties, specific capacity and charge-discharge cycling performance of core-shell materials were also explored. This chapter demonstrates the factors that must be carefully considered to make core-shell materials with both high specific capacity and excellent cycling performance.

The results of this chapter were incorporated into a manuscript published in the *Journal of the Electrochemical Society* with open access.[148]

4.2 Experimental

Three core-shell precursors, two uniform "shell" precursors and one uniform "core" precursor were provided by Zoomwe. The core-shell precursors were:

1. 17 μm diameter $Ni(OH)_2$ core and 0.5 μm thickness $Ni_{0.5}Mn_{0.5}(OH)_2$ shell
2. 16 μm diameter $Ni(OH)_2$ core and 1 μm thickness $Ni_{0.8}Mn_{0.2}(OH)_2$ shell
3. 17 μm diameter $Ni(OH)_2$ core and 0.5 μm thickness $Ni_{0.8}Mn_{0.2}(OH)_2$ shell

Core-shell precursors #1-3 have an average Ni content of ca. 92 mol%, 94 mol% and 97 mol%, respectively, as measured by Zoomwe. The two uniform "shell" precursors both with 16 μm size are $Ni_{0.8}Mn_{0.2}(OH)_2$ and $Ni_{0.5}Mn_{0.5}(OH)_2$. The core-shell and the "shell" precursors were lithiated as described in Chapter 3.1 for 20 hours in oxygen at 650°C, 700°C, 750°C or 800°C. The "core" precursor $Ni(OH)_2$ has a diameter of 18 μm and was only heated to 700°C.

For ease of discussion, the lithiated materials were given names based on their corresponding precursors, for example, CS92 – 5050 – 17/0.5, or the CS92 series for brevity, is the lithiated material made from a core-shell precursor #1 that has an average Ni content of 92 mol%, a $Ni_{50}Mn_{50}(OH)_2$ shell, a 17 μm diameter core and a 0.5 μm thickness shell. The "shell" materials $LiNi_{0.8}Mn_{0.2}O_2$ and $LiNi_{0.5}Mn_{0.5}O_2$ were denoted as NiMn8020 and NiMn5050, respectively.

4.3 Results and Discussion

4.3.1 Precursor Characterizations

Figure 4.1(a) shows SEM images of three core-shell precursors along with cross-sectional SEM images and Mn EDS mappings shown in the insets. The EDS mappings confirm the presence of Mn-rich shells as desired. The three precursors all have an identical D_{50} diameter of 18 μm but have varying core sizes, shell thicknesses and compositions as noted in the Experimental section. Figure 4.1(b) shows the XRD patterns of the core-shell precursors in comparison to the "core" $Ni(OH)_2$ which is also commercial-grade. The XRD pattern of core-shell precursor #2 clearly shows Bragg peaks from both the core and shell phases while the peaks from the shell phase in #1 and #3 are less intense due to the limited amount of the shell phase. In the case of #1, due to the similarity of lattice constants between the $Ni(OH)_2$ core phase and $Ni_{0.5}Mn_{0.5}(OH)_2$ shell phase as shown by Zhou et al.,[93] the Bragg peak separation from these two phases is even harder to observe than core-shell precursor #3. Figure 4.1(c) and (d) show SEM images of the uniform "shell" precursors $Ni_{0.8}Mn_{0.2}(OH)_2$ and $Ni_{0.5}Mn_{0.5}(OH)_2$, respectively. The $Ni_{0.5}Mn_{0.5}(OH)_2$ particles show a very rough surface morphology compared to $Ni_{0.8}Mn_{0.2}(OH)_2$, presumably a result of much higher Mn content. Figure 4.1(e) shows the

XRD patterns of the two commercial-grade uniform "shell" precursors, $Ni_{0.8}Mn_{0.2}(OH)_2$ and $Ni_{0.5}Mn_{0.5}(OH)_2$. The $Ni_{0.5}Mn_{0.5}(OH)_2$ XRD pattern shows the presence of oxyhydroxide phase.[93]

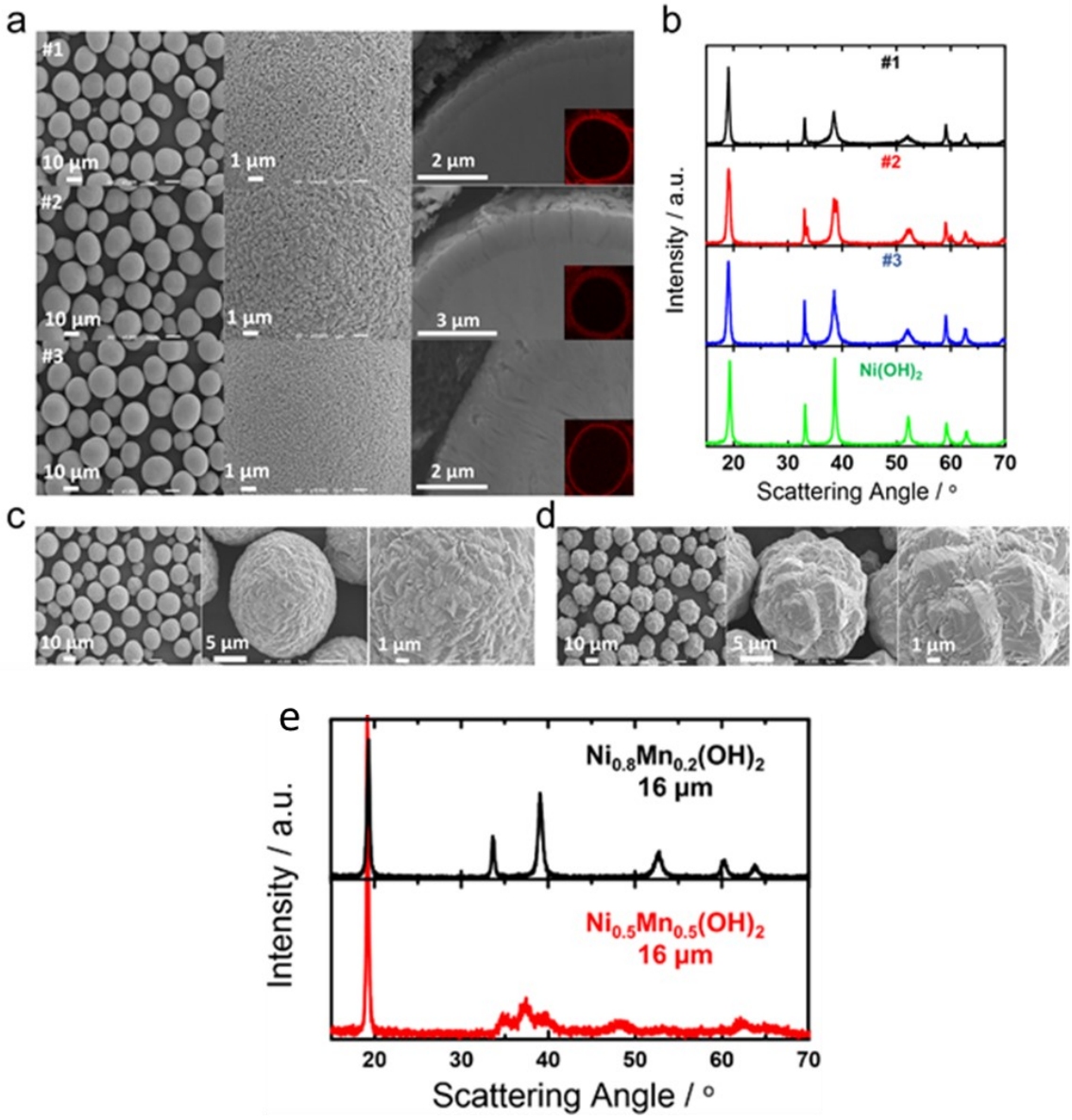

Figure 4.1 (a) SEM images of three core-shell precursors #1 to #3 from top to bottom. Inset images are cross-sectional Mn EDS mapping. (b) XRD patterns of the core-shell precursors and nickel hydroxide. (c) and (d) SEM images of the uniform "shell" precursors $Ni_{0.8}Mn_{0.2}(OH)_2$ and $Ni_{0.5}Mn_{0.5}(OH)_2$, respectively. (e) XRD patterns of the uniform "shell" precursors with 16 µm diameters.

4.3.2 Core-shell Structure Verification

Figure 4.2(a) shows SEM images of all three core-shell precursors after heating with $LiOH•H_2O$ at 650ºC to 800ºC for 20 hours. The SEM images indicate the spherical morphology of the precursor materials was maintained after heating with $LiOH•H_2O$. Figure 4.2(b) shows the morphologies of the lithiated "shell" precursors. All these images indicate no significant alteration of morphologies compared to their precursors.

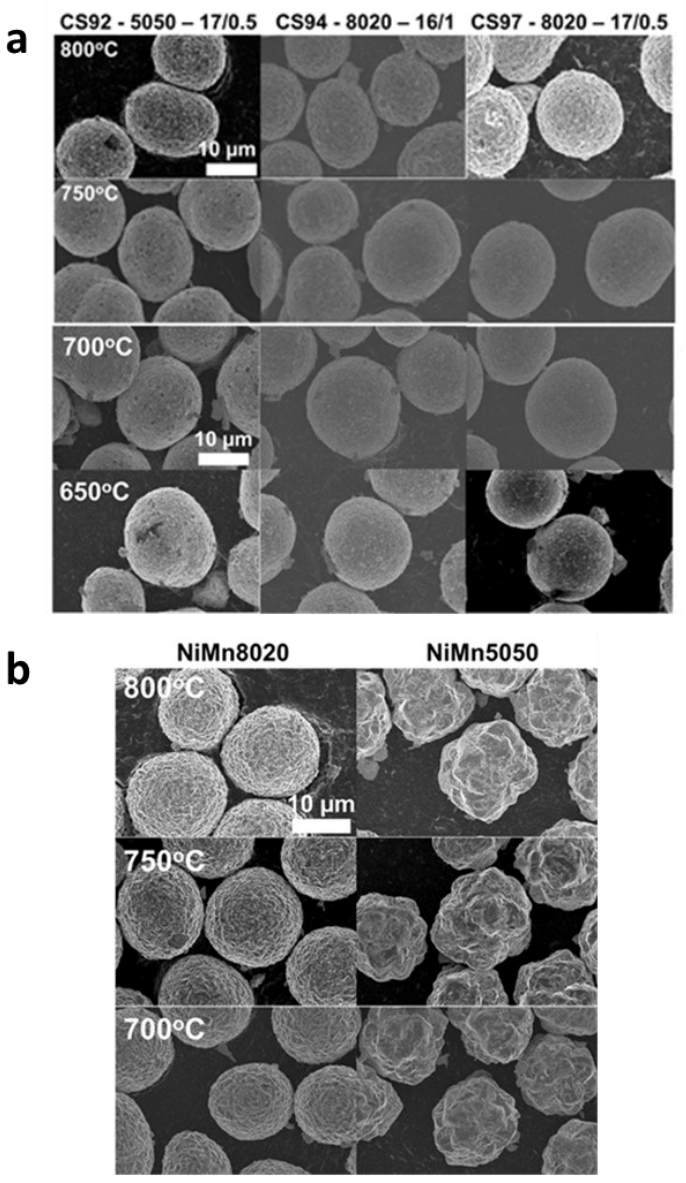

Figure 4.2 (a) SEM images of all three core-shell precursors after heating with $LiOH•H_2O$ at 650ºC to 800ºC for 20 hours. (b) SEM images of lithiated "shell" materials.

Figure 4.3 shows the cross-sectional SEM images, Mn EDS mappings and line scans of materials heated at 650°C to 800°C (bottom to top). The Mn line scans indicate the core-shell structure is maintained to some extent for CS92 at 800°C whereas, at the same temperature, CS94 and CS97 demonstrate a rather uniform Mn distribution, suggesting interdiffusion occurs at this temperature. Comparing CS92 (50% Mn in shell) to CS97 (20% Mn in shell), which have identical precursor shell thickness, a more Mn-rich shell is advantageous to maintain a core-shell structure at a higher heating temperature. At 750°C, the Mn EDS mapping and line scans for all three materials show much more prominent core-shell structure than those at 800°C, indicative of a lesser degree of interdiffusion. Well-defined core-shell structures remain at 700°C and 650°C for all three CS series.

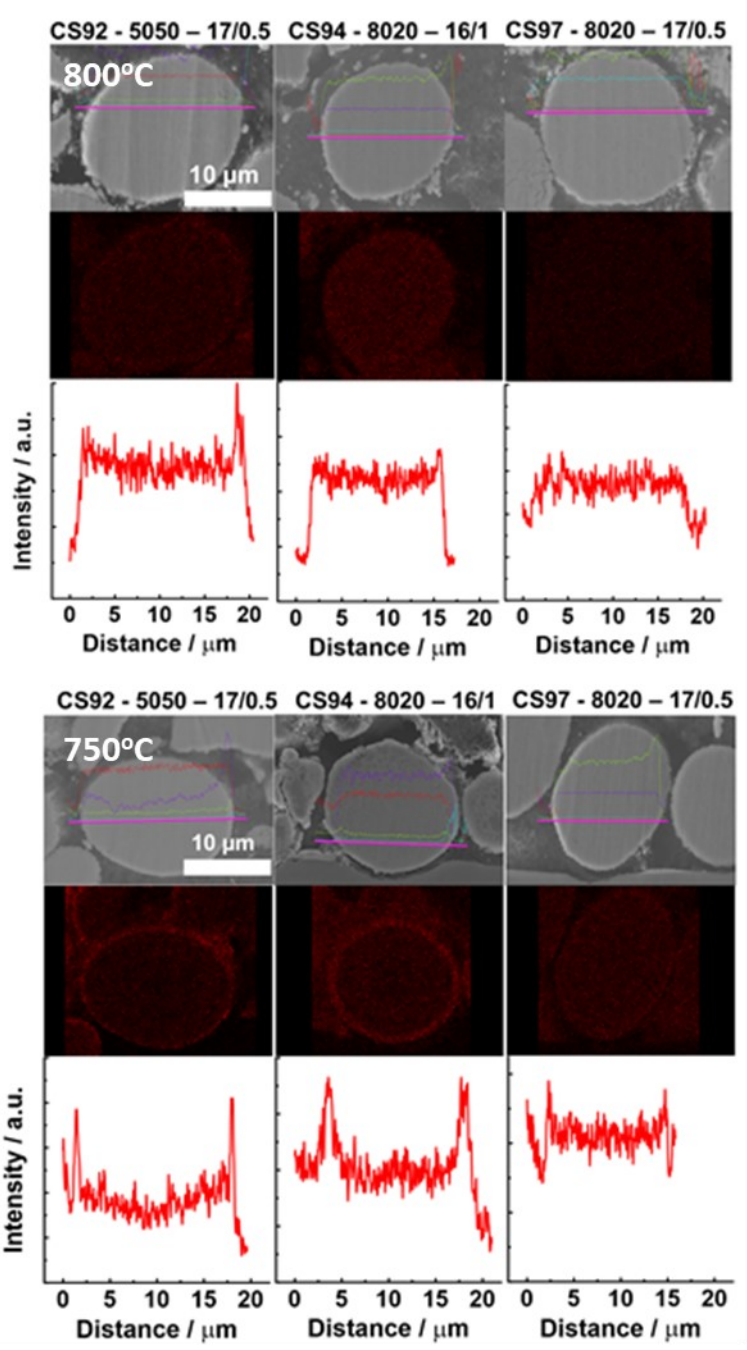
CS92 - 5050 – 17/0.5
CS94 - 8020 – 16/1
CS97 - 8020 – 17/0.5
800ºC
10 µm
Intensity / a.u.
0 5 10 15 20
Distance / µm
CS92 - 5050 – 17/0.5
CS94 - 8020 – 16/1
CS97 - 8020 – 17/0.5
750ºC
10 µm
Intensity / a.u.
0 5 10 15 20
Distance / µm

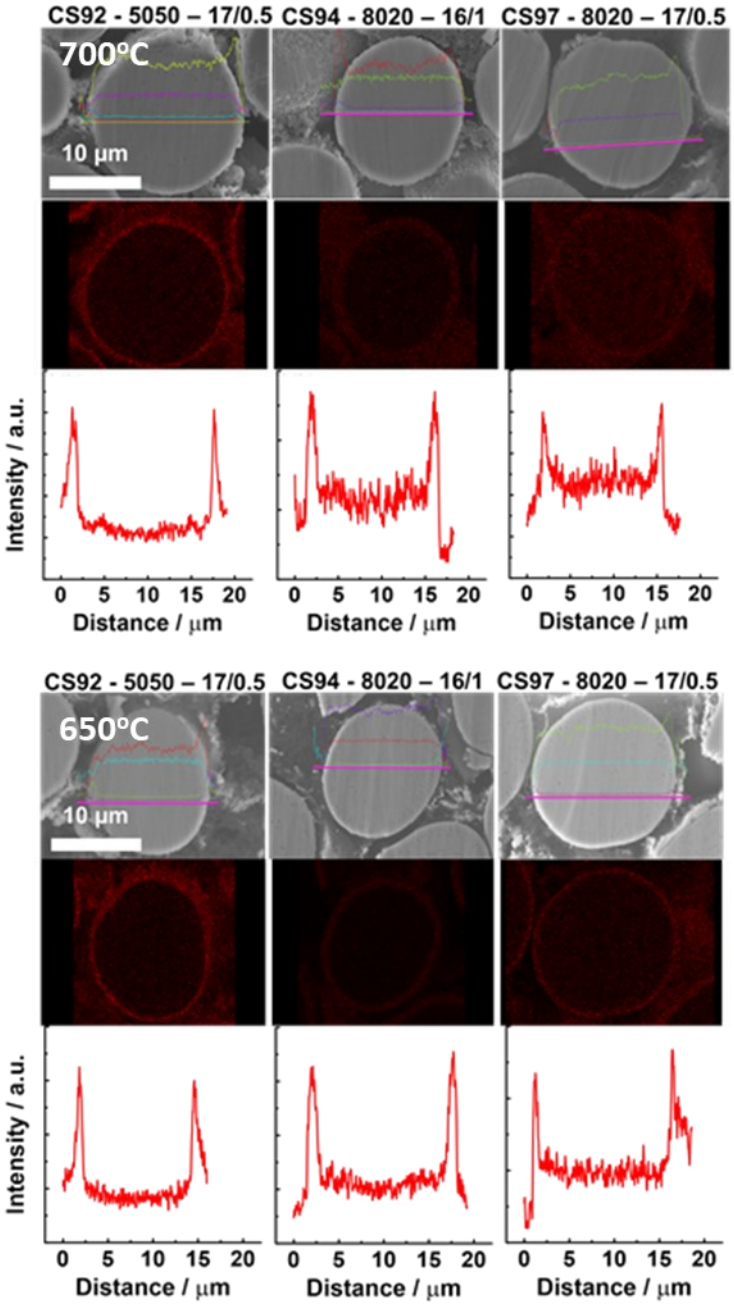

Figure 4.3 Cross-sectional SEM images, Mn EDS mapping and line scans of materials lithiated at 650°C to 800°C (bottom to top).

4.3.3 XRD and Refinement Results

Figure 4.4 shows the **average** lattice constants and percentage of Ni in Li layer (Ni_{Li}) from the Rietveld-refined XRD patterns as a function of lithiation temperature for all the materials made from core-shell precursors #1-3. Lattice constants and Ni_{Li} of the

corresponding "shell" materials, $LiNi_{0.5}Mn_{0.5}O_2$ and $LiNi_{0.8}Mn_{0.2}O_2$, denoted as NiMn5050 and NiMn8020 respectively, and $LiNiO_2$ taken from reference [63] are also included for comparison. All the refined XRD patterns can be found in Figure *A.1*. The XRD patterns from 20 to 35° scattering angle are free of any observable impurity peaks. An increased (108)/(110) Bragg peak splitting (near a scattering angle of 65°) at higher temperature indicates increased material crystallinity. However, for NiMn5050, its crystallinity does not seem to improve significantly at least up to 800°C.

The lattice constants and the percentage of Ni_{Li} of the CS92, 94 and 97 series all follow the same trends. Their lattice constant, a, varies little with heating temperature while the lattice constant, c, increases with heating temperature. Higher heating temperature decreases the average Ni_{Li} degree for the CS92, 94 and 97 series samples. If one assumes that Mn in the layered structure has an oxidation state of +4, Ni has to be partially reduced to Ni^{2+} from Ni^{3+} in order to maintain the average transition metal oxidation state of +3 in the layered structure. As a result, Ni_{Li} occurs due to the similar ionic radii of Ni^{2+}(0.69Å) and Li^{+}(0.73Å).[161] Therefore the CS97 series with only 3% Mn is expected to have the lowest average Ni_{Li} of all the CS series (a well-synthesized $LiNiO_2$ has a Ni_{Li} about 1%) which is exactly what is observed in Figure 4.4. Similarly, one expects NiMn5050 to have the highest percentage of Ni_{Li} followed by NiMn8020, which is consistent with Figure 4.4. Unlike any of the CS series and NiMn8020, heating up to 800°C does not lower the Ni_{Li} in NiMn5050 as a result of high Mn content. Both NiMn5050 and NiMn8020 show larger lattice constants than any of the CS series. High percentage of Ni_{Li}, and vice versa, allows more Li^{+}, which is larger than Ni^{3+}(0.7Å) to reside in the metal oxide slabs resulting in an increased lattice constant.

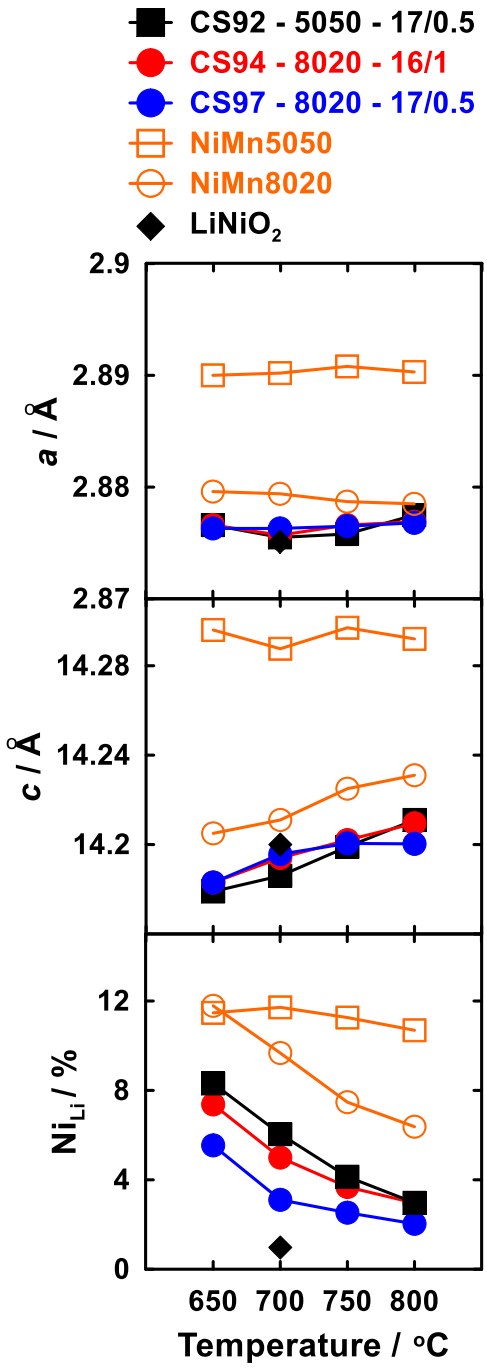

Figure 4.4 Rietveld-refined average lattice constants and average percentage of Ni in the Li layer, Ni_{Li}, as a function of lithiation temperature. NiMn5050 and NiMn8020 denote $LiNi_{0.5}Mn_{0.5}O_2$ and $LiNi_{0.8}Mn_{0.2}O_2$, respectively. Rietveld-refined XRD patterns of each sample are shown in Figure A.1. Lattice constants and Ni_{Li} for $LiNiO_2$ synthesized at 700°C were taken from reference 63.

4.3.4 Electrochemical Performance

Figure 4.5 shows the voltage vs. capacity (V-Q) curve of each material as a function of lithiation temperature. Specific capacity information is tabulated in Table A.1 to Table A.3 for the CS92, CS94 and CS97 series, respectively. At each temperature, the specific capacity increases from CS92 to CS97 as the Ni content increases. Within each CS series, the specific capacity sequentially increases from 650°C to 800°C while the voltage polarization becomes smaller, especially near the top of charge. The refinement results in Figure 4.4 show that the percentage of Ni_{Li} decreases from 650°C to 800°C. Less Ni_{Li} reduces voltage polarization at the top of charge as previously shown.[17,57,98] The dashed red rectangular regions in Figure 4.5 enclose the two CS materials that became approximately uniform after heating as Mn interdiffusion occurred substantially at 800°C according to Figure 4.3. The V-Q curve of the CS97 series at 800°C resembles that of pure Li_xNiO_2 which undergoes several phase transitions, believed to be detrimental for cycling, as x varies.[61,162,163] Irreversible capacity, in general, decreases as temperature gets higher. The irreversible capacity was reported to be related to slow diffusion of lithium due to the small number of di-vacancy sites in the lithium layer at high lithium content near the bottom of discharge.[164]

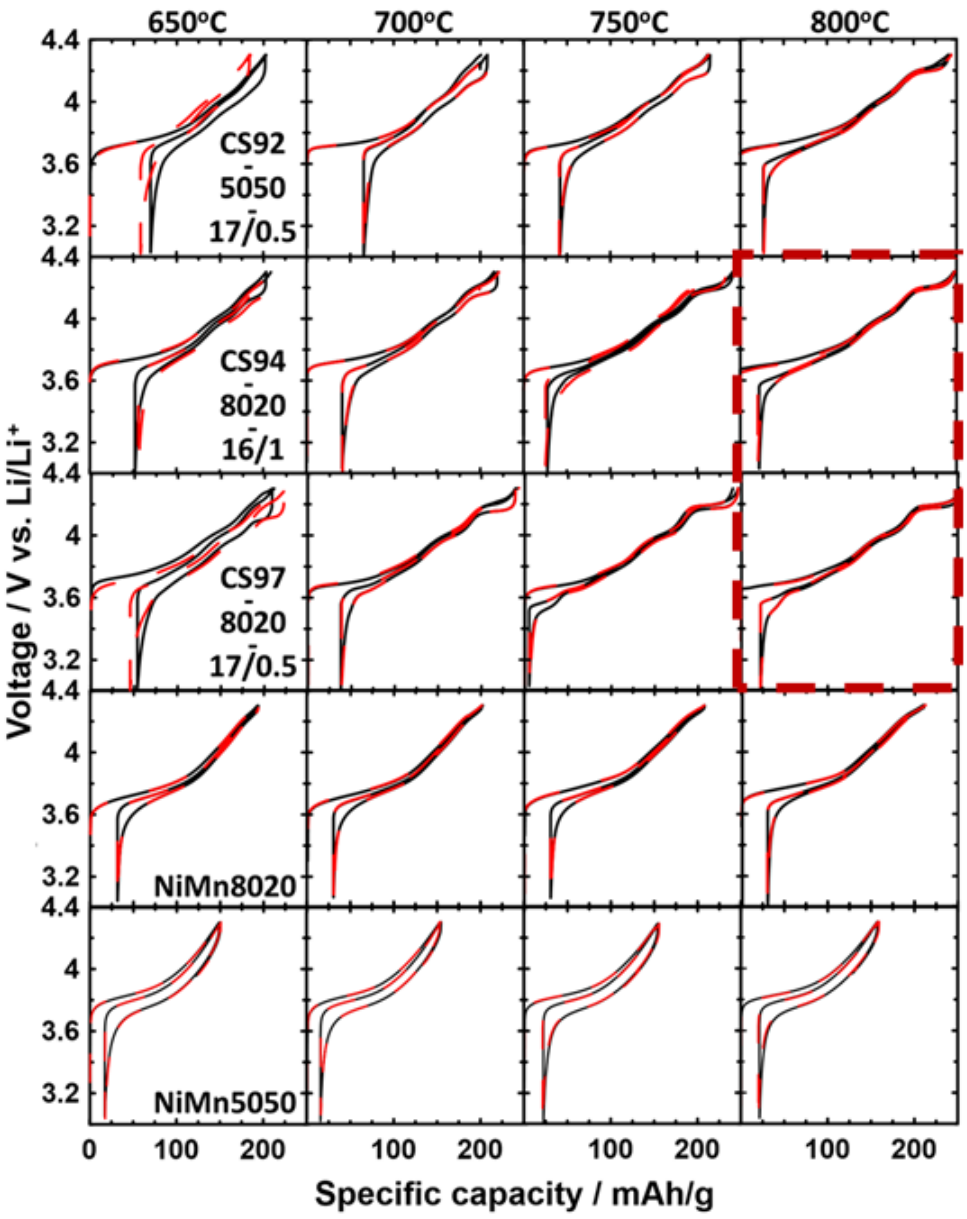

Figure 4.5 Voltage vs. capacity curve of each material as a function of lithiation temperature. Enclosed graphs (red dashed rectangle) are approximately uniform materials due to interdiffusion which occurred at high lithiation temperature. The black and red curves were measured from duplicate cells.

Specific capacity information for the uniform "shell" materials is tabulated in Table A.4 and Table A.5. The specific capacity of NiMn8020 increases with temperature. Both the specific capacity and voltage polarization of NiMn8020 are much weaker functions of

temperature compared to any of the CS series. The specific capacity of NiMn5050 is essentially unchanged from 650ºC to 800ºC and the voltage polarization remains high. This correlates to the XRD refinement results that show percentage of Ni_{Li} remains almost constant as the heating temperature increases. The V-Q plots of "shell" materials suggest that, for any CS series, the increase of specific capacity and reduced voltage polarization as a function of temperature is primarily due to the Ni-rich core.

Figure 4.6 relates the irreversible specific capacity (IRC) to the percentage of Ni_{Li}. The solid arrow and the dashed arrow point to the direction of increasing heating temperature for core-shell and "shell" materials, respectively. For the core-shell materials, the irreversible capacity is a strong function of Ni_{Li} as a small increase of Ni_{Li} such as 2% can lead to a significant rise in IRC. On the other hand, the IRC of the "shell" materials heated from 650ºC to 800ºC is almost unchanged with respect to Ni_{Li}. Therefore the Ni-rich cores of core-shell materials are most likely to be responsible for their strong dependency of IRC on Ni_{Li}. Both of the "shell" materials may require a heating temperature much higher than 800ºC to further lower their IRC under the synthesis condition in this study. $LiNiO_2$ synthesized at 700ºC was reported to have an IRC of ca. 25 mAh/g when charged to 4.3 V vs. Li/Li^+ at 30ºC.[63]

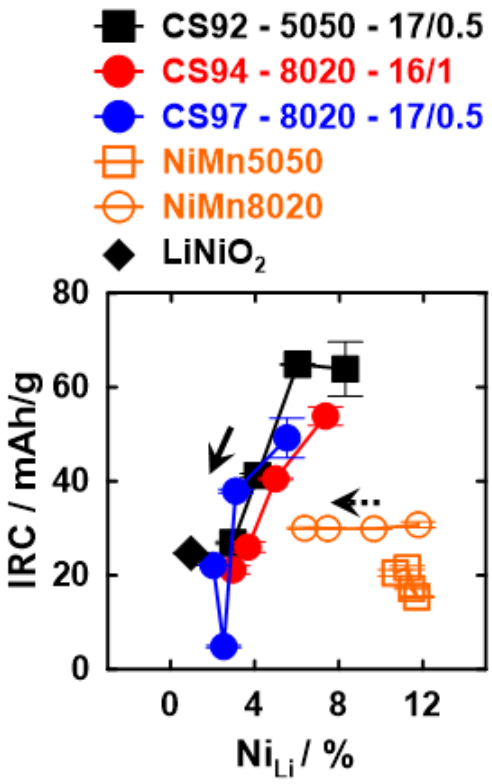

Figure 4.6 Irreversible specific capacity vs. percentage of Ni in Li layer, Ni_{Li}. Each IRC data point is the average of two coin-cells. The solid and dashed arrow point to the direction of increasing heating temperature of core-shell materials and the "shell" materials, respectively.

Figure 4.7(a) shows the charge-discharge cycling performance for the CS92, 94 and 97 series lithiated at different temperatures. The best performance of the CS92 and 94 series was achieved at the highest temperature with the core-shell structure still maintained. The best performing samples are CS92 at 800ºC and CS94 at 750ºC. However, for the CS97 series, the best performance was at 700ºC not at 750ºC which suggest the importance of having a sufficiently thick shell and/or Mn content in the shell after heating. The CS94 and CS97 series samples at 800ºC both had severely diminished shells due to interdiffusion and show poor cycling performance which are in sharp contrast to their counterparts heated at 750ºC. This illustrates the importance of a Mn-rich protective "shell" to achieve long cycle life of the Ni-rich core. The CS97 series at 800ºC has the worst charge/discharge cycling performance of all the CS series samples as expected since it is basically equivalent to uniformly 3% Mn doped material, $LiNi_{0.97}Mn_{0.03}O_2$.

Heating to higher temperature enhances the rate capability of all CS series, which can be observed as the decreasing specific capacity difference between the C/20 and the C/5 cycles. This correlates with the decrease in the percentage of Ni_{Li} that occurs with higher heating temperature.

Figure 4.7(b) examines the charge-discharge cycling stability of each CS series by comparing the C/20 dQ/dV vs. V profiles before and after cycling. The dQ/dV profile of an excellent material should be unchanged after cycling. In general, dQ/dV features (peaks) become increasingly prominent as a function of the lithiation temperature, especially the peaks at ca. 4.2 V are remnants of the H2 to H3 phase transition of $LiNiO_2$.[61] In this region, the unit cell volume changes dramatically and it is believed this can cause particle cracking for polycrystalline materials.[71,75,80] Of all the samples, the CS94 sample lithiated at 750ºC and the CS97 sample lithiated at 700ºC show the most stable dQ/dV peaks during cycling and these samples also have the best capacity retention in Figure 6a. The volume changes in a Mn-rich shell will be smaller than those in the core since the amount of lithium that can be extracted to 4.3 V becomes smaller as the Mn content increases.[57,165] Such a shell apparently protects the core and stable cycling ensues.

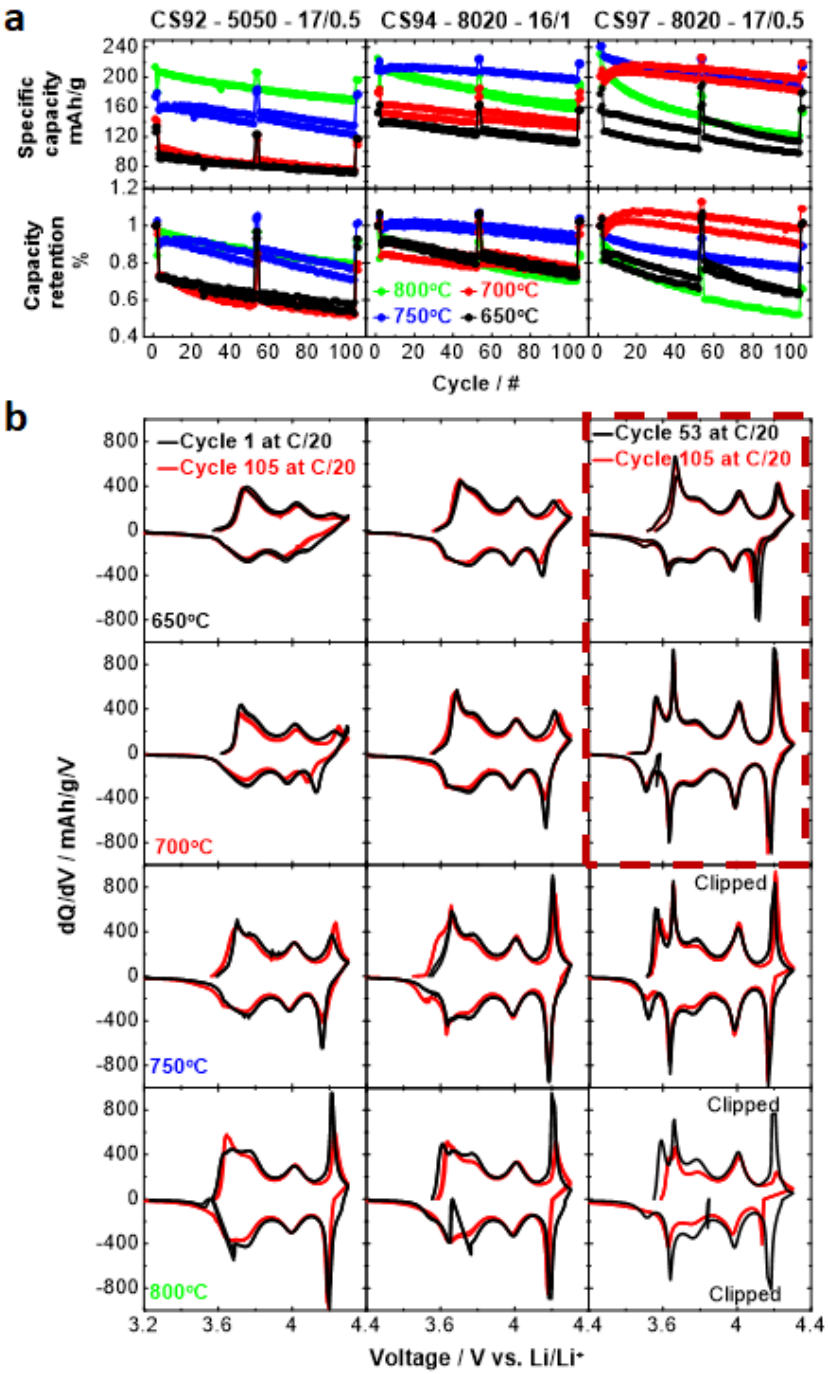

Figure 4.7 (a) Specific capacity and capacity retention vs. cycle number as a function of lithiation temperature. (b) Evolution of C/20 differential capacity before and after cycling. Enclosed region (dashed red rectangle) compares the 53rd cycle at C/20 (instead of cycle 1) to the 105th cycle at C/20 as specific capacity initially increased with cycles. The peaks at ca. 4.2 V that have intensities beyond the *y*-axis limits were "clipped" from the plots for clarity of presentation.

Figure 4.8(a) compares the cycling performance of the uniform "shell" materials to their corresponding CS series. At 650ºC and 700ºC, every CS series has very close specific capacity and capacity retention to its corresponding uniform "shell" material, except for CS97 at 700ºC. This implies that the heat treatment temperature is too low for the core to attain a small amount of Ni_{Li} and to develop its expected capacity. For CS97 at 700ºC, it not only has a core-shell morphology as shown in Figure 4.3 but also has a small average Ni_{Li} as shown in Figure 4.4, which can be the reason of why its performance stands out among all materials at 650ºC and 700ºC. Comparing the cycling performance of $LiNiO_2$ and CS97, taken from reference 63, the CS97 sample outperforms $LiNiO_2$ in terms of capacity retention even with 2% larger Ni_{Li} which indicates the significance of having a Mn-containing shell. At 750ºC all the CS series show much improved performance compared to the corresponding uniform "shell" materials as the average percent of Ni_{Li} gets smaller in all of them. However, careful examination of Figure 4.8(a) shows that CS97 has inferior capacity retention compared to CS94 which we believe is due to the near elimination of the shell in CS97 at 750ºC as shown in Figure 4.3, while CS94 has a clear Mn-rich shell. At 800ºC, all the CS94 and CS97 materials initially show higher specific capacity compared to the corresponding shell materials but their capacity retention is worse than the corresponding CS materials heated at 750ºC because the shell has been eliminated by interdiffusion at 800ºC (See Figure 4.3). By contrast, CS92 still retains some evidence of a shell after heating to 800ºC (See Figure 4.3) and Figure 4.8(a) shows that its capacity retention is similar to that of CS92 heated at 750ºC while its specific capacity is much larger due to a decrease in the average percentage of Ni_{Li}.

Figure 4.8(b) examines the electrochemical characteristics of the "shell" materials during charge-discharge cycling. The dQ/dV vs. V profiles of NiMn8020 change systematically with temperature as the specific capacity increases. In particular, the peak in dQ/dV vs. V at about 4.25 V sharpens as the temperature increases. Figure 4.4 shows that the percentage of Ni_{Li} is still decreasing between 750ºC and 800ºC suggesting an even higher heating temperature would be appropriate for NiMn8020 to simultaneously achieve higher specific capacity and lower Ni_{Li}. However, for a core-shell material, a higher temperature would lead to more rapid interdiffusion between core and shell and hence

inferior performance. On the other hand, neither the specific capacity nor the dQ/dV profile of NiMn5050 varies with heating temperature between 650ºC and 800ºC which is consistent with the relatively invariant percentage of Ni_{Li} for this material with temperature in Figure 4.4.

There are three factors which govern the behavior shown in Figure 4.8. Firstly, the core material, **nominally** $LiNiO_2$, needs to be heated to near 700ºC or 750ºC to attain a small amount of Ni_{Li} using the synthesis condition in this work. Percentages of Ni_{Li} in $LiNiO_2$ as low as 1% have been also attained in oxygen at 700ºC by de Biasi et al.[162] and at 750ºC by Kobayashi et al.[163] If $LiNiO_2$ is heated to higher than 750ºC, then lithium loss occurs[166,167] and lithium deficient materials with significant Ni_{Li} will likely result. If $LiNiO_2$ is heated at temperatures lower than 700ºC, it is difficult for a perfect layered structure to form leading to cation mixing between Ni and Li and hence, resulting more Ni in the Li layer. Secondly, the shell materials which contain 20% or 50% Mn need to be heated to temperatures at least to 800ºC to attain optimum properties, which is evident in Figure 4.8(a) by their steadily increasing specific capacities with temperature. Lastly, the interdiffusion between the Mn rich shell and the core proceeds at a significant rate beginning at 700ºC, therefore if a shell is too thin or contains too little Mn, it will not remain when the temperature is too high. It is clear from Figure 4.3, Figure 4.7 and Figure 4.8 that a Mn-rich shell is desired for the best capacity retention.

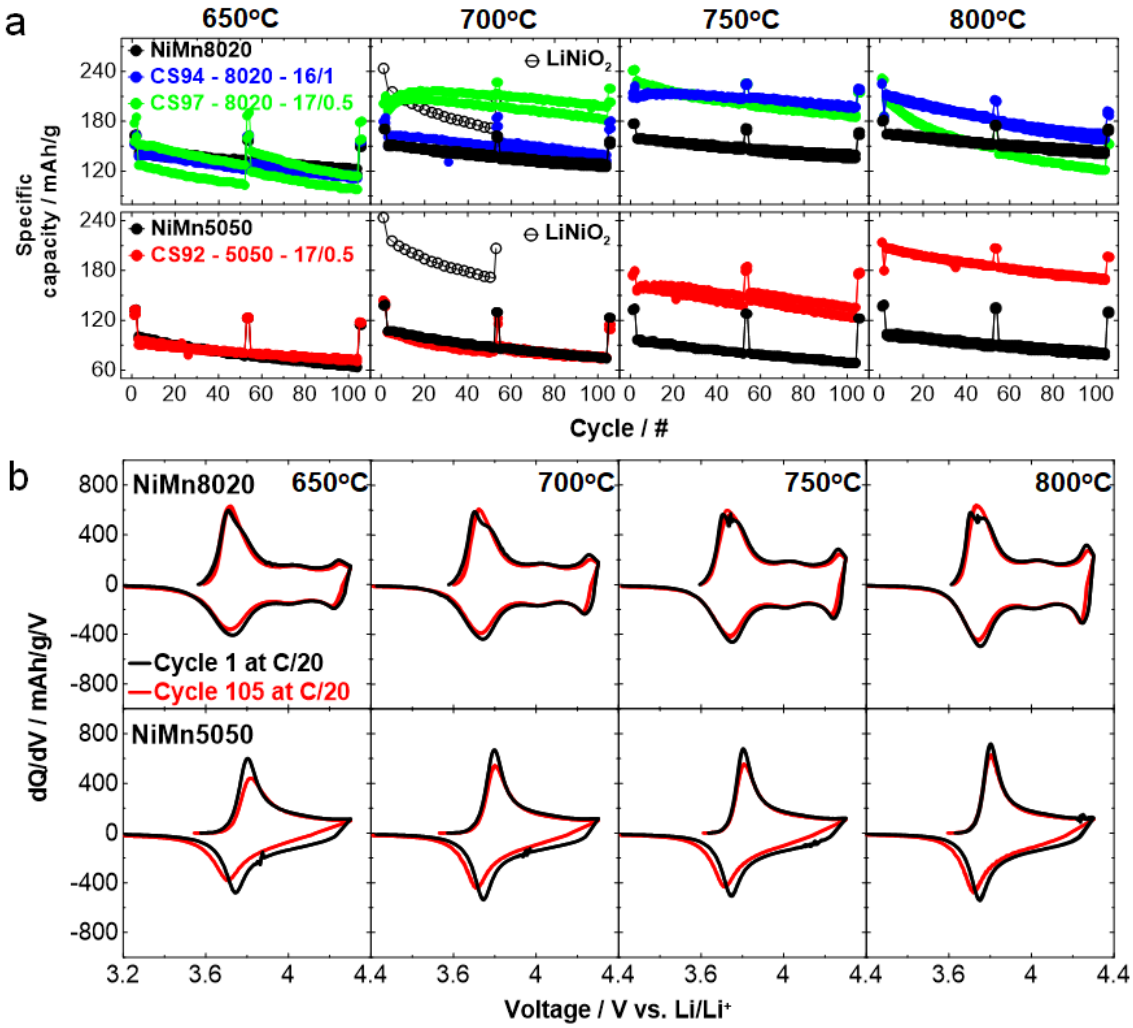

Figure 4.8 (a) Cycling performance comparison of the "shell" materials to the corresponding CS series. Cycling was performed under the same condition as this work. (b) Evolution of C/20 differential capacity before and after cycling of NiMn8020 and NiMn5050 at various lithiation temperatures.

Figure 4.9 summaries the specific capacity and capacity retention at the 100th cycle of each material as a function of the lithiation temperature. To attain high specific capacity from the Ni-rich core, heating temperatures near 700°C to 750°C are necessary, but the highest specific capacity and capacity retention are attainable only with a core-shell structure. The CS94 and CS97 series show their best performance at 700°C and 750°C, respectively, and beyond these temperatures, their performance deteriorated as a result of a diminishing shell. In contrast, the performance of the CS92 series keeps increasing as a

function of temperature most likely because of the very high Mn content originally in the shell. If heated far beyond the highest temperature studied in this work, it is likely the CS92 series would have worse capacity retention because the core-shell structure would not survive.

Apparently, the optimal temperature is closely associated with the shell thickness and Mn content. Comparing the optimal temperature of the CS97 series to the CS94 series, both of which have identical shell composition, the CS97 series performs the best when heated at 700ºC, 50ºC lower than the best of the CS94 series when heated at 750ºC. This is due to Mn interdiffusion almost eliminating the thinner shell in CS97 when heating to 750ºC. In general, a thicker shell helps maintain the core-shell structure but with a trade-off as more Mn content in the material lowers the specific capacity. It is very likely that a core-shell material with optimized shell thickness and Mn content can perform even better than CS94 at 750ºC, the best performing material in this chapter.

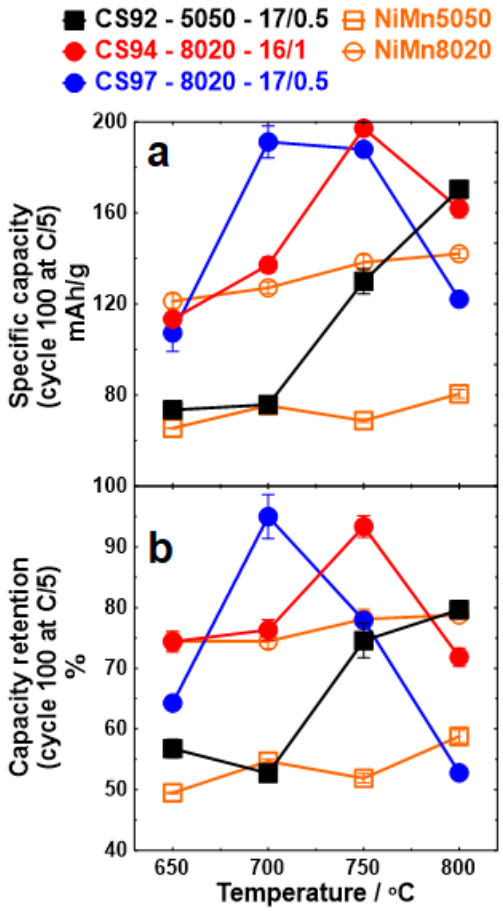

Figure 4.9 Specific capacity (a) and capacity retention (b) of all materials at cycle 100 as a function of lithiation temperature. Testing was performed at 30°C between 3.0 and 4.3 V.

4.4 Conclusions

Core-shell precursors with a $Ni(OH)_2$ core and either a $Ni_{0.8}Mn_{0.2}(OH)_2$ or $Ni_{0.5}Mn_{0.5}(OH)_2$ shell were heated with $LiOH{\bullet}H_2O$ at temperatures from 650°C to 800°C. The impact of shell composition and thickness on the structure and properties of the resulting materials was explored by cross-sectional EDS, XRD and charge/discharge cycling. Each CS series showed an increased specific capacity when heating to higher temperature. However, the shell completely disappeared when the temperature became too high due to Mn interdiffusion. When this occurs, the material simply becomes a uniformly doped Ni-rich material with poor cycling performance. The highest temperature a core-shell precursor can be heated while still maintaining a well-defined core-shell structure depends on the shell thickness and its Mn content. To attain both a

high specific capacity and excellent cycle life for a core-shell material, optimized shell thickness, Mn content and heating temperature are necessary.

The best material created in this chapter started with a 16 μm diameter core of $Ni(OH)_2$ covered by a 1 μm thick shell of $Ni_{0.8}Mn_{0.2}(OH)_2$. This was heated with $LiOH•H_2O$ at 750^oC to make a layered core-shell material which was confirmed by EDS mapping and EDS line scans. After 100 charge discharge cycles, the specific capacity at C/5 was ca. 200 mAh/g and the capacity retention was about ca. 93%.

Chapter 5 Comparison of the "Best" Core-shell Material with Commercial-grade Co-containing Ni-rich Layered Materials

5.1 Introduction

In Chapter 4, the "best" performing core-shell material was made with a 16 μm diameter core of $Ni(OH)_2$ covered by a 1 μm thick shell of $Ni_{0.8}Mn_{0.2}(OH)_2$. (CS94-8020-16/1) followed by heating with $LiOH•H_2O$ at 750ºC for 20 hours. In this chapter, the performance of this core-shell material is compared to that of the commercial-grade Co-containing Ni-rich materials in terms of cation mixing, charge-discharge cycling, powder electrical resistivity, and DCR tests.

The results of this chapter was incorporated into a manuscript published in the *Journal of the Electrochemical Society* with open access.[17]

5.2 Experimental

For simplicity of discussion, CS94-8020-16/1 synthesised at 750ºC and 800ºC are named CS750 and CS800, respectively, in this chapter. $Li[Ni_{0.8}Co_xAl_{0.2-x}]O_2$ (NCA) powder with 80% Ni was received from Umicore and used without further treatment. Single crystal $Li[Ni_{0.8}Co_{0.1}Mn_{0.1}]O_2$ (SC811) powder was received from a reputable vendor and used without further treatment. The SC811 and polycrystal $Li[Ni_{0.8}Co_{0.1}Mn_{0.1}]O_2$ (PC811) electrodes were harvested from dry (no electrolyte) commercial-grade pouch cells. The as-received pouch cells were cut open and the jelly roll was removed from the pouch. The jelly roll was unwound and the single-side-coated region of the positive electrode was punched into 12 mm diameter discs. The punched electrode discs were incorporated into coin cells for charge-discharge cycling and other tests. The electrodes have a formulation of 94:4:2 (active material: conductive carbon: binder) and a loading of 21 mg cm^{-2}.

5.3 Results and Discussion

5.3.1 XRD and Refinement Results

Figure 5.1 shows the XRD patterns of CS-750 (a) and CS-800 (b), along with those of commercial-grade SC811 (c) and NCA (d) from different vendors. The exact Co and Al

composition of NCA were not disclosed to the authors. The Rietveld refinements were performed on the XRD data assuming a hexagonal layered phase having the $R\bar{3}m$ space group (α-$NaFeO_2$) to extract lattice constants and percentage of Ni in the Li layer (Ni_{Li}) information. The black circles are the measured diffraction data and the red lines are the fitted XRD patterns from Rietveld refinement. The green lines show the difference between the measured and fitted XRD data. Both XRD patterns of the core-shell CS-750 and the approximately uniform CS-800 were refined with a uniform composition which gives average lattice constants and average Ni_{Li}. The (003) and (104) Bragg peaks of CS-800 are sharper and narrower (in full width half max (FWHM)) than those of CS-750. McCalla et al.,[168] when studying the pseudoternary Li-Mn-Ni oxide system, suggested the peak broadening could be a result of multiple phases with slightly different lattice parameters. This is expected since CS-800 does not retain a core-shell structure while CS-750 does. H. Li et al.[57] showed that the lattice constants of $LiNi_{1-x}Mn_xO_2$ varies as a function of x. We expect CS-750 to show broader peaks since it is a mixed phase with $x \approx 0$ in the core and $x \approx 0.2$ in the shell. Both materials show no sign of any impurities, for instance, the strongest peaks from a typical impurity, Li_2CO_3, are not observed in the 20^o to 35^o region. XRD patterns of commercial-grade SC811 and NCA demonstrate a higher crystallinity than CS-800 as indicated by the (104) and (108)/(110) Bragg peaks splitting due to the K_α doublet. Both materials are free of any impurities.

Table 5.1 summaries the refinement results of the XRD patterns in Figure 5.1. The values in the table are those of the **average** structure of CS-750. By increasing the lithiation temperature from 750ºC to 800ºC, the a-axis lattice constant remains almost unaffected (number in the parenthesis represents the uncertainty of the last digit). The c-axis lattice constant increases slightly from 14.202 to 14.210 Å. Lithiation at 800ºC also decreased the percentage of Ni in the lithium layer (Ni_{Li}) by ca. 0.7% compared to heating at 750ºC. However, this decrease may be spurious because the results for CS-800 are being compared to a refinement to the **average** structure of CS-750. It is reasonable to assume that for CS-750, the large average value of Ni_{Li} is dominated by the shell as a result of a significantly higher Mn content than the core. Commercial-grade SC811 and NCA show low Ni_{Li} which agrees with the previously observed high crystallinity from their XRD

patterns. Core-shell precursors heated to higher than 800ºC with LiOH•H_2O are believed to be capable of obtaining a higher crystallinity and even lower Ni_{Li} than CS-750, however the core-shell structure will not be maintained.

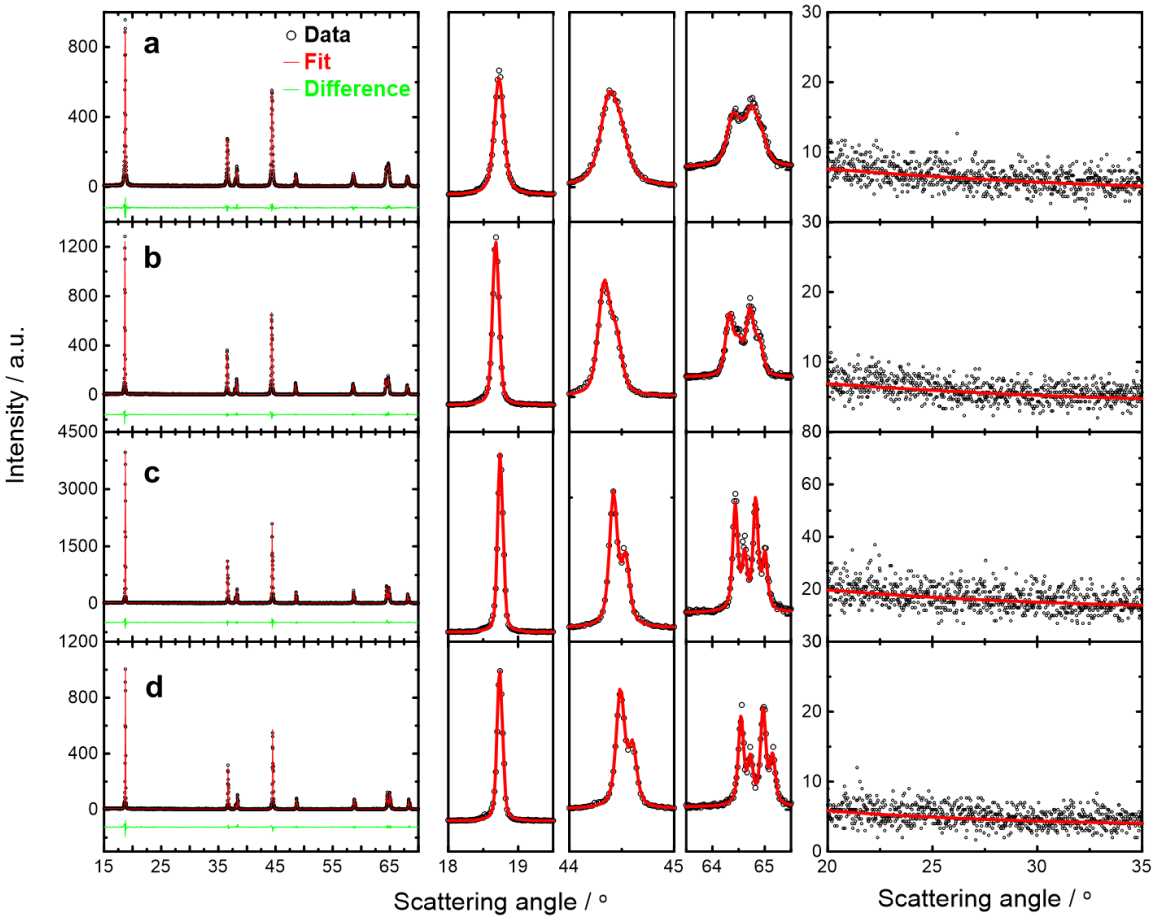

Figure 5.1 Rietveld-refined XRD patterns of CS–750 (a), CS–800 (b), commercial-grade SC811 (c) and NCA (d). From left to right: full XRD pattern from 15º to 70º, the corresponding expanded views of (003) Bragg peak, (104) Bragg peak, and (108)/(110) Bragg peaks, and the impurity region. NCA is assumed to have a composition of $Li[Ni_{0.8}Co_{0.1}Al_{0.1}]O_2$ for refinement purposes only.

Table 5.1 Rietveld refinement results for CS-750, CS-800, SC811 and NCA

Sample	Lattice constant *a* [Å]	Lattice constant *c* [Å]	Ni_{Li}[a)] [%]	$FWHM_{(003),\ (104)}$[b)] [°]	R_b
CS-750	2.87660(9)	14.2023(9)	3.68	0.142, 0.193	1.41
CS-800	2.87690(6)	14.2100(6)	2.97	0.0786, 0.131	1.51
SC811	2.87430(4)	14.1953(5)	1.50	0.0500, 0.0880	1.65
NCA[c)]	2.86730(5)	14.1710(5)	1.47	0.0540, 0.0920	2.67

[a)] Percentage of Ni in the Li layer; [b)] Full width half max of (003), (104) Bragg peaks. Each peak was fitted with a K_α doublet and the reported values are the FWHM of the $K_{\alpha1}$ peak; [c)] NCA - $Li[Ni_{0.8}Co_{0.1}Al_{0.1}]O_2$ (assumed 10% of Co and 10% of Al for the purposes of refinement).

5.3.2 Long-term Charge-discharge Cycling Performance

Figure 5.2(a) shows the voltage vs specific capacity (V vs Q) curves from 3 to 4.3 V vs Li/Li^+ for the first 1.5 C/20 cycles of commercial-grade SC811, PC811, CS-750 and CS-800. The NMC811 samples have a reversible capacity of ca. 210 mAh g^{-1} which is slightly lower than those of CS-750 (220 mAh g^{-1}) and CS-800 (225 mAh g^{-1}). The specific capacity of CS-800 is higher than CS-750 which may be due to less Ni_{Li}. The larger voltage hysteresis (circled region), which is more pronounced at the top of charge, of CS-750 is believed to be caused by large amounts of Ni_{Li} as seen in other reports.[57,98]

$dQdV^{-1}$ vs V curves are able to reveal more details about the samples than their voltage curves. Figure 5.2(b) shows the 1st discharge and 2nd charge differential capacity vs voltage curves ($dQdV^{-1}$ vs V) of the samples described by Figure 5.2(a). $dQdV^{-1}$ vs V plots of NMC811 (both SC811 and PC811) with maxima found at 3.62, 3.75, and 4.22 V vs Li/Li^+ during charging are consistent with those reported in the literature.[9,18] In comparison to NMC811, the core-shell materials have more prominent $dQdV^{-1}$ vs V features above 3.9 V vs Li/Li^+. Both core-shell materials have very sharp $dQdV^{-1}$ peaks at around 4.2 V in both charging and discharging curves. A wider peak separation of about 30 mV (gap between vertical dashed lines) was observed for CS-750 whereas it was only about 15 mV for CS-800, which matches the increased hysteresis in the voltage profile.[57,97]

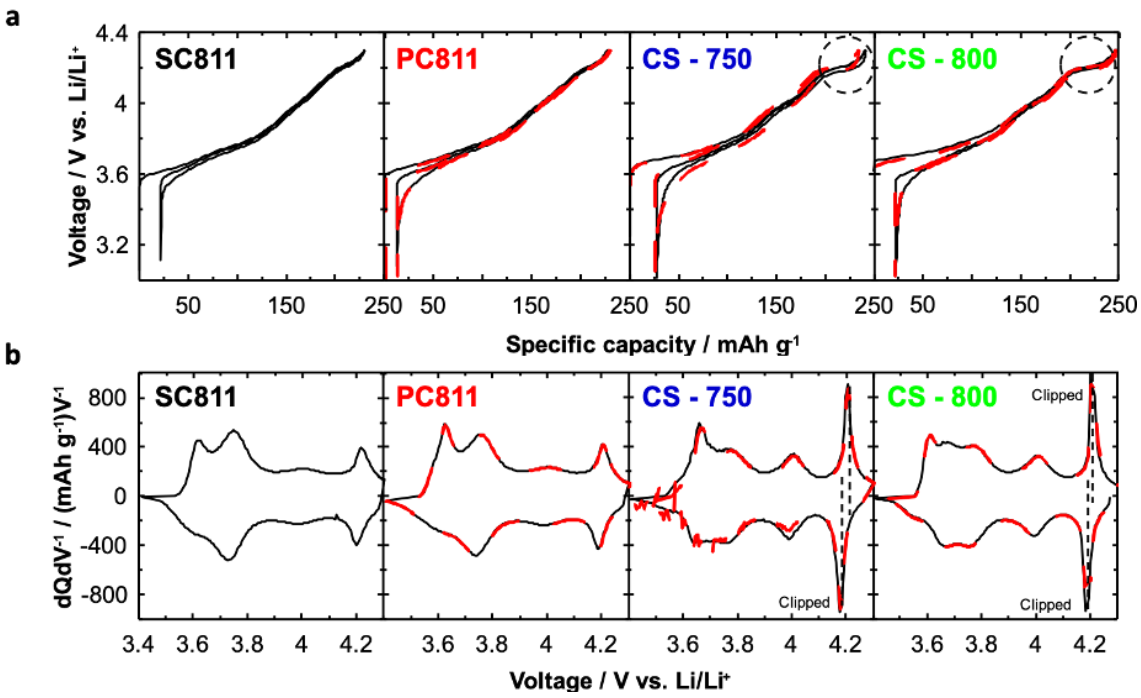

Figure 5.2 (a) Voltage versus capacity curves from 3 to 4.3 V vs Li/Li^+ SC811, PC811, CS-750 and CS–800, respectively. (b) Corresponding differential capacity ($dQdV^{-1}$) versus voltage curves. These tests were done at 30ºC. The black solid line and the red dashed line represent data for pair cells.

Figure 5.3(a) compares the charge-discharge cycling performance of SC811, PC811, CS-750 and CS-800. SC-811 and PC-811 show almost identical capacity retention. CS-750, with a well-defined core-shell structure, shows higher specific capacity and comparable capacity retention to these commercial-grade NMC811 samples. Although CS-800 has higher initial C/20 reversible capacity than CS-750, its capacity retention is much inferior to CS-750. CS-800 has a severely diminished core-shell structure due to Mn diffusing into the core during lithiation at 800ºC shown previously in Figure 4.3, therefore it is approximately equivalent to 6.5% Mn-doped $LiNiO_2$ ($LiNi_{0.935}Mn_{0.065}O_2$). Without proper protection from a Mn-doped shell, the cycling performance of CS-800 is worse than NMC811 and CS-750. This is consistent with results on ultra-high Ni materials with over 90% Ni (Note: the average composition of the transition metals in CS-750 and CS-800 is 93.5% Ni and 6.5% Mn).

Figure 5.3(b) shows the corresponding C/20 and C/5 $dQdV^{-1}$ vs V plots at some selected cycle numbers. $dQdV^{-1}$ plots at C/20 minimize the impact of polarization on the data. The $dQdV^{-1}$ profiles of SC-811 and PC811 are almost unchanged after cycling which demonstrates high stabilities of these commercial-grade materials. CS-750 shows a slight capacity increase in the 53rd cycle (C/20) below 3.65 V vs Li/Li^+. The origin of this slight capacity increase is not known at this moment, however capacity increase during initial stage of cycling is not uncommon as seen in some reports.[159,169] The $dQdV^{-1}$ profiles of CS-750 remain very stable until the end of cycling. CS-800, which has a relatively uniform composition, experiences a gradual decrease of capacity especially around the 4.2 V region which is the most significant contributor to the overall CS-800 capacity loss. C/5 $dQdV^{-1}$ profiles take the impact of polarization into account. The $dQdV^{-1}$ profiles of PC811 at C/5 are relatively stable without any shift of peak positions except for a decrease of the intensity of the peak at around 3.65 V. SC811, however, shows an increase in the onset charging voltage and a slight decrease of the onset discharging voltage which indicate an increase in polarization. The $dQdV^{-1}$ vs V data for CS-750 shows that its rate capability is very well maintained throughout the cycling with only a slight decrease in the intensity of the of 4.2 V during charge. By contrast, a significant loss of rate capability is observed for CS-800 particularly at the 4.2 V region where severe $dQdV^{-1}$ vs V peak shifts and intensity decrease occur.

The evolutions in the $dQdV^{-1}$ profiles around 4.2 V vs Li/Li^+ as a function of cycle number suggest that the CS-750 has a greater structural stability than CS-800. The series of CS-750 and CS-800 $dQdV^{-1}$ peaks can be treated as remnants of the phase transitions that occur in Li_xNiO_2 as a function of x.[61] The peak at 4.2 V vs Li/Li^+ is a remnant of the H2 to H3 phase transition which is detrimental to cell cycling and is believed to be associated with particle microcracking.[89] Whether a core-shell structure is indeed robust to microcracking requires further verification. However, J. Li et al,[165] via *in-situ* XRD, suggested a core-shell structure with Ni-rich core and Mn-rich shell should be very stable upon cycling as a result of a lower degree of unit cell contraction and expansion of the shell material compared to a Ni-rich core. Other studies have demonstrated the robustness of the core-shell structure through cross-sectional imaging on cycled materials.[85,91,170]

The only difference between CS-750 and CS-800 lies in the heating temperature where CS-750 is able to maintain its core-shell structure while CS-800 is not. The improved cycling of CS-750 over CS-800 can be therefore attributed to the Mn-doped shell which CS-800 lacks.

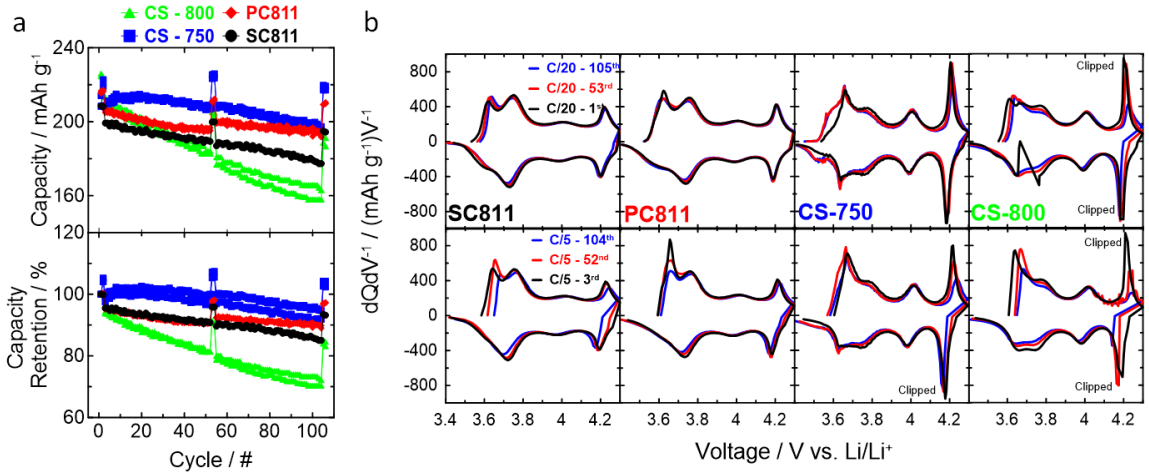

Figure 5.3 (a) Discharge capacity and capacity retention versus cycle number of SC811, PC811, CS–750 and CS–800. Each material was tested in pair half cells at currents corresponding to C/5. C/20 capacity was measured at the beginning of the cycling for 2 cycles, at the 53rd and 54th cycle, and 2 cycles at the end of cycling. (b) Differential capacity (dQdV^{-1}) versus voltage curves of C/20 (top row) and C/5 (bottom row) at various stages of cycling. These tests were done at 30^{o}C from 3 to 4.3 V.

5.3.3 Powder Electrical Resistivity and DCR Measurement

Figure 5.4(a) compares the powder electrical resistance of Co-containing commercial materials and Co-free core-shell materials as a function of applied pressure. All the data was measured in the same apparatus in the same manner. The powder resistances of all tested materials reduce monotonically as the pressure increases. Commercial-grade NCA powder (80% Ni) has the lowest powder resistivity among all the materials. However, upon applying a higher pressure, the powder resistances of NCA and the core-shell materials gets increasingly similar. This suggests that in a practical situation where engineers aim to achieve high electrode loading or density with thousands of atmospheres of calendaring pressure, the impact of different powder resistivity on electrode rate

capability could even be negligible. The powder resistance of SC811 (scraped from electrodes with 4% conductive carbon and 2% PVDF binder) shows a much higher value than the core-shell materials.

It is tempting to examine the direct current resistance (DCR) of electrodes made from these powders. The SC811 electrodes with 21 mg cm^{-2} and 94% active material were directly punched from the single-side-coated region of a dry (no electrolyte) commercial-grade pouch cell for DCR measurements. For a fair comparison, NCA, CS-750 and CS-800 electrodes were prepared with the same loading and percentage of active material, and their DCR results are shown in Figure 5.4(b) plotted against state of charge (SOC). Initial DCR measurements were performed on coin cell half cells right after 1.5 cycles at C/20 at 40ºC, then cells were run for 30 C/10 cycles and DCR measurements were conducted again. All the DCR plots show relatively high resistances at low (< 20%) and high (> 90%) SOC before and after cycling. If only comparing the DCR between 30% and 90% SOC from the initial measurements, CS-750 is very close to NCA having DCR almost constant with voltage. CS-800 shows a similar trend but slightly higher DCR than CS-750. SC811 has highest DCR among all, particularly at high SOC. Both commercial materials show quite stable DCR performance between 30% and 90% SOC even after cycling. A significant DCR increase can be observed at the low SOC. Though CS-750 has a slight DCR increase after cycling, its overall DCR still remains relatively small and outperforms the commercial materials at low SOC. However, for CS-800, which has the highest Ni content with approximately uniform structure, its DCR increase after cycling is the largest among all the materials. Figure 5.4(c) shows the capacity retention vs cycles after initial DCR measurement which matches the half cell cycling performance shown in Figure 5.3(a).

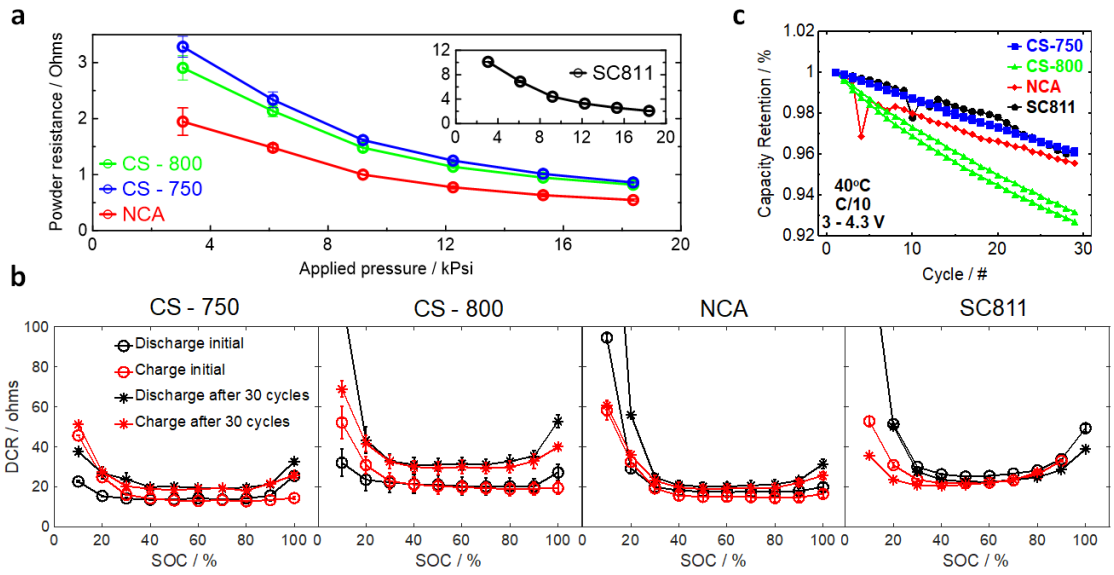

Figure 5.4 (a) Powder electrical resistance versus applied pressure. (b) direct current resistance (DCR) versus state of charge (SOC) of NCA, SC811, CS–750 and CS–800 at 40°C before and after 30 C/10 cycles. (c) Capacity retention versus cycle number for NCA, SC811, CS–750 and CS–800 at 40°C and C/10 from 3 to 4.3 V. Each material was tested with pair cells.

5.4 Conclusions

In this chapter, a core-shell structure was demonstrated to be capable of mitigating the typically poor cycle life of Ni-rich material while maintaining high specific capacity. A Co-free core-shell precursor with a $Ni(OH)_2$ core and a $Ni_{0.8}Mn_{0.2}(OH)_2$ shell was lithiated at 750°C (CS-750) and 800°C (CS-800). CS-750 with a well-defined core-shell structure, shows comparable capacity retention with commercial-grade NMC811 and higher specific capacity, while CS-800, with a severely diminished core-shell structure, shows much inferior capacity retention to both CS-750 and NMC811. CS-750 and CS-800 have also displayed comparable DCR with NCA and SC811, indicating that Co is not required to attain comparable DCR.

Chapter 6 An Evaluation of a Systematic Series of Cobalt-free Ni-rich Core-Shell Materials

6.1 Introduction

In Chapter 4 and Chapter 5, it was shown that Co-free core-shell materials can have comparable cycling performance and direct current resistance to commercial single crystal $LiNi_{0.8}Mn_{0.1}Co_{0.1}O_2$, highlighting the potential of Co-free core-shell materials as promising alternative positive electrode materials. In this chapter, a systematic evaluation of the performance of Co-free core-shell materials as a function of core size, shell thickness, core/shell compositions and heating temperature was conducted. Results were then compared with historical data from other layered Ni-rich Co-free materials tested in the Dahn group within the past few years.[63] A relationship between the cycling performance of core-shell materials and the heating temperature during synthesis is proposed in this chapter. This relationship considers the crystallinity of the material, the average percentage of Ni in the Li layer and the presence or absence of the shell phase after the heating step. Finally, the reactivity of the charged electrode materials with electrolyte was measured using accelerating rate calorimetry experiments to explore the influence of shell composition and thickness, heating temperature, etc. This chapter aims to provide an overview of Co-free core-shell material performance.

The results of this chapter was incorporated into a manuscript published in the *Journal of the Electrochemical Society* with open access.[8] The ARC/BET measurements were conducted by Dongxu Ouyang. Divya Rathore contributed greatly to the lithiation of core-shell precursors.

6.2 Experimental

14 core-shell precursors containing only Ni and Mn were provided by Zoomwe (Hunan Zoomwe Zhengyuan Advanced Material Trade Company, Ltd., Changesha 410000, China). The core and shell compositions, the core sizes, shell thicknesses and the average Ni contents are listed in Table 6.1. Precursors #1 to 11 were not reported before and precursors #12 – 14 have been reported in Chapter 4 and Chapter 5. The lithiated

materials have been divided into 4 groups for ease of discussion. Group I (#1 to 4) materials were made from precursors that all have a $Ni_{0.98}Mn_{0.02}(OH)_2$ core and a $Ni_{0.8}Mn_{0.2}(OH)_2$ shell composition. The only differences among materials in Group I are the core diameter and shell thickness. Groups II (#5 to 7) and III (#8 to 11) materials were all made with a $Ni(OH)_2$ core composition. Group II materials have larger core sizes whereas Group III materials all have an 8 μm core diameter. Group IV (#12 to 14) materials are from the precursors studied in Chapter 4 and Chapter 5.

For precursors #12 – 14, the performance of the lithiated oxides made at temperatures between 650 and 800°C have been reported in previous chapters along with the performance of the homogeneous "shell" materials $LiNi_{0.8}Mn_{0.2}O_2$ and $LiNi_{0.5}Mn_{0.5}O_2$. Results for Precursor #14 heated with lithium hydroxide monohydrate at 725°C and 775°C were not reported in those two chapters.

The lithiation process was the same as previous chapters. The lithiation temperatures for Group I and II materials are 700°C, 725°C, 750°C, 800°C for 10 hours in oxygen. The lithiation temperatures for Group III materials are 700°C, 750°C, 800°C for 10 hours in oxygen. The lithiation temperature for Group IV materials are 650°C, 725°C (#14 only), 700°C, 750°C, 775°C (#14 only), 800°C for 20 hours in oxygen.

The lithiated materials were given names based on their corresponding precursors, for example, C98_S80_16/1 is the lithiated material made from precursor #1 that has a core composition of $Ni_{0.98}Mn_{0.02}(OH)_2$, shell composition $Ni_{0.8}Mn_{0.2}(OH)_2$, 16 μm core diameter and 1 μm shell thickness. The SEM images of precursors #1 to #11 are shown in Figure B.1.

Table 6.1 List of all core-shell precursors

Precursor #	Ni Composition in Core - Shell [%]	Core Diameter - Shell Thickness [μm]	Average Ni Content [%]	Reference Name
Group I # 1	98 - 80	16 - 1	91.7	C98_S80_16/1
Group I # 2	98 - 80	12 - 0.75	91.8	C98_S80_12/0.75
Group I # 3	98 - 80	8 - 0.75	90.7	C98_S80_8/0.75
Group I # 4	98 - 80	8 - 0.5	92.4	C98_S80_8/0.5
Group II # 5	100 - 85	16 - 1	93.8	C100_S85_16/1
Group II # 6	100 - 85	12 - 0.75	95.6	C100_S85_12/0.75
Group II # 7	100 - 80	12 - 0.75	93.6	C100_S80_12/0.75
Group III # 8	100 - 85	8 - 0.75	94.6	C100_S85_8/0.75
Group III # 9	100 - 80	8 - 0.75	91.8	C100_S80_8/0.75
Group III # 10	100 - 85	8 - 0.5	95.4	C100_S85_8/0.5
Group III # 11	100 - 80	8 - 0.5	93.8	C100_S80_8/0.5
Group IV # 12	100 - 50	17 - 0.5	91.7	C100_S50_17/0.5
Group IV # 13	100 - 80	17 - 0.5	97.2	C100_S80_17/0.5
Group IV # 14	100 - 80	16 - 1	93.5	C100_S80_16/1

6.3 Results and Discussion

6.3.1 XRD and Refinement Results

Figure 6.1 shows the **average** lattice constants a, c and percentage of Ni in the Li layer, Ni_{Li}, for samples in Groups I to III from the Rietveld-refined XRD patterns. The XRD patterns of samples in Groups I to III at 700ºC, 750ºC and 800ºC are shown in Figure B.2 in Appendix B. Separate core and shell phases could not be distinguished by XRD due to the similarity of the lattice constants of the core and shell phases. The XRD patterns show no observable impurity peaks between 20 and 35º as shown in Figure B.2 and no impurity peaks elsewhere. An increased (108)/(110) Bragg peak splitting (near 65º) at

higher heating temperature indicates increased material crystallinity. The lattice constant, *a*, shows a weak function on heating temperature for all sample groups, whereas the lattice constant, *c*, and Ni_{Li} show a much stronger dependence on temperature. Higher heating temperature helps reduce the amount of undesirable nickel atoms in the Li layer giving higher specific capacity.

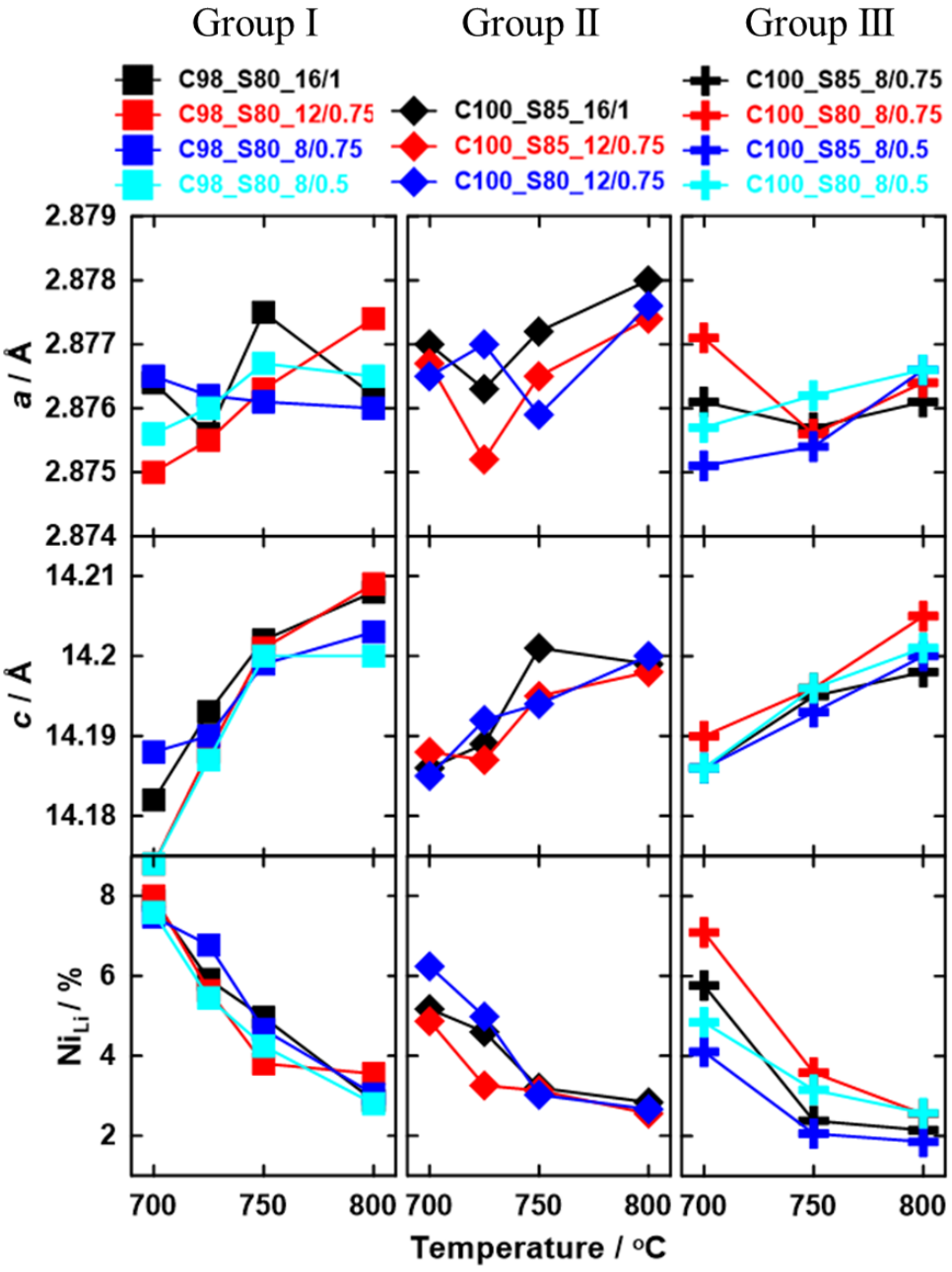

Figure 6.1 Impact of heating temperature on lattice constants and percentage of Ni in Li layer, Ni_{Li}.

6.3.2 Irreversible Capacity and Voltage Polarization as a Function of Cation mixing

Figure 6.2 shows the 1st cycle irreversible specific capacity (IRC) and voltage polarization between 2nd charge and 1st discharge (ΔV) measured at C/20 and at 30ºC as a function of Ni_{Li} for Groups I to III. For all three groups, a low value of Ni_{Li}, resulting from a high heating temperature, yields low IRC and ΔV, therefore high reversible specific capacity.

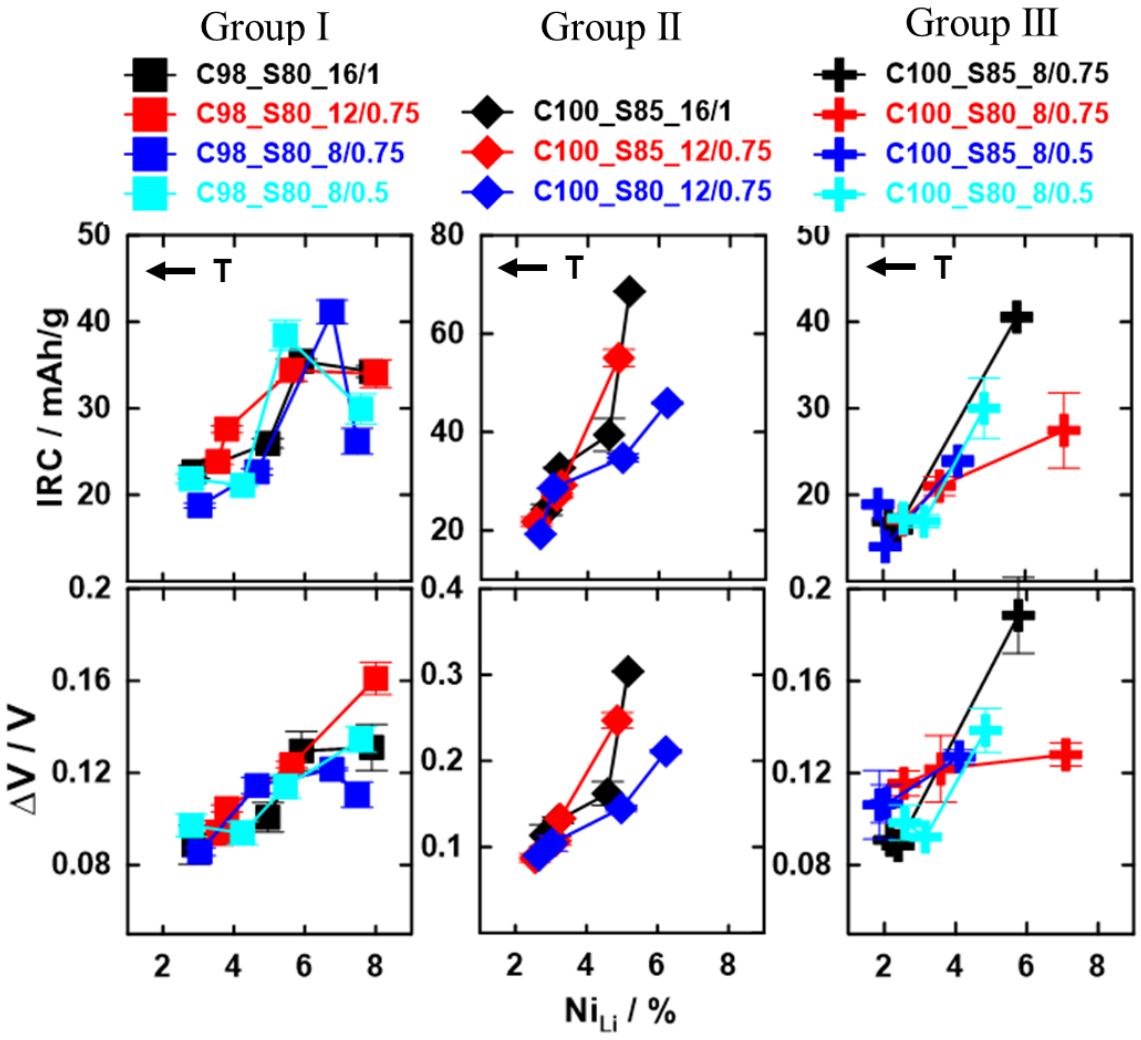

Figure 6.2 Impact of Ni_{Li} on the 1st cycle irreversible capacity, IRC, and voltage polarization, ΔV, between the 2nd charge and 1st discharge. The arrows show the direction of increased heating temperature.

6.3.3 Core-shell Structure Verification

Figure 6.3(a) shows the initial C/20 dQ/dV vs. V for materials in Groups I to III synthesized at several temperatures. Specific capacity data for all materials in Groups I to III are shown in Table B.1 to Table B.11 in Appendix B. Heating to higher temperatures increases the specific capacity of all the materials considered here. This is also shown by the increased area of the dQ/dV vs V graphs. The specific capacity increase agrees with the discussion surrounding Figure 6.1 and Figure 6.2 where the high heating temperature increases the material crystallinity and reduces Ni_{Li}.

The most prominent changes in the features present in the dQ/dV vs V curves occur at ca. 4.2 V vs. Li/Li^+. The dQ/dV peaks at this voltage are remnants of the H2/H3 phase transition which exists in $LiNiO_2$.[61] These peaks keep increasing in intensity (sharpness) as the heating temperature increases. In this region, the unit cell volume changes dramatically, therefore it is believed that long term cycling over this region can cause particle cracking for polycrystalline materials.[71,80]

The red enclosed dQ/dV vs V plots in Figure 6.3(a) are from materials that failed to maintain their core-shell structures due to Mn interdiffusion at 800ºC heating temperatures for 10 hours. These materials are expected to have poor cycling performance and severe particle cracking with an upper cut-off set at 4.3 V vs. Li/Li^+. EDS Mn line scans of the core-shell samples from Groups I to III at 750ºC and 800ºC are shown in Figure 6.3(b). Among the materials in Group I, the C98_S80_8/0.5 at 800ºC failed to maintain its core-shell structure due to having the thinnest shell in the group. Comparing the line scan of C98_S80_12/0.75 to the smaller C98_S80_8/0.75 particles, it is apparently easier for a smaller core size to maintain a core-shell structure at high heating temperature. This could be due to the larger surface area of the C98_S80_12/0.75 particles compared to the C98_S80_8/0.75 particles which allows more Mn interdiffusion per unit time. At 800ºC, the C100_S80_12/0.75 sample in Group II still has a core-shell structure whereas C100_S85_12/0.75 with less Mn in the shell became homogenous. This implies it is necessary to have a relatively high Mn content in the shell if heating at 800ºC is desired. For Group III materials, the C100_S80_8/0.75 sample has the thickest

shell with the highest Mn content and it still became almost homogenous at 800ºC, therefore other materials with thinner shells or shells with less Mn will not be able to maintain the core-shell structure. This matches the observations in EDS Mn line scans.

Comparing C98_S80_8/0.75 of Group I to C100_S80_8/0.75 of Group III at 800ºC, it seems that more Mn in the core helps maintain the core shell structure as the Mn diffusion was slightly reduced due to lower concentration gradient. Therefore, C98_S90_8/0.75 is still a core shell material at 800ºC but C100_S80_8/0.75 at 800ºC is not. However, comparing C98_S80_12/0.75 of Group I to C100_S80_12/0.75 of Group II contradicts this observation, but it is possible the larger core surface area plays a role here.

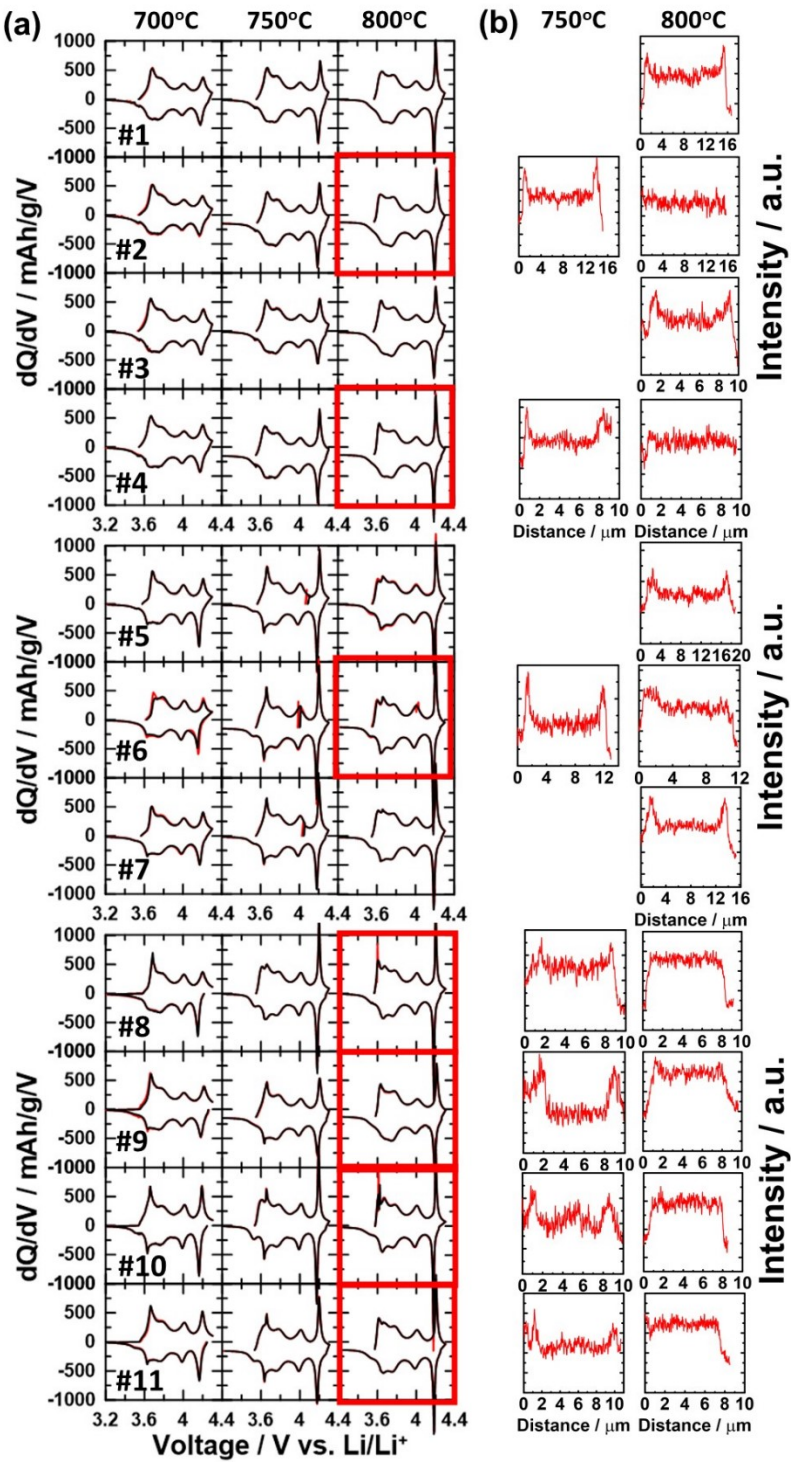

Figure 6.3 (a) The C/20 dQ/dV vs. V evolution as a function of heating temperature of Group I (top) to Group III (bottom). Plots are numbered by their corresponding precursors as in Table 6.1. (b) The absence or presence of core-shell structures at 750°C and 800°C as verified by Mn EDS line scans from cross-sections of particles in fresh electrodes.

6.3.4 Capacity Retention as a Function of Specific Capacity, Li Utilization, Crystallinity and Cation Mixing

Figure 6.4 shows the fractional capacity after 50 charge-discharge cycles measured from 3 to 4.3 V vs. Li/Li^+ at 30ºC and C/5 versus the 1st C/20 discharge specific capacity (top panels) and Li utilization (bottom panels) of the materials in Groups I to IV on top of the historic half cell data shown in grey. All the historic data consists of both published and unpublished Co-free half cell data that was measured under the same condition in Dahn group before 2020.[63] The historic data shows a very "depressing" trend that excellent capacity retention and high specific capacity for Ni-rich layered materials cannot be achieved at the same time. The main purpose of these plots is to examine if any core-shell material is able to overcome the challenge of layered Ni-rich materials. In other words, can any material reach the upper-right corner of these plots? A commercial single crystal $LiNi_{0.8}Mn_{0.1}Co_{0.1}O_2$ (SC811) data point is included here for benchmarking. Digitized literature data for two Co-free materials from two research groups are also included here for comparison.[47,54] These groups adopted a different strategy to solve the challenges of Ni-rich materials through doping $LiNiO_2$ with other elements. Please note that the testing conditions for these literature data are not the same as in this study. The specific capacities from the literature were both measured at C/10 and these would have been a bit higher by ca. 5 mAh/g, if measured at C/20. The fractional capacities versus cycle number were measured at C/3 to 4.4 V vs. Li/Li^+ at 25ºC for W. Li et al.[54] and at C/2 to 4.3 V vs. Li/Li^+ at 30ºC for Aishova et al.[47]

The materials in Group I and Group II mostly follow the historic data. All Group I and II materials follow the same trend of typical Ni-rich layered materials where higher heating temperature brings higher specific capacity but at the same time lowers the capacity retention. Among these materials, C98_S80_12/0.75, C98_S80_8/0.5 and C100_S85_12/0.75 at 800ºC are homogenous due to Mn interdiffusion which are equivalent to $LiNi_{0.918}Mn_{0.082}O_2$, $LiNi_{0.924}Mn_{0.076}O_2$ and $LiNi_{0.956}Mn_{0.044}O_2$, respectively. At 800ºC, the core shell materials have superior capacity retention to those that become homogenous.

Among the Group III and IV materials, C100_S85_8/0.5 at 700ºC and 750ºC, and C100_S80_16/1 at 750ºC, located towards the upper-right corner of the graphs, outperformed other materials within their groups as they simultaneously showed high specific capacity and good capacity retention. These three materials all have well-defined core-shell structures. Comparing their counterparts at 800ºC which are homogenous materials, the differences in their capacity retention are significant.

The trend in capacity retention vs. and Li utilization mirrors that of the capacity retention vs. specific capacity as high Li utilization leads to high specific capacity. Figure B.3 shows specific capacity, fractional capacity and normalized voltage polarization (ΔV_3) as a function of cycle number for Group I (a) to III (c) materials, respectively, at 700ºC, 750ºC and 800ºC up to 106 cycles. Figure B.4 compares the C/20 dQ/dV vs V plot of 2nd cycle to that of the 105th cycle. Materials without the core-shell structure show more severe changes in their dQ/dV peaks at ca. 4.2 V. vs. Li/Li$^+$ which could be related to particle cracking.[98]

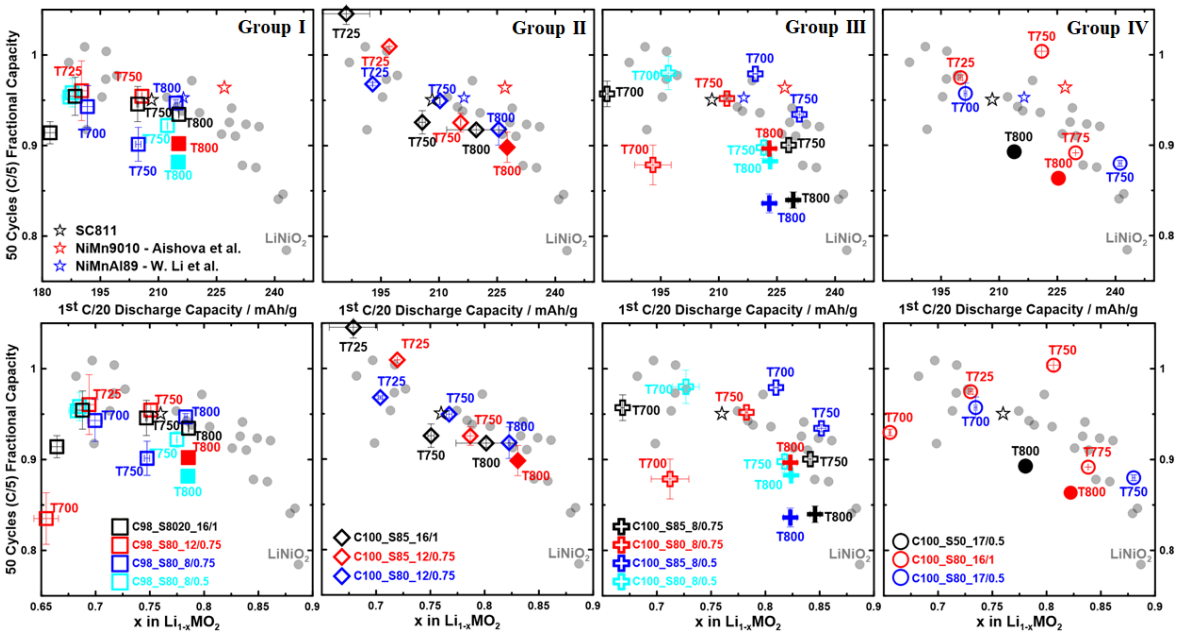

Figure 6.4 Fractional capacity vs. specific capacity (top panels) and Li utilization (bottom panels) of Group I to Group IV. All data points were measured at 30°C with upper cut-off 4.3 V vs. Li/Li^+. The 1st C/5 discharge capacity was taken as 100%. Data points from literature were digitized from references [47] and [54] where the discharge capacities were both measured at C/10. The heating temperatures are labeled. Hollow symbols denote core-shell materials. Solid symbols denote homogenous samples due to Mn interdiffusion.

Figure 6.5 shows the fractional capacity after 50 cycles measured from 3 to 4.3 V vs. Li/Li^+ at 30°C and C/5 as a function of the full width half max (FWHM) of (108) Bragg peak and the percentage of Ni in the Li layer (Ni_{Li}). Both independent variables are also functions of heating temperature as shown in Figure 6.1 and Figure 6.2. Group I, II and IV materials show an obvious trend that though high heating temperature gives high crystallinity and low Ni_{Li}, the materials risk losing the core-shell structure due to Mn interdiffusion, and when that occurs, the materials show an inferior capacity retention. In contrast, low heating temperature helps maintain the core-shell structure but at the cost of having low crystallinity and high Ni_{Li} therefore low specific capacity. Optimized heating temperature, shell thickness and Mn content in both the core and shell are required to have both satisfactory specific capacity and capacity retention.

For the C98_S80_12/0.75 and 8/0.5 series in Group I, although their crystallinity is increased and Ni_{Li} is lowered from 750 to 800°C which increases specific capacity, their capacity retention shows a large decrease due to the vanishing Mn-containing shell. On the other hand, the C98_S80_16/1 and 8/0.75 that can withstand heating to 800°C and maintain their core-shell structures show a relatively high crystallinity and low Ni_{Li} without compromising capacity retention. For all Group II materials, the highest fractional capacity after 50 cycles occurs at 725°C with intermediate crystallinity and Ni_{Li}. For Group III materials, the highest fractional capacity remaining after 50 cycles likely also occurs at around 725°C for which experiments were not conducted. For Group IV materials, the best performing material is the C100_S80_16/1 at 750°C which is also an intermediate heating temperature.

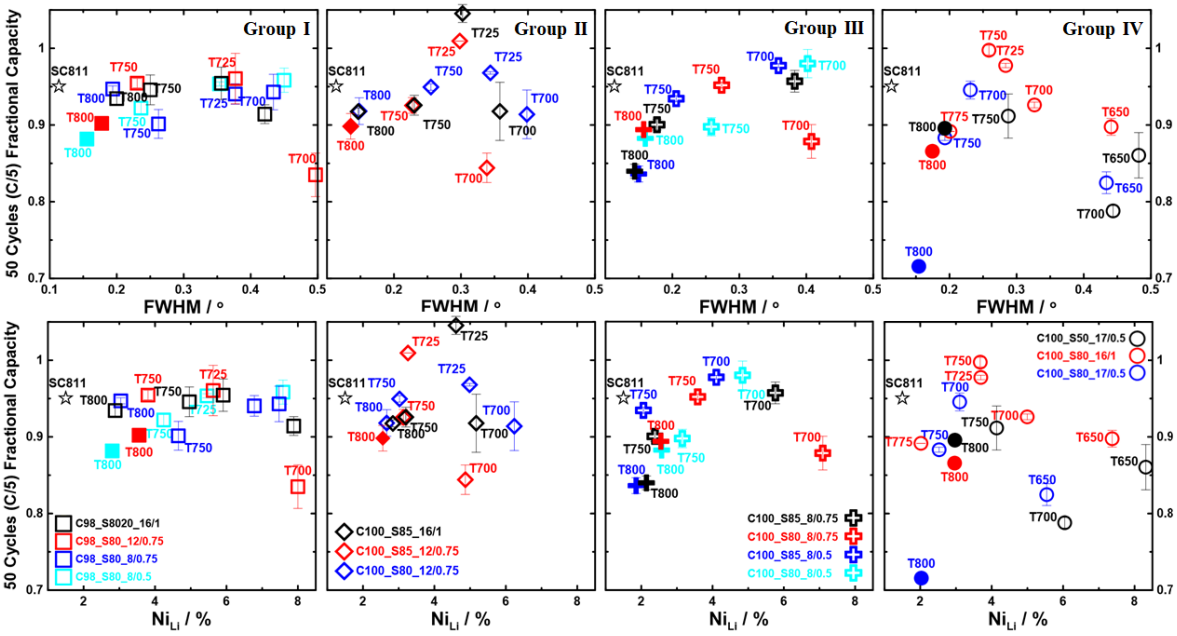

Figure 6.5 Fractional capacity vs. full width half max (FWHM) of (108) Bragg peak (top panels) and percentage of Ni in Li layer (Ni_{Li}) (bottom panels) of Group I to Group IV. All data points were measured at 30°C with and upper cut-off 4.3 V vs. Li/Li^+. The 1st C/5 discharge capacity was taken as 100%. The heating temperatures are labeled. Hollow symbols denote core-shell materials. Solid symbols denote homogenous samples due to Mn interdiffusion.

6.3.5 Degradation Analysis

Figure 6.6(a) shows the post-cycling cross-section SEM images of four materials heated at either 750ºC (T750) or 800ºC (T800). Among them, T800_C100_S80_8/0.75 and T800_C100_S85_8/0.75 are not core-shell materials due to Mn interdiffusion at 800ºC as shown previously, whereas T750_C100_S85_8/0.5 and T750_C100_S80_16/1 are core-shell materials. Both materials heated at 800ºC suffer from severe particle cracking which can explain their poor capacity retentions and high voltage polarization increase in Figure 6.6(b). In contrast, T750_C100_S85_8/0.5 has shown few observable microcracks which is one of the reasons that it shows good capacity retention. Surprisingly, T750_C100_S80_16/1 which has even better capacity retention than T750_C100_S85_8/0.5 shows obvious particle cracking. However, upon a closer look at the particle periphery, these cracks hardly extend beyond the core. Because of this, the shell may still prevent electrolyte from going into the particle interior. J. Li et al.,[165] via *in-situ* XRD, showed the core-shell structure with Ni-rich core and Mn-rich shell should be very stable upon cycling as a result of a lower degree of unit cell contraction and expansion of the shell material compared to a Ni-rich core, therefore microcracking is only observed for the core.

Since the capacity degradations for both T750_C100_S85_8/0.5 and T750_C100_S80_16/1 are unlikely due to microcracking, it is speculated that the difference in specific surface areas as a result of difference particle size may play an important role here. A core-shell particle with 8 μm diameter core and 0.5 μm thick shell has a surface area around 0.25 m^2/g shown in Table 6.2. A much larger core-shell particle with 16 μm diameter core and 1 μm thick shell has a surface area of 0.13 m^2/g larger specific surface area of small particle size could cause more side reactions with electrolyte during long-term charge/discharge cycling than the much larger particles with smaller specific surface area. This explains the faster voltage polarization increase of T750_C100_S85_8/0.5 than that of T750_C100_S80_16/1.

Figure 6.6(c) shows the EDS Mn mapping/line scans after 106 cycles at 4.3 V vs. Li/Li^+ for T750_C100_S85_8/0.5 and T750_C100_S80_16/1. Both materials have maintained the core-shell structures after charge/discharge cycling.

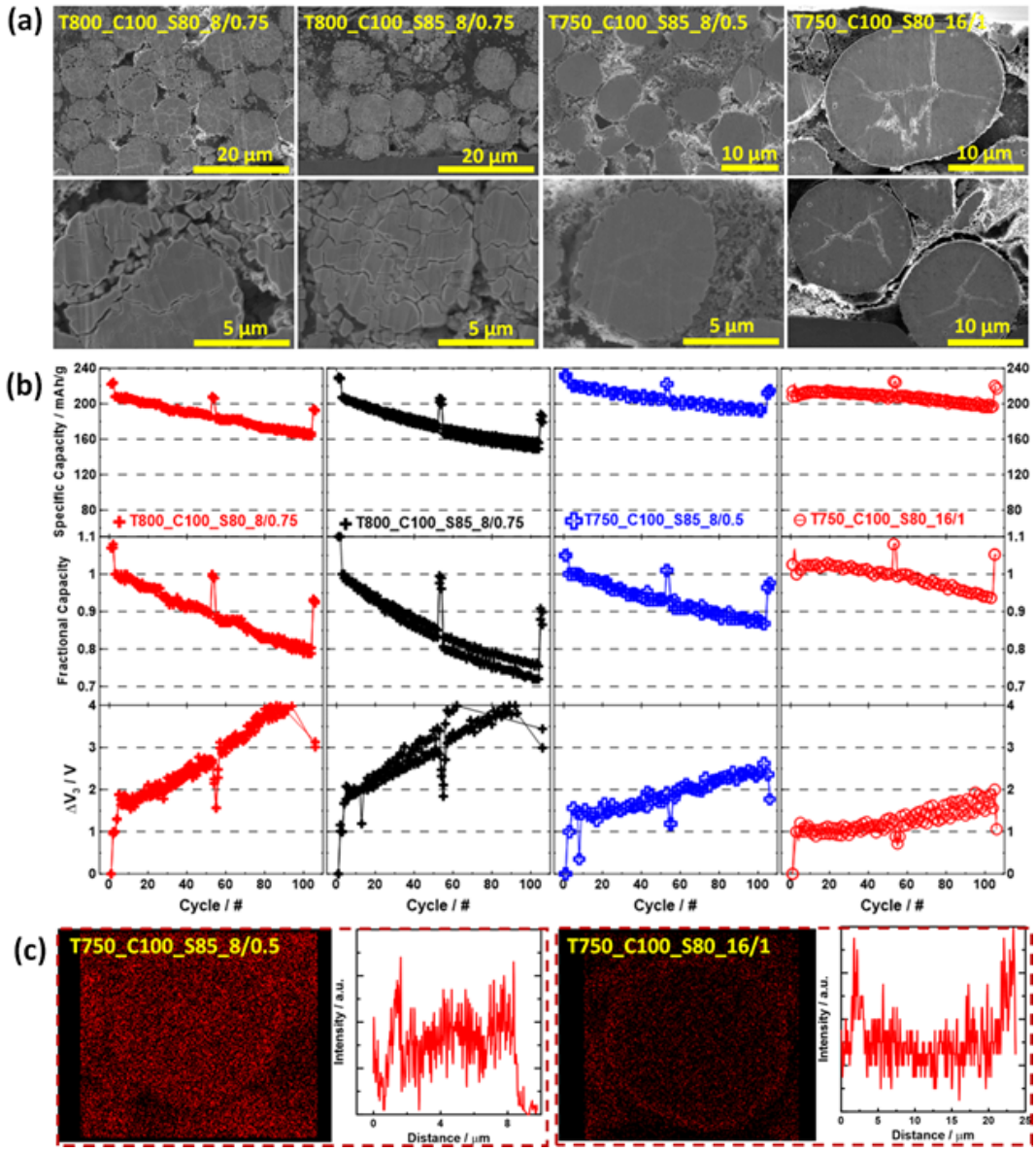

Figure 6.6 (a) Cross-section SEM images after 106 cycles at 30°C to 4.3 V vs. Li/Li^+. These electrodes were retrieved at 4.3 V vs. Li/Li^+. (b) The specific capacity, fractional capacity and normalized voltage polarization (ΔV_3). The materials were tested at 30°C to 4.3 V vs. Li/Li^+. The 1st C/5 discharge (3rd discharge) is taken as 100% in the fractional capacity plots. The ΔV of the 1st C/5 cycle (3rd cycle) is taken as 100%. (c) The EDS Mn mapping/line scans at 4.3 V vs. Li/Li^+ after 106 cycles.

6.3.6 Safety Comparison

Figure 6.7 examines the safety performance of some selected materials by accelerating rate calorimetry (ARC). This is to explore how the safety performance of Co-free core-shell material is influenced by parameters such as heating temperature, core size, shell thickness, and Mn content in the core and shell. Table 6.2 shows the BET specific surface areas of these materials showing they are all less than 0.26 m^2/g and within a factor of two of that value. The ARC result therefore reflects the intrinsic reactivity difference across different materials. Figure 6.7(a) compares the C100_S80_8/0.75 samples heated to 700, 750 and 800°C to $LiNiO_2$ which is well-known for its poor safety performance. As the heating temperature gets higher, the Mn-containing shell gets thinner due to Mn interdiffusion. As a result, the ARC result shows high reactivity with electrolyte when the core-shell samples are heated to high temperature due to the thinner or non-existent shell. Figure 6.7(b) compares the influence of core size on reactivity with electrolyte for core-shell samples prepared at 750°C. All three materials maintained the core-shell structure when prepared at this temperature and showed no thermal-runaway in the ARC experiments. This shows that for core-shell materials, the core size does not affect the reactivity with electrolyte at elevated temperature in a significant way. Figure 6.7(c) shows the influence of shell thickness on reactivity with electrolyte for samples prepared at 750°C. All three materials have core-shell structures when prepared at this temperature. The samples with a shell thickness of 0.75 μm and 1 μm did not go to thermal-runaway in the ARC experiments. However, when the shell thickness was reduced to 0.5 μm, thermal-runaway occurred in one of two trials. Figure 6.7(d) compares the effect of Mn content on samples with the same core size and shell thickness when prepared at 750°C. Slightly lowering the Mn content in the core by 2% does not impact the reactivity with electrolyte at elevated temperature. When the Mn content in the shell is low, the reactivity of the material with electrolyte is increased. In general, for a core-shell material to have low reactivity with electrolyte at elevated temperature, it needs to have a thick and relatively high Mn-content shell. Based on this conclusion, though the C100_S85_8/0.5 at 750°C shows excellent specific capacity and capacity retention, its safety performance in Li-ion cells would most likely be poor due to its relatively low Mn content in the thin shell.

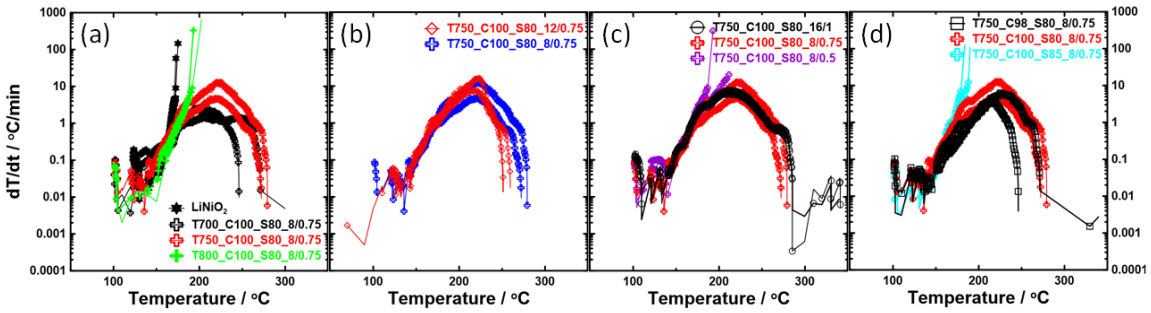

Figure 6.7 Self-heating rate, dT/dt, versus temperature during ARC studies on charged core-shell materials (4.3 V vs. Li/Li^+) and electrolyte. The ARC samples were forced to 100°C at the start of each experiment. Duplicate experiments were made for each sample. The reactivity of the samples has been examined as a function of (a) synthesis temperature (b) core size (c) shell thickness (d) core and shell composition. Hollow symbols denote core-shell materials. Solid symbols denote homogenous samples.

Table 6.2 Specific surface areas of materials used in ARC experiments

Precursor	C98_S80_8/0.75	C100_S80_8/0.75			C100_S85_8/0.75	C100_S80_8/0.5	C100_S80_12/0.75	C100_S80_16/1
Temperature [°C]	750	700	750	800	750	750	750	750
Surface area [m^2/g]	0.15	0.26	0.17	0.22	0.17	0.25	0.16	0.13

6.4 Conclusions

This chapter systematically studied the electrochemical and safety performance of a variety of Co-free core-shell materials with different core size, shell thickness, core and shell compositions synthesized at various temperatures. Among all the materials, C100_S85_8/0.5 at 700°C/750°C of Group III and C100_S80_16/1 at 750°C of Group IV standout towards the upper-right corner of the capacity retention vs. specific capacity plots shown in Figure 6.4. For core-shell materials to have satisfactory performance in both metrics, the heating temperature of the precursor/$LiOH•H_2O$ mixture must be carefully selected. Core shell materials made at too low heating temperature will have low specific capacity resulting from low crystallinity and high Ni_{Li}, whereas if the heating temperature is too high, capacity retention and safety performance will decrease

due to the diminished Mn-containing shell. Core shell materials with thick and relatively high Mn-content shells have shown low reactivity with electrolyte at elevated temperature. Figure 6.8 schematically summaries the above observation. In this regard, C100_S85_8/0.5 at 700ºC from Group III and C100_S80_16/1 at 750ºC from Group IV have shown the good performance in all of safety, specific capacity, and capacity retention performance.

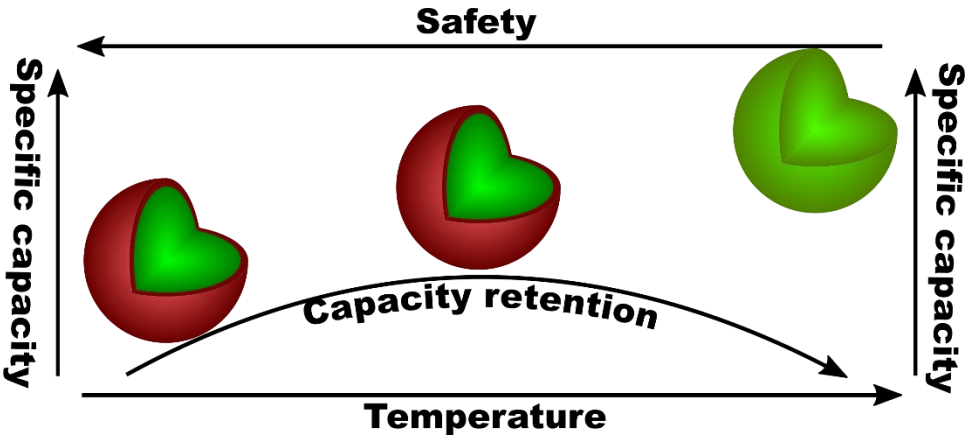

Figure 6.8 A schematic shows the importance of optimized lithiation temperature on material performance.

The author acknowledges that mass producing such materials may be challenging in part due to the sensitivity of the core-shell microstructure to the heating temperature. There is a temperature window of only about 25 to 50ºC in which optimum materials can be produced as shown by heating C100_S80_16/1 precursor in Figure 6.4 Group IV. Because of this, it may be difficult to achieve an optimum material when scaling-up with a large tunnel kiln, for example. If the temperature is too low, there is poor crystallinity and too much Ni in the Li layer. If the temperature is too high, the core-shell structure, and all its benefits, disappears due to Mn interdiffusion. Various types of core-shell and gradient core-shell materials have been proposed in the literature by several research groups.[86,145,171–173] We believe that mass production of such materials will face similar challenges for the same reasons.

Chapter 7 A Physical and Electrochemical Comparison of the Washed and Unwashed Core-shell Materials

7.1 Introduction

Slurry gelation caused by surface lithium residues on positive electrode materials makes it impossible to produce good electrode coatings. Therefore, removing surface lithium residues by a washing step is commonly applied. However, this washing step can potentially impact the physical and electrochemical performance of the material. In this chapter, unwashed Co-free Ni-rich core-shell material could be uniformly coated on aluminium foil when 0.7 wt.% of oxalic acid was added to the slurry formulation to neutralize the basic lithium residues. In this way, pouch cells with the unwashed core-shell material could be made and their performance can be compared to those made with washed core-shell materials. Besides the electrochemical performance, physical performance of the washed and unwashed core-shell material is also compared in this chapter.

7.2 Experimental

Both the washed and unwashed polycrystalline Co-free core-shell materials have an average composition of $LiNi_{0.94}Mn_{0.06}O_2$ provided by reputable vendor. The materials were made from a precursor that has 16 μm $Ni(OH)_2$ core and 1 μm thick $Ni_{0.8}Mn_{0.2}(OH)_2$ shell. The precursor was reacted with $LiOH{\bullet}H_2O$ at a temperature between 700 and 750ºC in oxygen flow. This is the core-shell composition demonstrated good performance from Chapter 4 to Chapter 6. The core-shell materials were not coated and were obtained from a reputable company. The material obtained right after the lithiation process is called the “unwashed” material. The washing/reheating process was carried out on the “unwashed” material to obtain the “washed” material. The detailed washing/reheating process was not revealed to the author.

The physical characterization methods of powder crush test, XRD and refinement, SEM/EDS have been shown in Chapter 3.

Both the washed and unwashed core-shell pouch cells were formed at 40ºC followed by the protocol in Chapter 3, except those with (methyl acetate) MA were formed the same way but with a 4.2 V upper voltage cut-off.

The electrolyte blends used in each pouch cell were based on our previous experience on the cells made with $LiNi_{0.5}Mn_{0.3}Co_{0.2}O_2$ (SC532) and $LiNi_{0.8}Mn_{0.1}Co_{0.1}O_2$ (SC811) positive electrodes.[45,159] and were discussed in Chapter 2. All electrolytes used were 1.5 M $LiPF_6$ salt from either BASF or Shenzen Capchem. The solvent blend without MA used in this chapter was ethylene carbonate (EC): ethyl methyl carbonate (EMC): dimethyl carbonate (DMC) 25:5:75 by volume. A control electrolyte is a blend of solvent and $LiPF_6$ salt only.

Electrolyte additives were added to the control electrolyte with respect to the total electrolyte weight:

1. 2% VC (vinylene carbonate) and 1% DTD (ethylene sulfate), abbreviated as 2VC1DTD, promoted by J. Li et al.,[43]
2. 2% FEC (fluoroethylene carbonate) and 1% LFO ($LiPO_2F_2$ - lithium difluorophosphate), abbreviated as 2FEC1LFO, promoted by L. Ma et al.,[120]
3. 1% LFO, abbreviated as 1LFO, promoted by L. Ma et al.,[119]
4. 1% LFO and 1% ODTO (1,2,6 – Oxadithiane 2,2,6,6 – tetraoxide), abbreviated as 1LFO1ODTO, promoted by X. Ma et al.[118]

The solvent blend with MA was used together with 2FEC1LFO additives in unwashed core-shell pouch cells only. MA was added to the EC/EMC/DMC solvent by volume to improve ionic conductivity[35]:

1. 90% EC:EMC:DMC + 10% MA, abbreviated as 10MA,
2. 80% EC:EMC:DMC + 20% MA, abbreviated as 20MA,
3. 70% EC:EMC:DMC + 30% MA, abbreviated as 30MA,

7.3 Results and Discussion

7.3.1 Physical Characterization Comparison

Figure 7.1(a) shows the SEM images of the washed and unwashed core-shell materials. For the washed material, there are no observable lithium residues on particle surfaces, whereas several lithium residue-covered particles can be easily found in the SEM image of unwashed core-shell material, as indicated by the yellow arrows. The high magnification SEM images of the unwashed material shows well-defined primary particles. In contrast, the washed particle surface seems to be "smoothed" which makes it difficult to determine the primary particle size from the SEM images.

Figure 7.1(b) shows the Rietveld-refined powder XRD patterns of the washed and unwashed materials. Both XRD patterns are virtually identical. No Li_2CO_3 impurity was detected by XRD within the 20° to 35° scattering angle range, even for the unwashed material. This suggests that XRD is not sensitive enough to detect the small amounts of lithium impurities in this sample. The XRD refinement was conducted assuming an average core-shell composition $LiNi_{0.94}Mn_{0.06}O_2$ and the refinement results are listed in Table 7.1. The washed material shows a higher percentage of Ni in the Li layer, Ni_{Li}%.

Figure 7.1(c) verifies the core-shell structure of the washed and unwashed materials with a Mn EDS mapping/line scan. After material washing/reheating, the core-shell structure was still maintained. Figure 7.1(d) shows the SEM images of the material powders that underwent the crushing test at 700 MPa. The unwashed material is more mechanically robust than the washed material. After crushing, many washed core-shell particles crumbled into small pieces, but the unwashed particles largely retained their spherical shape. The single crystal $LiNi_{0.8}Mn_{0.1}Co_{0.1}O_2$ (SC811) particles have outstanding mechanical strength and hence the crushing test has virtually no effect on the single crystal particles.

Figure 7.1(e) shows the cross-sectional SEM images of the fresh electrodes from pouch cells. Both the washed and unwashed core-shell positive electrodes show particle cracking from electrode calendering. The microcracks due to calendering are particularly

detrimental for the Ni-rich core as a direct exposure to the electrolyte is expected to cause severe side reactions during cycling. It was shown previously that the SC811 fresh electrodes have minimal microcracking from calendering,[80] which highlights the advantageous processing ability of single crystal materials compared to the polycrystalline ones. The cross-sectional SEM images of the artificial graphite negative electrode used in pouch cells are also shown.

Figure 7.1(f) shows the front and back images of the unwashed core-shell electrode from a dry (no electrolyte) pouch cell where 0.7 wt.% of oxalic acid was added to the slurry formulation. The unwashed core-shell positive electrode shows a uniform coating texture without any observable defects.

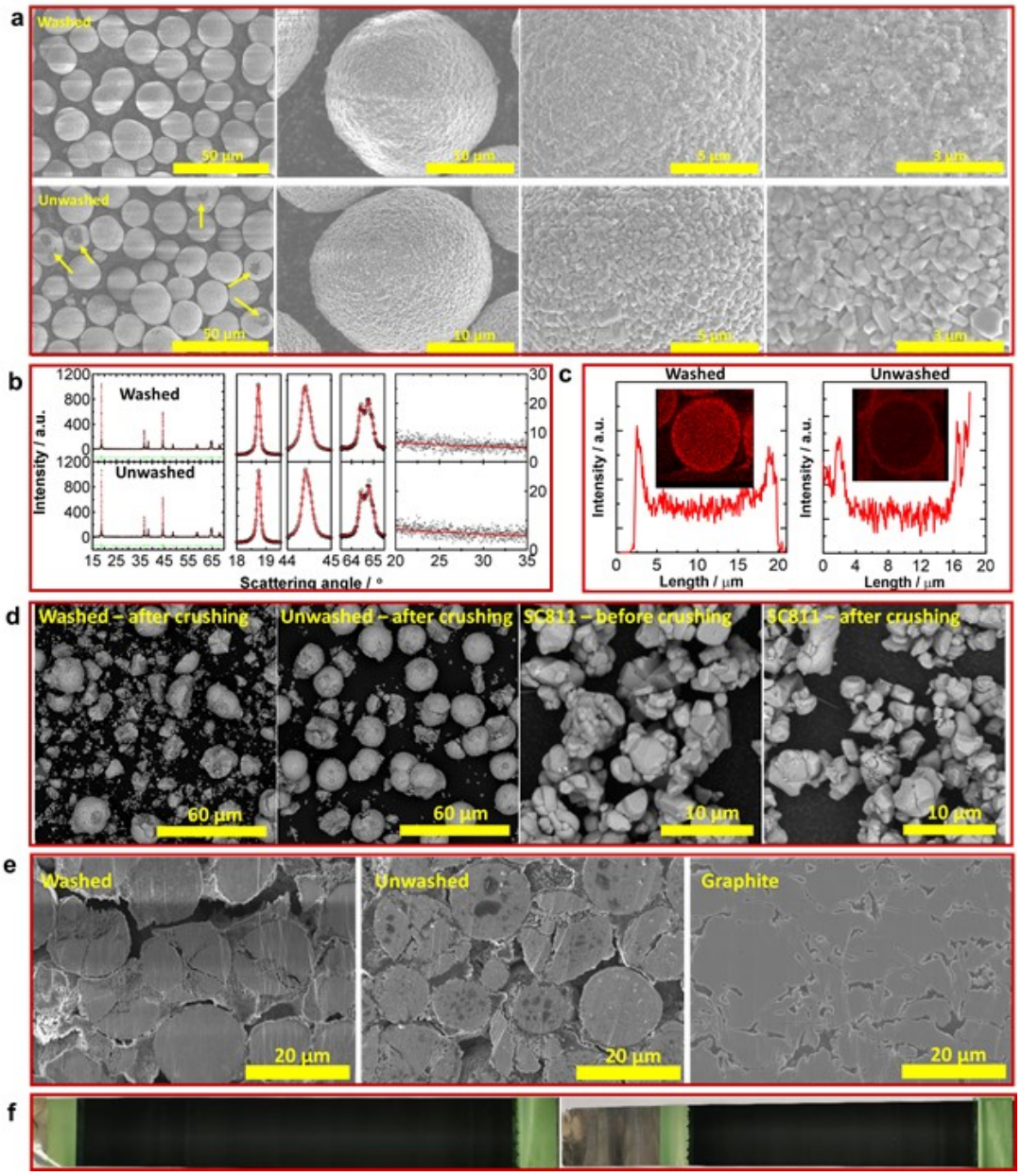

Figure 7.1(a) SEM images of the washed and unwashed core-shell materials. The arrows point to the particles with surface lithium residues. (b) Rietveld-refined powder XRD patterns of the washed and unwashed core-shell materials. The refinement results are shown in Table 7.1. (c) Cross-sectional Mn mappings/line scans of washed and unwashed core-shell particles. (d) SEM images of the crushed washed/unwashed core-shell particles, and the SEM images of the SC811 before/after crushing. (e) The cross-sectional SEM images of fresh washed and unwashed core-shell positive electrodes, and fresh artificial graphite negative electrode. (f) The front and back images of the unwashed core-shell positive electrode from a fresh pouch cell using 0.7 wt.% oxalic acid in the slurry formulation.

Table 7.1 Rietveld-refinement result of the washed and unwashed core-shell materials

Core-shell material	a / Å	c / Å	Oxygen position, *z*	*Ni_{Li} / %	Bragg R
Washed	2.87690(8)	14.199(8)	0.2420(2)	2.993	1.29
Unwashed	2.87650(8)	14.200(8)	0.2418(2)	2.559	1.26

*Ni_{Li} – percent of Ni atoms in the Li layer.

7.3.2 Coin Half Cell Performance Comparison

Figure 7.2(a) compares the half cell cycling performance of the washed and unwashed core-shell materials with 4.25 and 4.1 V upper cut-off voltage (UCV) vs. Li/Li^+, which corresponds to 4.18 and 4.04 V when cycled in pouch cells. When cycled up to 4.25 V vs. Li/Li^+, the unwashed material performs better than the washed material with 1.2 M $LiPF_6$ in FEC/DMC electrolyte in terms of normalized capacity and voltage polarization, but their cycling performances are quite similar when cycled to up to 4.1 V vs. Li/Li^+. This implies the washing/reheating process mainly influences the material performance at high voltage. When cells are cycled with a MA-containing electrolyte with 2FEC1LFO additives, the capacity retention and voltage polarization of the unwashed core-shell electrode performance can be further improved with 4.25 V UCV.

Figure 7.2(b) compares the C/20 dQ/dV vs. V plots before and after 50 cycles of C/5 cycling. After 50 cycles, the washed material shows a decreased intensity of the 4.2 dQ/dV peak, whereas the 4.2 V dQ/dV peak remains stable for the unwashed material, regardless of the electrolyte used. This dQ/dV peak is the "remnant" of the "H2-H3 phase transition" of Li_xNiO_2 that occurs between 4.1 V and 4.25 V vs. Li/Li^+. When charging over this region, the lattice volume decreases significantly causing particle microcracking that induces more side reactions between the Ni-rich core and the electrolyte.[63] The 4.1 V UCV cycling excludes this "H2-H3 remnant" region which is believed to be the main reason for its better capacity retention than cycling with 4.25 V UCV shown in (a). The very stable dQ/dV plots in the 4.1 V UCV case for both the washed and unwashed materials suggest the washing/reheating process impacts mostly the "H2-H3 remnant" of the core-shell material. It was shown in Figure 7.1(e) that the unwashed material was more mechanically robust in the crushing test. Recent work by Hamam et al.[174] has

shown that high Ni materials with better capacity retention are more mechanically robust, which could explain the better performance of the unwashed core-shell material compared to its washed version, even when cycling over the "H2-H3 remnant" region.

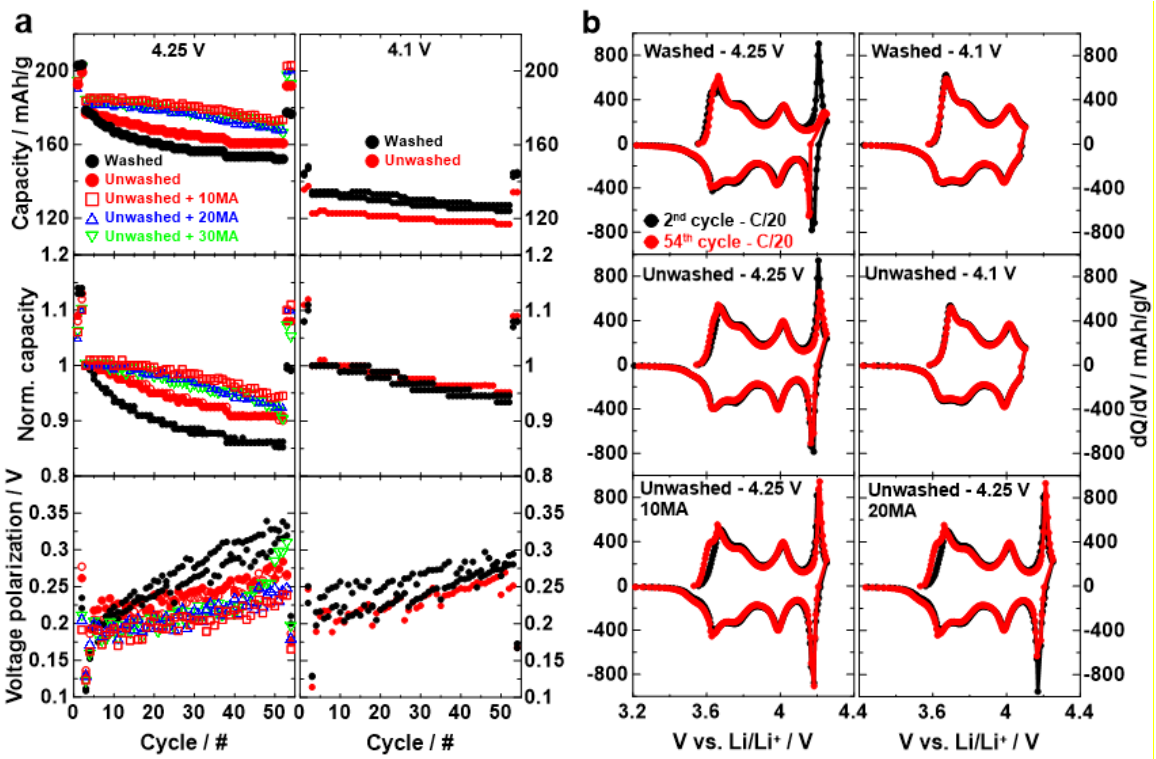

Figure 7.2(a) Capacity, normalized capacity and voltage polarization of the washed and unwashed core-shell positive electrodes tested in coin cells. Electrodes were punched from the single-side-coated part of the positive electrodes in fresh (no electrolyte) pouch cells. Electrodes were tested at 30°C from 3.0 to either 4.1 or 4.25 V vs. Li/Li^+. The electrolyte blends are indicated in the Experimental section. (b) C/20 dQ/dV vs. V plots before and after 50 cycles of the washed and unwashed core-shell positive electrodes.

7.3.3 Pouch Cell Performance Comparison

Figure 7.3(a) shows the gas generation during formation, 1st cycle efficiency and charge-transfer resistance R_{ct} measured after formation of the washed and unwashed core-shell pouch cells when formed to either 4.1 V or 4.3 V UCVs. For all the electrolytes, there is more gas generation during formation for the unwashed core-shell pouch cells for both UCVs. The 2FEC1LFO additive combination generates the least amount of gas and the use of the MA co-solvent does not increase the gas generation in any significant way. The 4.3 V 1st cycle efficiency is similar for the washed and unwashed core-shell pouch cells,

but the 4.1 V 1st cycle efficiency is lower for the unwashed core-shell pouch cells which is not understood at this moment. R_{ct} values were lower when cells were formed to higher UCV. The negative electrodes reach a lower voltage vs. Li/Li^+ when a full cell charges to a higher voltage during formation, which may impact the impedance of the SEI formed as one study suggested.[175] The incorporation of LFO in the electrolyte generally causes a reduction in R_{ct} compared to cells with 2VC1DTD as has been previously reported.[45,176] When an LFO-containing electrolyte is used, the R_{ct} values of the washed and unwashed core-shell pouch cells are much more similar than when control or 2VC1DTD electrolytes are used.

Figure 7.3(b) shows the 1st charge dQ/dV vs. V plots of the washed and unwashed core-shell pouch cells. For all the electrolytes, their reduction voltages in both the washed and unwashed core-shell pouch cells are the same as those reported previously.[118,119] The use of MA co-solvents does not change the 2FEC1LFO reduction voltage.

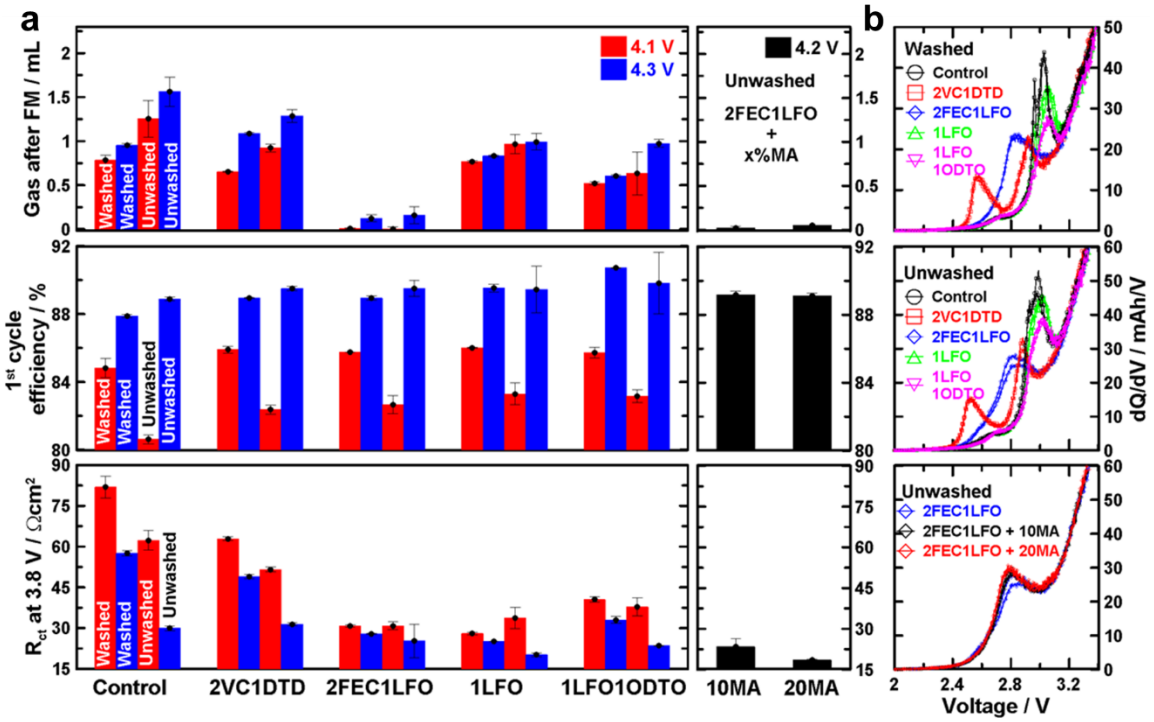

Figure 7.3(a) The gas generation during formation (FM), 1st cycle efficiency and the charge-transfer resistance R_{ct} at 3.8 V of the washed and unwashed core-shell pouch cell formed to 4.1 V, 4.2 V (only with MA co-solvent) and 4.3 V upper cut-off voltages. (b) The 1st charge dQ/dV vs. V plots of the washed and unwashed core-shell pouch cells from 2 to 3.4 V.

Figure 7.4 shows the discharge capacity, normalized capacity and normalized voltage polarization vs (a) cycle number and (b) time for the washed and unwashed core-shell pouch cells with different electrolytes. The cycling performance was tested at 40ºC from 3 to 4.18 V with C/3 (with respect to the washed core-shell pouch cell) CCCV mode. The 4.18 V pouch cell voltage approximately corresponds to 4.25 V vs. Li/Li^+ in half cell testing which includes the "H2-H3 remnants" shown in Figure 2. When plotting vs cycle number, the core-shell pouch cells with unwashed material showed similar capacity retention to the pouch cells with the washed material. However, when plotting vs time, the unwashed core-shell pouch cells showed better capacity retention than the washed ones. This is because it takes more time for the unwashed cells to complete one cycle since the true C-rate for the unwashed cells was about C/4.2, not C/3 as it was for the washed cells. At elevated temperatures such as 40ºC, time-based degradation can be more significant than cycle-based degradation,[177,178] so the results in Figure 7.4b suggest the unwashed pouch cells are actually performing slightly better than the washed ones. All cells show a dramatic increase in voltage polarization by a factor of ca. 2.5 over the 200 cycles and 1200 hours of the testing shown.

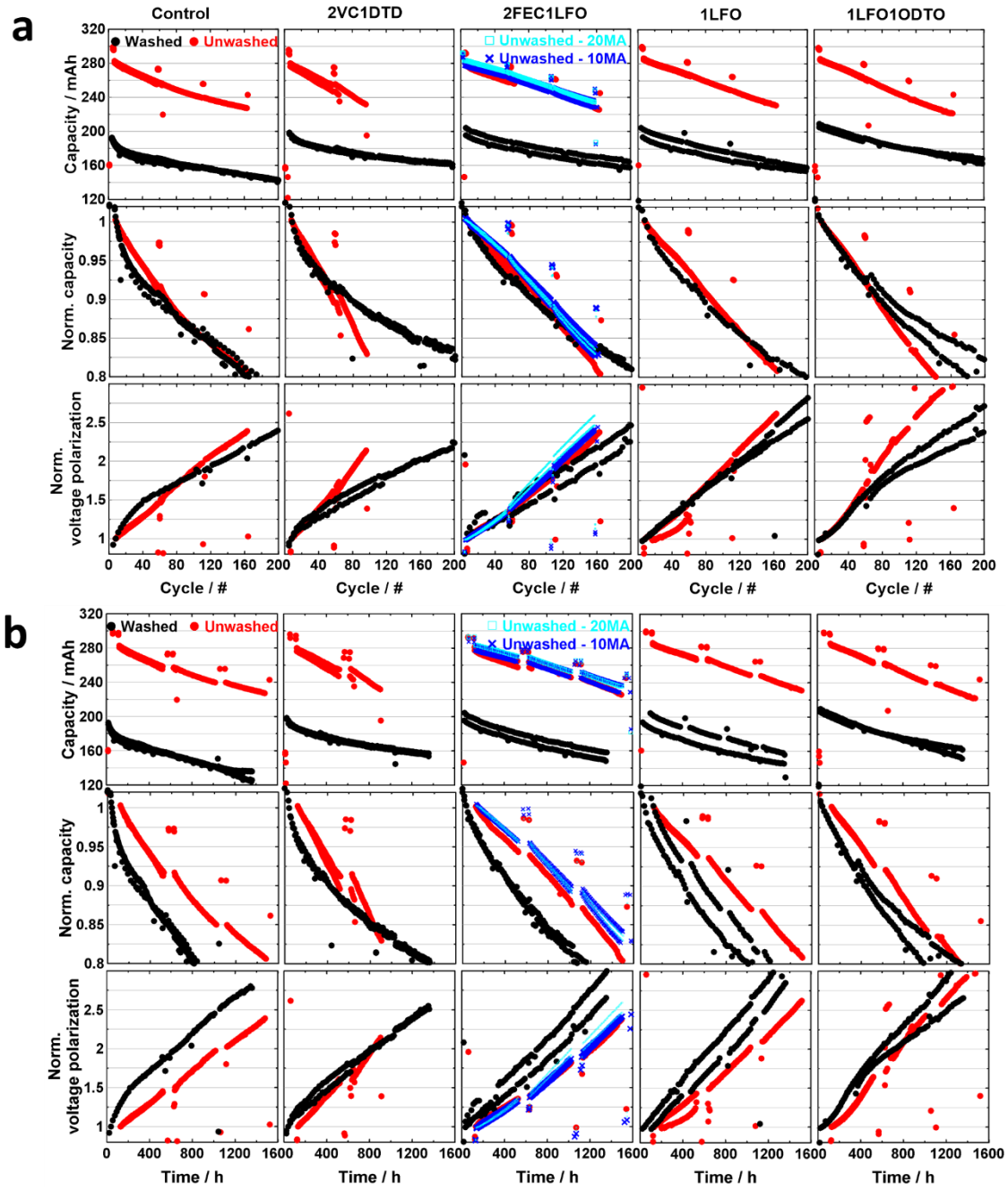

Figure 7.4 The discharge capacity, normalized capacity and normalized voltage polarization of the washed and unwashed core-shell pouch cells vs. (a) cycle and (b) time tested at 40°C from 3 to 4.18 V. The protocol is C/3 with respect to the washed core-shell pouch cell capacity in CCCV mode and a C/20 check-up cycle was measured every 50 cycles for the unwashed core-shell pouch cells. The 8th cycle discharge capacity and voltage polarization are taken as 1 for normalization.

Figure 7.5 shows the discharge capacity, normalized capacity and normalized voltage polarization vs (a) cycle number and (b) time of the washed and unwashed core-shell pouch cells containing different electrolytes. The cycling performance was tested at 40ºC from 3 to 4.04 V with C/3 (with respect to the washed core-shell pouch cell) CCCV mode and shows much improved capacity retention and voltage polarization compared to cycling with 4.18 V UCV. The 4.04 V pouch cell voltage approximately corresponds to 4.12 V vs. Li/Li^+ in half cell testing which excludes the "H2-H3 remnant" peak in dQ/dV vs V shown in Figure 7.2. Both the washed and unwashed core-shell pouch cells show an initial increase in normalized capacity. The initial increase in capacity during charge-discharge cycling is not uncommon but for the unwashed material cycled up to 4.04 V, the increase in initial capacity retention was as large as 10%. For all the unwashed cells in Figure 7.5, the capacity increase does not correspond to a decrease in cell impedance, as the voltage polarization remains more or less constant while the capacity increases. Most likely the capacity increase occurs because the cells are initially positive electrode limited on discharge (at C/3) and slowly become negative electrode limited as cycling proceeds. The C/20 check-up cycles in Figure 7.5 do not show the capacity increase with cycle number which supports this argument.

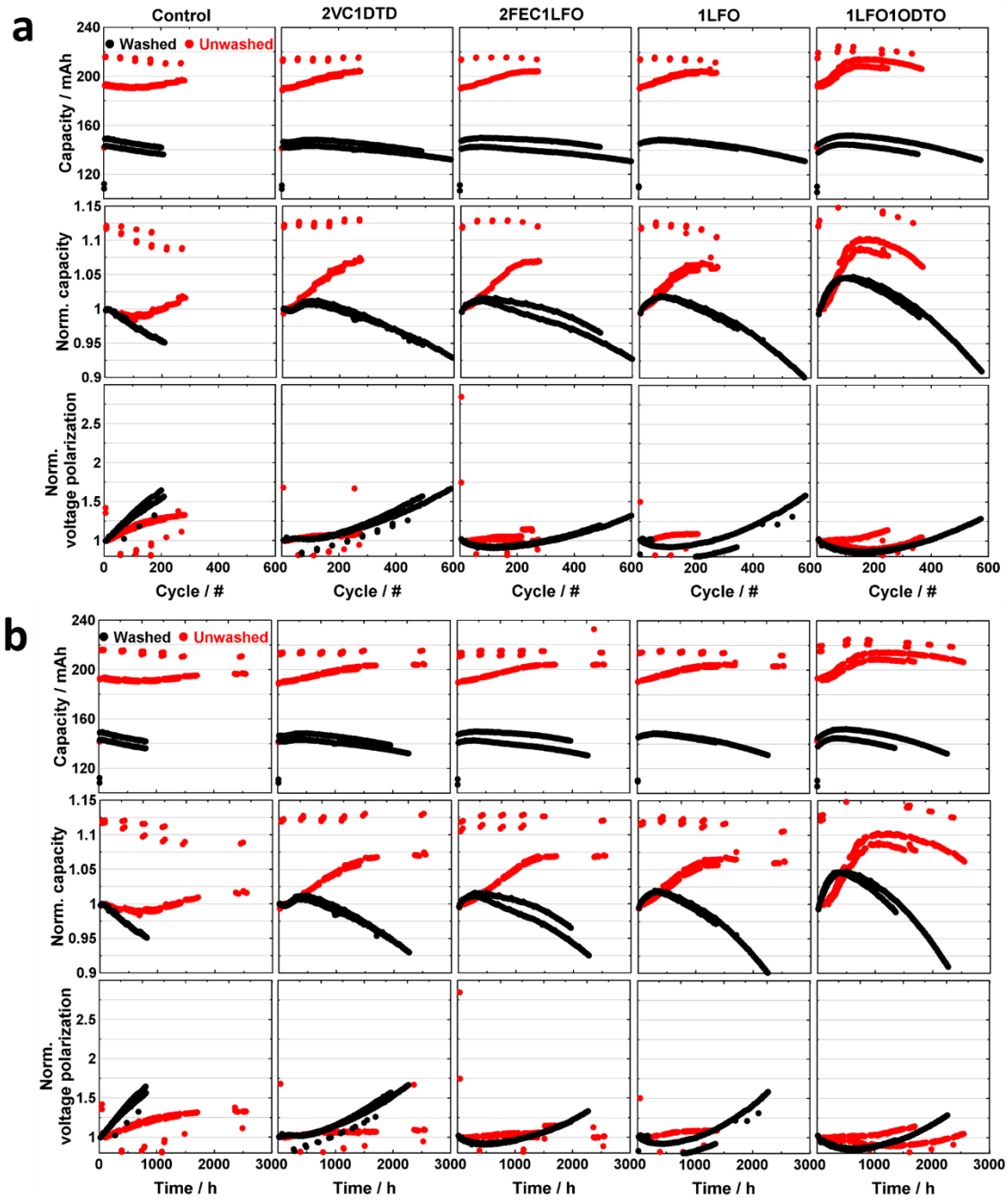

Figure 7.5 The discharge capacity, normalized capacity and normalized voltage polarization of the washed and unwashed core-shell pouch cells vs. (a) cycle and (b) time tested at 40°C from 3 to 4.04 V. The protocol is C/3 with respect to the washed core-shell pouch cell capacity in CCCV mode and a C/20 check-up cycle was measured every 50 cycles for the unwashed core-shell pouch cells. The 8th cycle discharge capacity and voltage polarization are taken as 1 for normalization.

Figure 7.6 shows the discharge capacity, normalized capacity and normalized voltage polarization versus cycle number and time of the washed and unwashed core-shell pouch cells with 2FEC1LFO and LFO additives. The cycling performance was tested at 20ºC from 3 to (a) 4.18 V and (b) 4.04 V with C/3 (with respect to the washed core-shell pouch cell) CCCV mode. Similar to the cycling performance at 40ºC shown previously, the unwashed core-shell pouch cells show better capacity retention than the washed version when plotted versus time. Cycling with a 4.04 V UCV has significantly better capacity retention and much lower voltage polarization than cycling with 4.18 V UCV. A large increase of capacity was also observed for the unwashed core-shell pouch cells tested at C/3, but unlike cycling at 40ºC in Figure 7.5, the C/20 check-up cycles also experience a small steady capacity increase with the 4.04 V UCV.

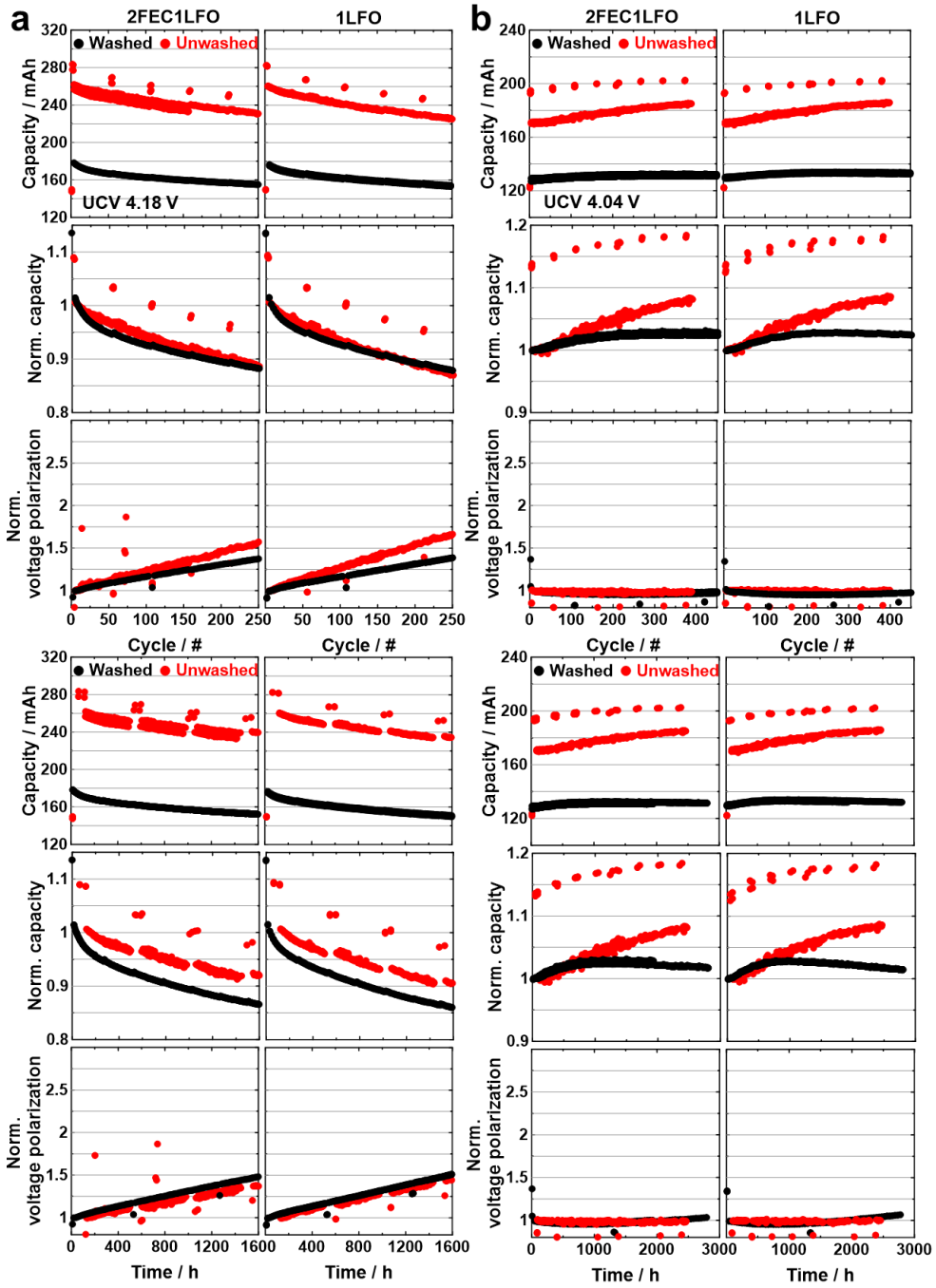

Figure 7.6 The discharge capacity, normalized capacity and normalized voltage polarization of the washed and unwashed core-shell pouch cells vs. cycle and time tested at 20°C from 3 to (a) 4.18 V and (b) 4.04 V with 2FEC1LFO and 1LFO electrolyte additives. The protocol is C/3 with respect to the washed core-shell pouch cell capacity in CCCV mode and a C/20 check-up cycle was measured every 50 cycles for the unwashed core-shell pouch cells. The 8th cycle discharge capacity and voltage polarization are taken as 1 for normalization.

Figure 7.7 shows the gas generation during charge-discharge cycling at 40ºC with 4.18 V (top panel) and 4.04 V (bottom panel) UCVs. The cycling data for these cells have been shown in Figure 7.4 and Figure 7.5. When cycling with a 4.18 V UCV, the gas generation from the unwashed material nearly doubles compared to that from the washed material for all additives except for the control electrolyte. Given that the volume of the pouch cell (excluding the gas bag) is about 2.5 mL, the top panel of Figure 7.7 shows that unacceptable amounts of gas are being generated for all of the unwashed cells. When cycling with the 4.04 V UCV, the gas generation is around an order of magnitude lower than the 4.18 V UCV case. Though the gas generation during formation can be lowered by carefully selecting electrolyte additive blends such as using 2FEC1LFO as shown in Figure 7.3 even in unwashed core-shell pouch cell, the gas generation during cycling still shows that positive electrode materials with surface lithium residues generate significantly more gas, especially when cycled to 4.18 V.

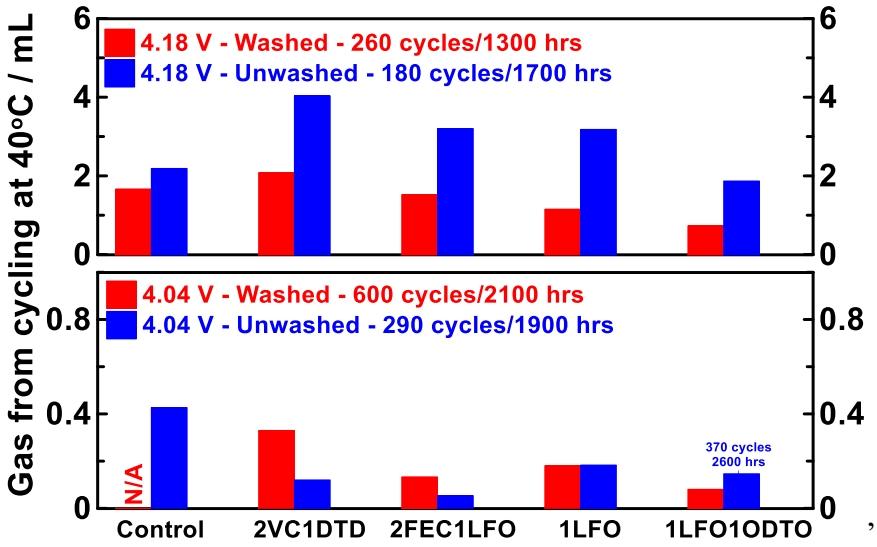

Figure 7.7 The gas generation during charge-discharge cycling at 40ºC with 4.18 V UCV (top panel) and 4.04 V UCV (bottom panel) for the washed and unwashed core-shell pouch cell. The gas generation for the unwashed core-shell pouch cell with 4.04 V UCV and 1LFO1ODTO electrolyte was measured after 370 cycles/2600 hours.

Figure 7.8 (a) shows the dQ/dV changes when the pouch cells were discharged using various C-rates. The C-rate was determined based on the discharge capacity of formation. For both the washed and unwashed core-shell pouch cells, high discharge rate impacts the

"H2-H3 remnant" region most when discharging from 4.18 V (ca. 4.25 V vs. Li/Li^+). This shows the "H2-H3 remnant" is more rate-sensitive than the rest of the dQ/dV peaks. A study of Li-ion diffusion in Li_xNiO_2 by Phattharasupakun et al.[100] has shown the lowest diffusion coefficient above 3.6 V vs. Li/Li^+ occurs at 4.25 V vs. Li/Li^+, which explains the poor rate capability over the "H2-H3 remnant" region. Similar results were also observed by A. Liu et al.[179] on single and polycrystalline $LiNi_{0.975}Mg_{0.25}O_2$.

Figure 7.8(b) compares the rate capability of the washed and unwashed core-shell pouch cells. Regardless of the UCV, the pouch cell rate capability does not appear to be influenced by the presence of surface lithium residues on the core-shell material at least up to 2C rate.

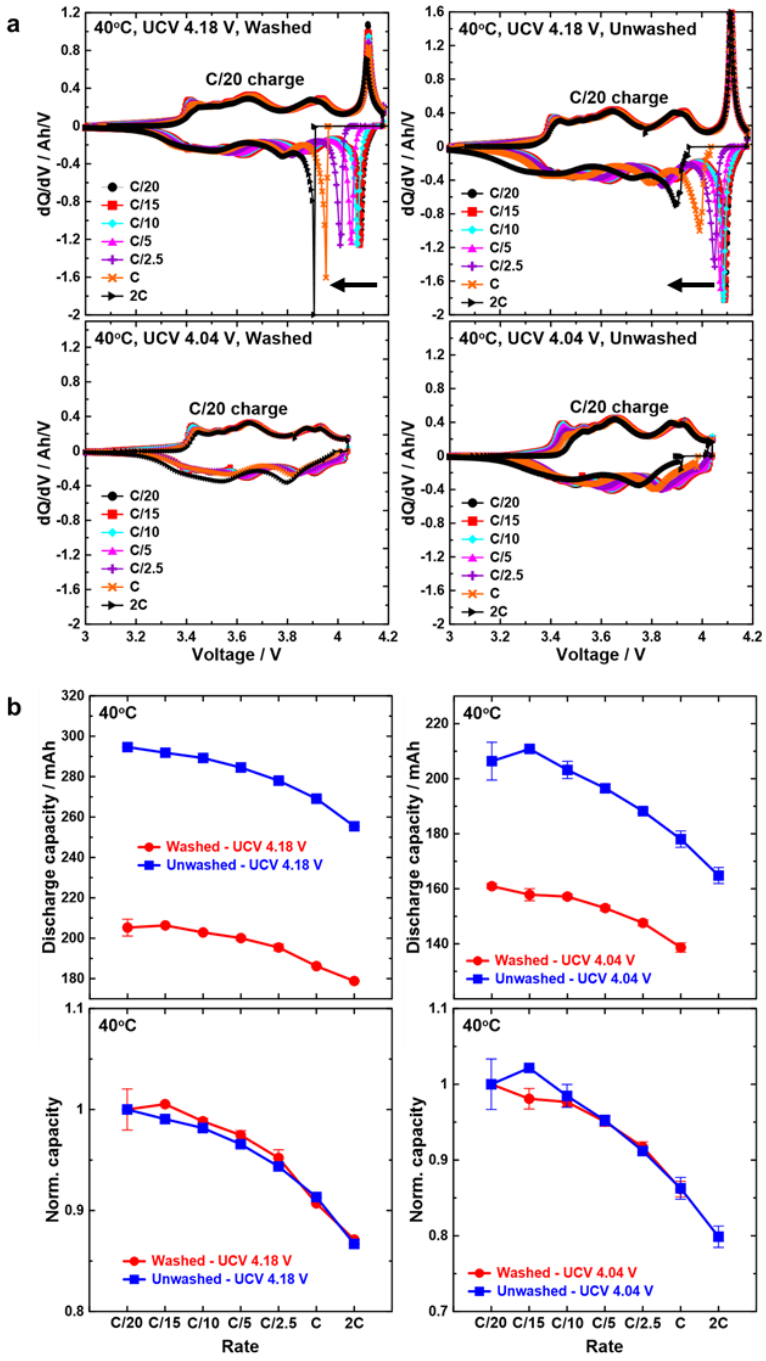

Figure 7.8(a) dQ/dV versus V curves of the washed and unwashed core-shell pouch cells as a function of discharge C-rate with 4.18 V and 4.04 V upper cut-off voltages (UCV) measured at 40°C. The arrows indicate the direction of increasing of C-rate for the discharge data (b) The discharge capacity and normalized capacity as a function of discharge C-rate. The C/20 discharge capacity was taken as 1 for normalization.

7.4 Conclusions

Washed and unwashed polycrystalline Ni-rich Co-free core-shell materials were evaluated and compared in this work. Both the washed and unwashed materials have an average composition of $LiNi_{0.94}Mn_{0.06}O_2$ and were prepared from a precursor that has a 16 μm $Ni(OH)_2$ core and a 1 μm thick $Ni_{0.8}Mn_{0.2}(OH)_2$ shell. This is a core-shell composition reported previously in Chapter 4 to Chapter 6 and in references.[8,17,148]. The washed core-shell material maintained the core-shell structure but powder XRD refinement showed an increased fraction of Ni atoms in the Li layer and crushing tests showed worse mechanical strength compared to the unwashed material. The use of 0.7 wt.% oxalic acid in the slurry formulation eliminated the gelation problem of the unwashed material so that electrodes could be made and pouch cells could be built. Half cell charge-discharge cycling using punched single-side-coated electrodes from pouch cells showed that the washed material had worse performance than the unwashed material between 3 and 4.25 V vs. Li/Li^+ at 30ºC. Washed pouch cell charge-discharge cycling also showed worse performance than the unwashed cells as a function of time at both 20ºC and 40ºC. The rate capabilities of the washed and unwashed core-shell pouch cells were virtually the same before long term cycling and the high-discharge rate significantly impacted the high voltage "H2-H3 remnant" region regardless of the washing condition. The washed core-shell pouch cells generated a lot less gas than the unwashed cells for the control, 2VC1DTD, 2FEC1LFO, 1LFO and 1LFO1ODTO electrolyte blends with 1.5 M $LiPF_6$ when cycling with 4.18 V UCV at 40ºC.

The pouch cells tested to an upper cut-off of 4.04V showed reasonable amounts of gas production, excellent capacity retention and minimal impedance growth at both 20 and 40ºC. By contrast, cells tested to an upper cut-off of 4.18V showed significant amounts of gas production at 40ºC, poor capacity retention and significant impedance growth at both 20 and 40ºC. These results highlight once again the difficulties associated with simultaneously obtaining very high energy density and long lifetime with Ni-rich materials.

Chapter 8 Comparison of the Washed Core-shell Material with Commercially-available Materials in Pouch Cells

8.1 Introduction

In Chapter 7, gelation problem of the unwashed core-shell material was alleviated so that the performance of the washed and unwashed core-shell material was able to be compared in pouch cells. Gas generation during cycling at 40°C with 4.18 V OCV showed the unwashed material generated much more gas than its washed version, which could cause severe safety issue. In this chapter, the washed core-shell material is compared to the commercially available material $LiNi_{0.5}Mn_{0.3}Co_{0.2}O_2$ (SC532) and $LiNi_{0.8}Mn_{0.1}Co_{0.1}O_2$ (SC811). Special attention is given to the impact of the "H2-H3 phase transition remnant" ("H2-H3 remnant" for short), if any, on the cycling performance of these three positive electrode materials.

8.2 Experimental

Coated single crystal SC532 was provided by Vendor 1 and is the same material featured in reference [159]. Uncoated single crystal SC811 was provided by Vendor 2 and is the same material featured in reference [80]. The washed core-shell oxide is the same as used in Chapter 7 and named Ni94 here for simplicity of discussion as its Ni content is 94%. Coin cell building and electrolytes used are indicated in Chapter 3

The *in-situ* XRD studies of SC532, SC811 and $LiNi_{0.95}Mn_{0.05}O_2$ (not to be confused with core-shell Ni94), and the following unit cell volume determination versus voltage or lithium content were carried out in previous work.[57,63]

Two pouch cell testing protocols were used. In the protocol for long term cycling measured at 20 and 40°C, two upper cut-off voltages (UCVs) were selected for each positive material. The SC532 cells were cycled from 3.0 to either 4.1 V or 4.3 V. The SC811 cells were cycled from 3.0 to either 4.06 V or 4.2 V. The core-shell Ni94 cells were cycled from 3.0 to either 4.04 V or 4.18 V. The pouch cell voltage polarization is defined as the average voltage difference between the charge and discharge curves of the

same cycle. The capacity and voltage polarization of the 5th cycle was taken as 100%. The SC532 and SC811 cells were measured with C/3 CCCV mode at 40ºC and 1C CCCV mode at 20ºC. All the core-shell Ni94 cells were measured with C/3 CCCV mode at both 20ºC and 40ºC. The 2nd protocol was adopted only for the Co-free core-shell Ni94 pouch cells with 2FEC1LFO additive measured at 20ºC and 40ºC, C/3 CCCV mode. The pouch cell was cycled with alternating UCVs of 4.18 V and 4.04 V. The UCVs were alternated every 10 cycles.

8.3 Results and Discussion

8.3.1 Unit Cell Volume Change Over "H2-H3 remnant" Region

Figure 8.1 (a) shows the voltage (vs. Li/Li$^+$) vs. specific capacity of the SC532, SC811 and the washed core-shell Ni94 positive electrode materials measured at 30ºC. Increasing the Ni content increases the first charge capacity as expected. The irreversible capacity depends on a number of factors such as the Li-ion diffusion constant at low potentials, the discharge rate and the primary particle size.[100,179,180] The diffusion constant is affected by the material composition and also by the fraction of Ni atoms in the Li layer. There is no simple relationship between material composition and irreversible capacity.

Figure 8.1 (b) shows the dQ/dV curves (left y-axis) and the unit cell volumes (right y-axis) of the SC532, SC811 and homogenous $LiNi_{0.95}Mn_{0.05}O_2$ (not to be confused with Ni94) as a function of voltage. The "H2-H3 phase transition remnant" peaks at around 4.2 V become sharper in intensity as the Ni content increases. The capacity in this region also contributes more to the overall specific capacity as the Ni content increases. In addition, the unit cell volume experiences a dramatic decrease as the materials are charged through this peak in dQ/dV, especially for $LiNi_{0.95}Mn_{0.05}O_2$. This shows that in order to access more capacity for Ni-rich materials, a large lattice volume change will be inevitable.

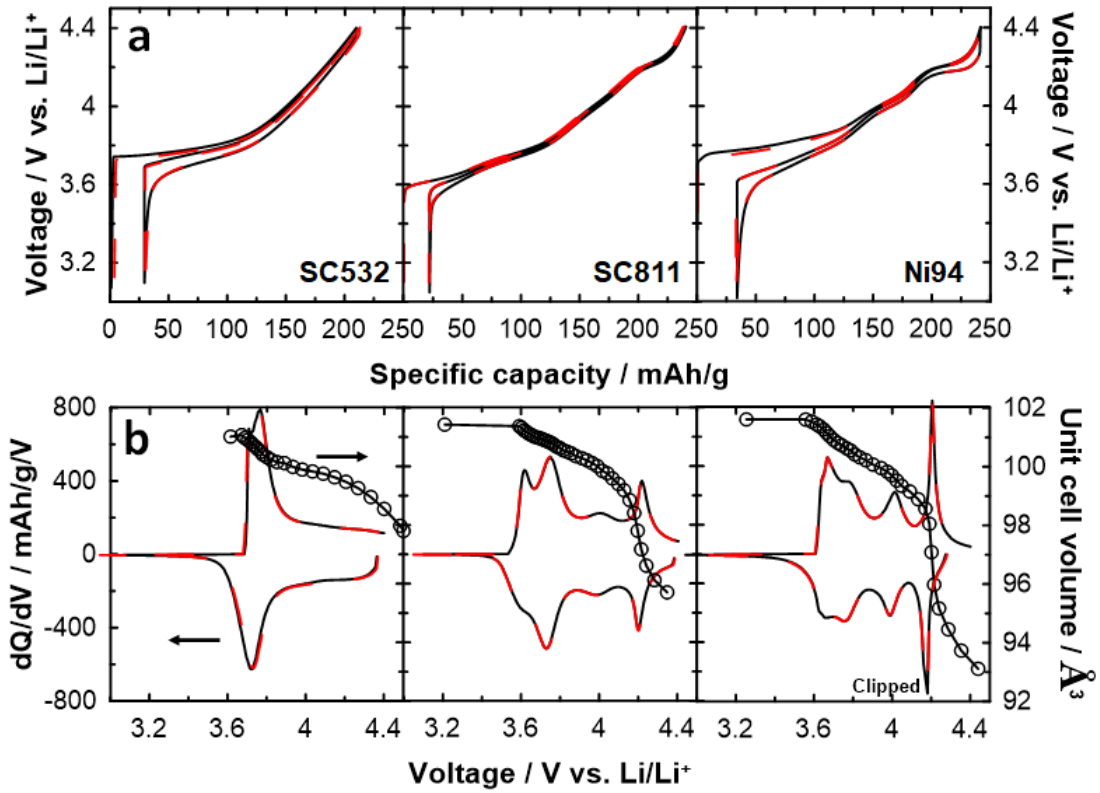

Figure 8.1 (a) The voltage vs. specific capacity of the SC532, SC811 and the washed Co-free core-shell Ni94 for the 1st 1.5 cycles measured at 30°C, C/20 from 3.0 to 4.4 V. (b) dQ/dV of the 1st discharge and 2nd charge (left y-axis) and the unit cell volumes (right y-axis) of SC532, SC811 and homogenous $LiNi_{0.95}Mn_{0.05}O_2$ (not to be confused with Ni94) vs. V. The black and red curves are data from duplicate cells. The unit cell volume data was taken from reference 63

8.3.2 Impact of "H2-H3 remnant" on Pouch Cell Performance

Figure 8.2 shows the amount of gas generated during formation (left column) and the charge-transfer resistance R_{ct} measured after formation (right column) as a function of the five electrolyte blends for the SC532, SC811 and the core-shell Ni94 pouch cells. The formation was done by charging to two different UCVs. The formation current was the same for the two UCVs of each cell type. This means the formation time was slightly longer when charging to a higher voltage.

For the gas generation, the 2FEC1LFO additive combination generates the least amount of gas regardless of which positive electrode material was used in the pouch cells. For each additive, the amount of gas generated in SC532 cells is similar to that in SC811 cells,

which suggests the gas generated was primarily a result of SEI formation on the negative electrode. However, for the Ni94 cells with 2VC1DTD, the amount of gas generated was higher when formed to 4.3 V than when formed to 4.1 V. When LFO was added to the electrolyte in the Ni94 cells, the amount of gas generated when formed to 4.1 or 4.3 V was almost the same.

The charge-transfer resistances, R_{ct}, were generally slightly lower when cells were formed to higher UCV for all the positive electrode materials studied here. It is not very clear to the authors at this moment why charging to a high voltage lowers the R_{ct} value. When a full cell charges to a higher voltage during formation, the negative electrodes reach a lower voltage vs. Li/Li$^+$ which may impact the impedance of the SEI formed.[175] The incorporation of LFO to the electrolyte generally causes a reduction in R_{ct} compared to cells with 2VC1DTD as has been previously reported.[45,176]

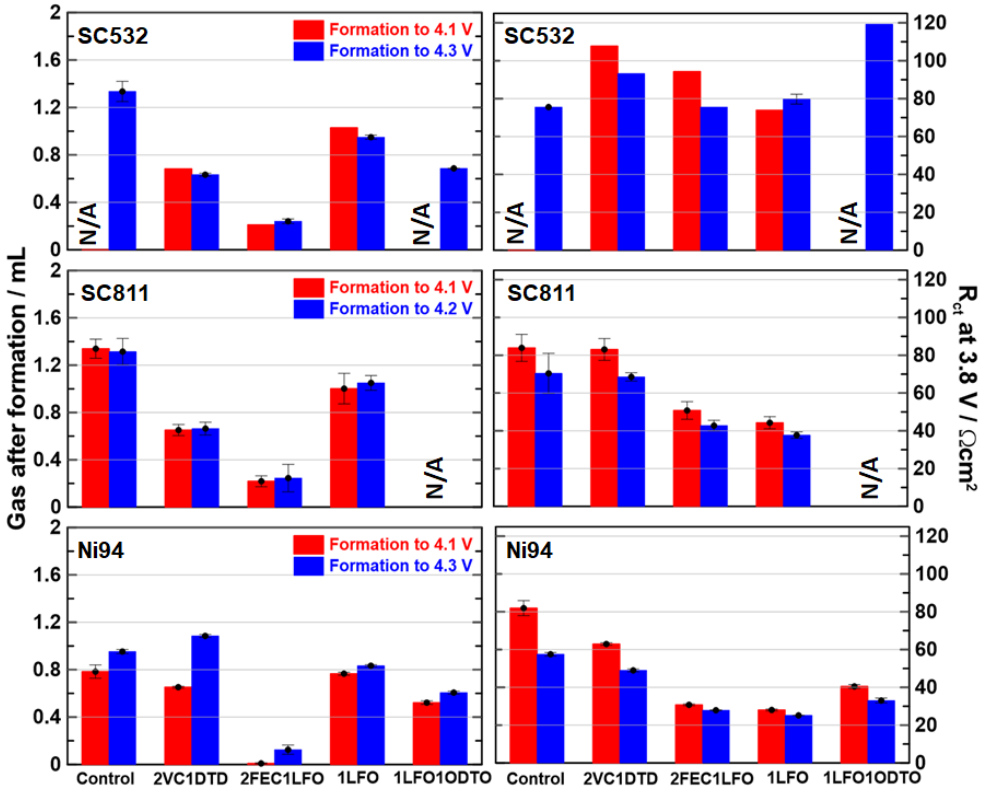

Figure 8.2 The gas generation (left column) during formation and the charge-transfer resistance R_{ct} (right column) after formation for the SC532, SC811 and core-shell Ni94 pouch cells as a function of electrolyte blends. The data shown without error bars were digitized from J. Li et al.,[43] L. Ma e al.,[119] and X. Ma et al.[118]

Figure 8.3 shows the cell balancing of the SC532, SC811 and the core-shell Ni94 cells as determined by the dV/dQ analysis method.[181] The goodness-of-fit of the dV/dQ method is shown qualitatively in Figure C.1. The corresponding positive electrode voltages are labeled when the full cell is charged to 4.1 V and 4.3 V for SC532 (a), 4.06V and 4.2 V for SC811 (b), as well as 4.04 V and 4.18 V for the core-shell Ni94 (c). The inset images show dQ/dV vs. V of the corresponding positive electrode and the dashed lines indicate the corresponding low and high UCVs for the positive electrode vs Li/Li^+. The "H2-H3 remnant" peaks of the positives, bounded by the dashed lines in the inset dQ/dV curves, are excluded when the full cells are charged to 4.06 V for SC811 and 4.04 V for Ni94. Please note that for SC532 cells, the "H2-H3 remnant" is not observed even at 4.3 V.

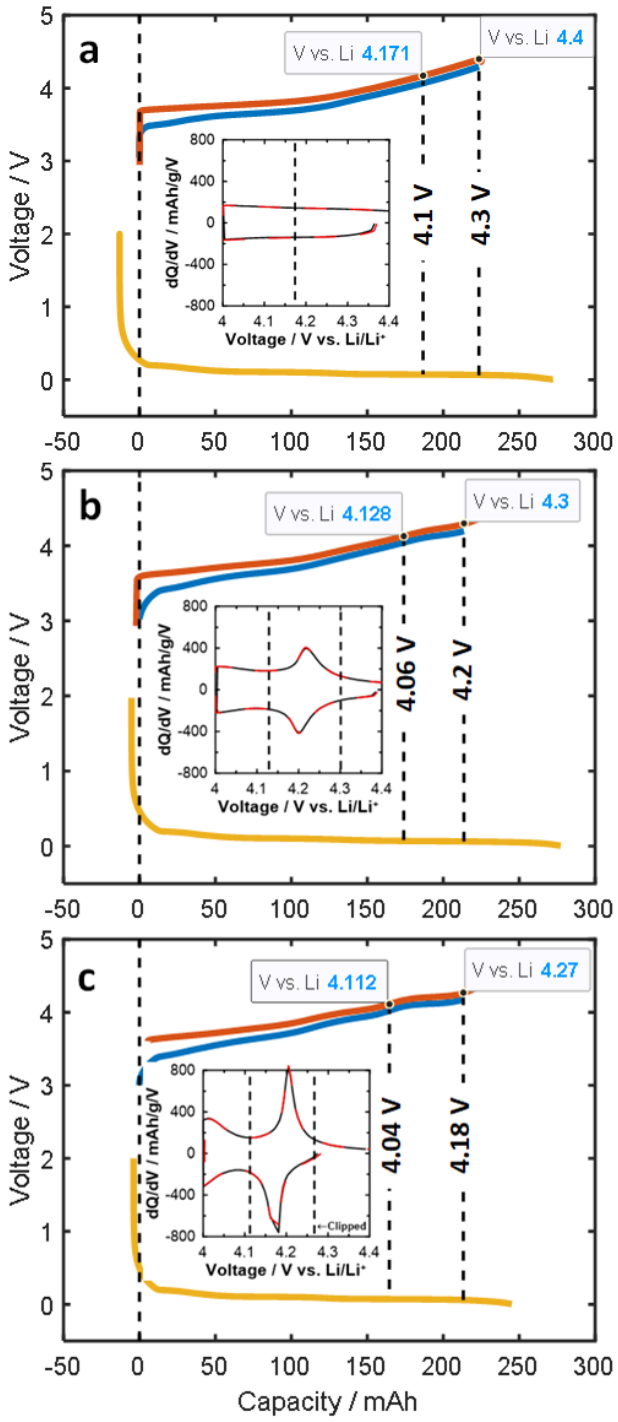

Figure 8.3 Pouch cell electrode balances for the SC532 (a), SC811 (b) and the core-shell Ni94 (c) measured on the 2nd charge. The dashed lines indicate the two UCVs of the full cells with the positive electrode voltage labeled. The dashed lines in the inset indicate where the labeled positive electrode voltages are in the dQ/dV vs. V plots.

Figure 8.4 shows the charge-discharge cycling performance of the SC532, SC811 and the core-shell Ni94 pouch cells when the UCVs **include** the "H2-H3 remnant" for SC811 and Ni94. Both the SC811 and Ni94 pouch cells show poor capacity retention without electrolyte additives (control electrolyte). With the help of additives, the performance of SC811 cells was significantly improved and the core-shell Ni94 cells reach 200 cycles at 80% retention. The capacity retention decreased as Ni content increased with 2VC1DTD, 2FEC1LFO and 1LFO additives. The SC532 cells charged only to 4.3 V do not pass through a large volume change region (Figure 8.1b) and they show excellent capacity retention and very little impedance growth. Both the SC532 and SC811 are very robust to particle microcracking, so the differences in capacity retention and voltage hysteresis could be a result of parasitic reactions between the positive electrode material and the electrolyte.[80] Jung et al.[182] showed that oxygen release from $LiNi_xMn_yCo_zO_2$ positive electrode materials causing chemical oxidation of the electrolyte occurs coincidentally with the large volume contraction which occurs near the "H2-H3 remnant". This reaction will occur in the case of SC811 but should not occur in the case of SC532. For the polycrystalline core-shell Ni94, Y. Liu et al.[8] have shown in coin cells that though the high Ni-content core (nominally 100% Ni) showed cracking when cycled up to 4.3 V vs. Li/Li^+ for 100 cycles, the shell (nominally 80% Ni) did not. This material was shown to have comparable capacity retention with SC811 in half coin cells. However, the Ni94 pouch cells have a very poor capacity retention and the rate of voltage polarization growth is enormous compared to the SC811 and SC532 cells. The author speculates this may be related to impact of standard industrial processing on the characteristics of this material. The details of how the Ni94 was processed were not revealed to the author.

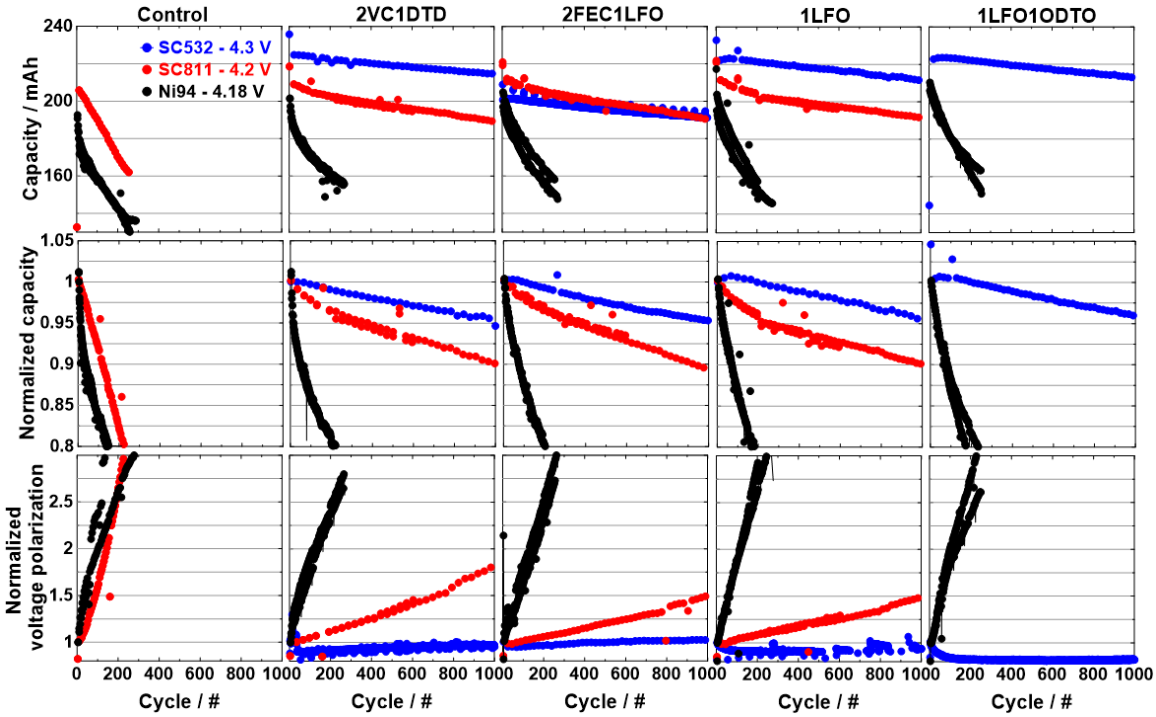

Figure 8.4 Capacity, normalized capacity and normalized voltage polarization vs. cycle for five electrolyte blends measured at 40°C, C/3 CCCV when the UCVs include the "H2/H3 remnant" for the case of SC811 and Ni94. The 5th cycle is chosen as "1" for the normalization.

Figure 8.5 shows the cycling performance of SC532, SC811 and the core-shell Ni94 pouch cells when the UCVs were chosen to **exclude** the "H2-H3 remnant". The most obvious difference between Figure 8.4 and Figure 8.5 is the vastly improved capacity retention for the Ni94 cells charged to only 4.04 V as well as a dramatic reduction in the rate of growth of voltage polarization. Similarly, the capacity retention and impedance growth for the SC811 cells charged to 4.06 V in Figure 8.5 are vastly improved compared to Figure 8.4 when the cells were charged to 4.2 V. These comparisons highlight the fact that the "H2-H3 remnant" is detrimental to cells that require extremely long lifetime. Even a material like the Ni94 used here where capacity degrades very rapidly when used in cell operated to 4.18 V (charging through the "H2-H3 remnant" on every cycle) is relatively acceptable when operated to only 4.04 V by avoiding the "H2-H3 remnant".

One interesting thing to note is that penalty in absolute cell capacity which occurs by reducing the UCVs from 4.3 to 4.1 V for SC532, from 4.2 to 4.06 V for SC811 and from 4.18 to 4.04 V for Ni94. The cell capacity decrease is the largest for the core-shell Ni94

cells. This is because the "H2-H3 remnant" contributes a larger portion of its capacity, so avoiding this remnant causes a dramatic capacity reduction. This suggests that the longest-lived cells, operated to avoid the "H2-H3 remnant", with the highest capacity will not be made with positive electrode materials with extremely high Ni contents.

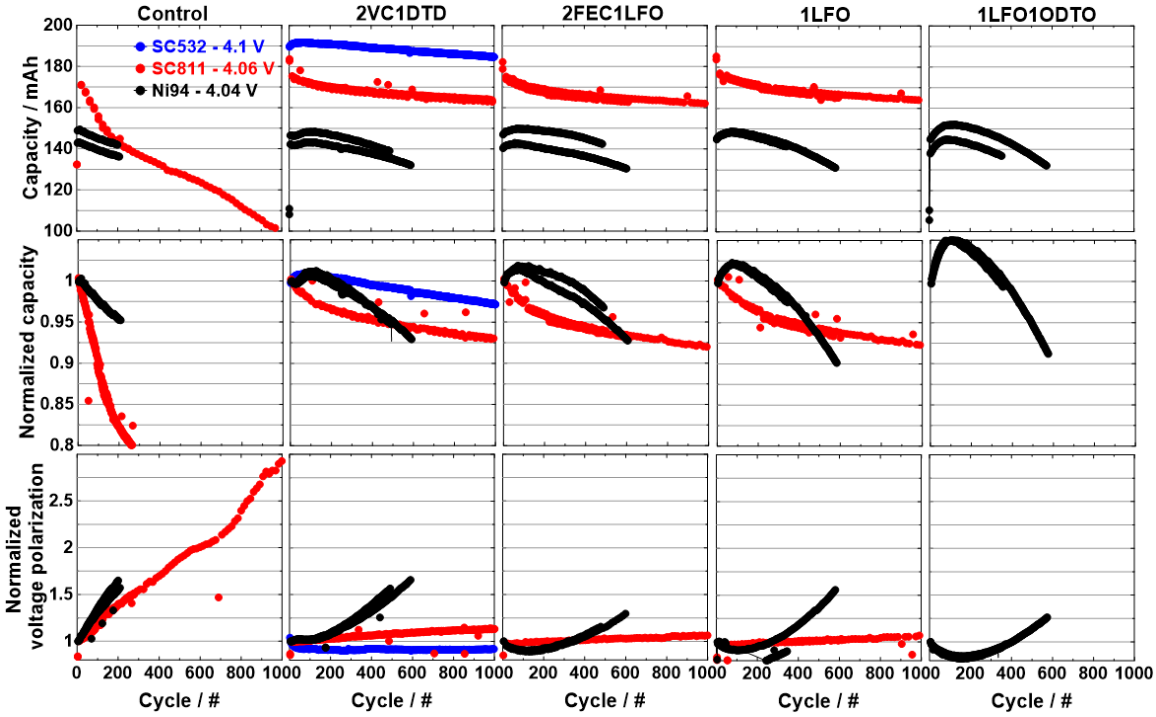

Figure 8.5 Capacity, normalized capacity and normalized voltage polarization vs. cycle for five electrolytes measured at 40°C, C/3 CCCV when the UCVs exclude the "H2/H3 remnant". The 5th cycle is chosen as "1" for the normalizations.

Figure 8.6 shows the cycling performance for pouch cells with the 2FEC1LFO and 1LFO electrolyte blends at 20°C when the "H2-H3 remnant" was either included (a) (note that SC532 cell has no "H2-H3 remnant" even at 4.3 V) or excluded (b). The cycling performance of the core-shell Ni94 was significantly improved at 20°C compared to cycling at 40°C for both UCVs. The capacity retention with 4.18 V UCV is almost tripled at 20°C compared to at 40°C. For both UCVs, the significantly lower voltage polarization increase with cycle numbers at 20°C compared to 40°C highlights the strong dependency of the side reactions between the electrodes and the electrolyte on temperature. The Ni94 cells charged to only 4.04 V at 20°C operate without capacity loss and the impedance growth is equal to that of the SC811 cells. Again, by comparing the difference of cycling

performance in Figure 8.6(a) and (b), it is striking how much the capacity retention can be improved by avoiding the "H2-H3 remnant" especially for Ni94 cells.

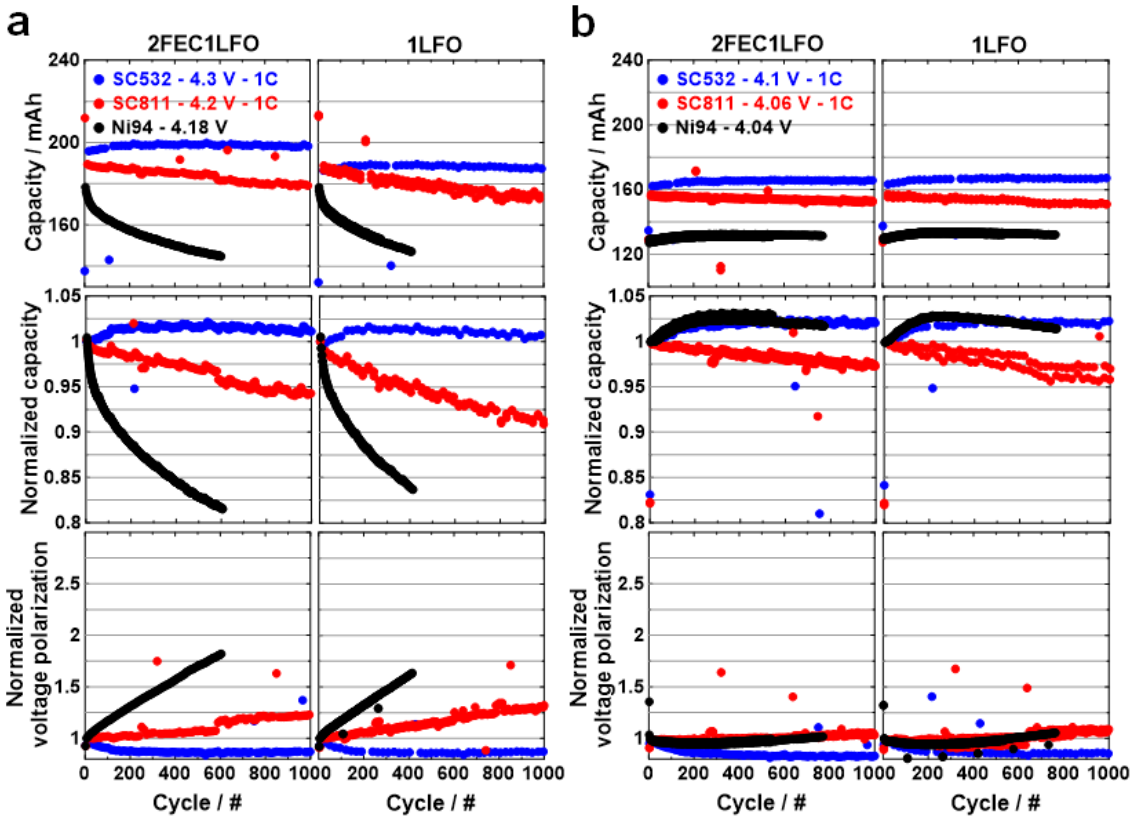

Figure 8.6 Capacity, normalized capacity and normalized voltage polarization vs. cycle for 2FEC1LFO and 1LFO electrolyte blends measured at 20ºC when the UCVs include (a) and exclude (b) the "H2/H3 remnant". The 5th cycle is chosen as "1" for the normalizations. The SC532 and SC811 cells were measured with 1C CCCV. The core-shell Ni94 was measured with C/3 CCCV.

Figure 8.7(a) shows two negative electrodes extracted from core-shell Ni94 pouch cells with control electrolyte or 2FEC1LFO electrolyte blend that were cycled at 40ºC, C/3 CCCV with 4.18 V UCV. The charge-discharge cycling performance of these cells is shown in Figure 8.4. The control and 2FEC1LFO cells were cycled to the 290th and 270th cycle, respectively, before disassembly at 4.18 V. Both cells were slowly charged to 4.18 V and voltage hold at 4.18 V for 30 hours before opening in glove-box. Both negative electrodes showed a uniform gold color indicating uniform lithiation,[37] even though the

pouch cell with control electrolyte experienced worse capacity loss compared to the cell with the 2FEC1LFO additive. By the look of the graphite negative electrodes, there appears to have been no significant mass and lithium inventory loss, which also implies there is no significant SEI thickening. Therefore the impedance growth from the negative side is expected to be low and the fast capacity fade of the core-shell Ni94 cell is most likely due to the impedance growth from the positive electrode. The different performance of the cells with control and 2FEC1LFO electrolyte blends can be a result of the different ability to inhibit the impedance rise of the positive electrode by the electrolyte.

Figure 8.7(b) shows the cross-section SEM images of a fresh electrode from a dry core-shell Ni94 pouch cell. The SEM images show many of the particles have been fractured due to the calendaring process. Figure 8.7(c) and (d) show cross-section SEM images of positive electrodes from two cycled pouch cells with control electrolyte. The pouch cell dissembled in Figure 8.7(c) was cycled to 4.18 V UCV for 290 cycles at 40ºC. This is the cell with control electrolyte shown in Figure *8.4* and its negative electrode was examined in Figure 8.7(a)**.** The pouch cell dissembled in Figure 8.7(d) was cycled to 4.04 V UCV for 200 cycles at 40ºC**.** This is the cell with control electrolyte shown in Figure 8.5. Particles in both electrodes show microcracking. Even though the *in-situ* XRD in Figure 8.1 and many other reports in the literature indicate the generation of microcracking when a polycrystalline material was repeatedly cycled to high voltage,[42,75,183] it is difficult from these SEM images to tell whether the microcracks were generated due to initial calendaring or induced by anisotropic volume change from repeatedly cycling to a high voltage. The goal of using a core-shell structure is to protect the Ni-rich core from the electrolyte exposure using a low Ni content shell so that both high capacity and long cycle life can be achieved. Therefore, the microcracks due to calendaring are particularly detrimental for the core-shell Ni94 material as the Ni-rich core will have a direct exposure to the electrolyte which is expected to cause severe side reactions during cycling. It was shown previously that the SC532 and SC811 fresh electrodes have minimal microcracking from calendaring, which highlights the advantageous processing ability of single crystal materials compared to the polycrystalline ones.[80]

8.3.3 Degradation Analysis

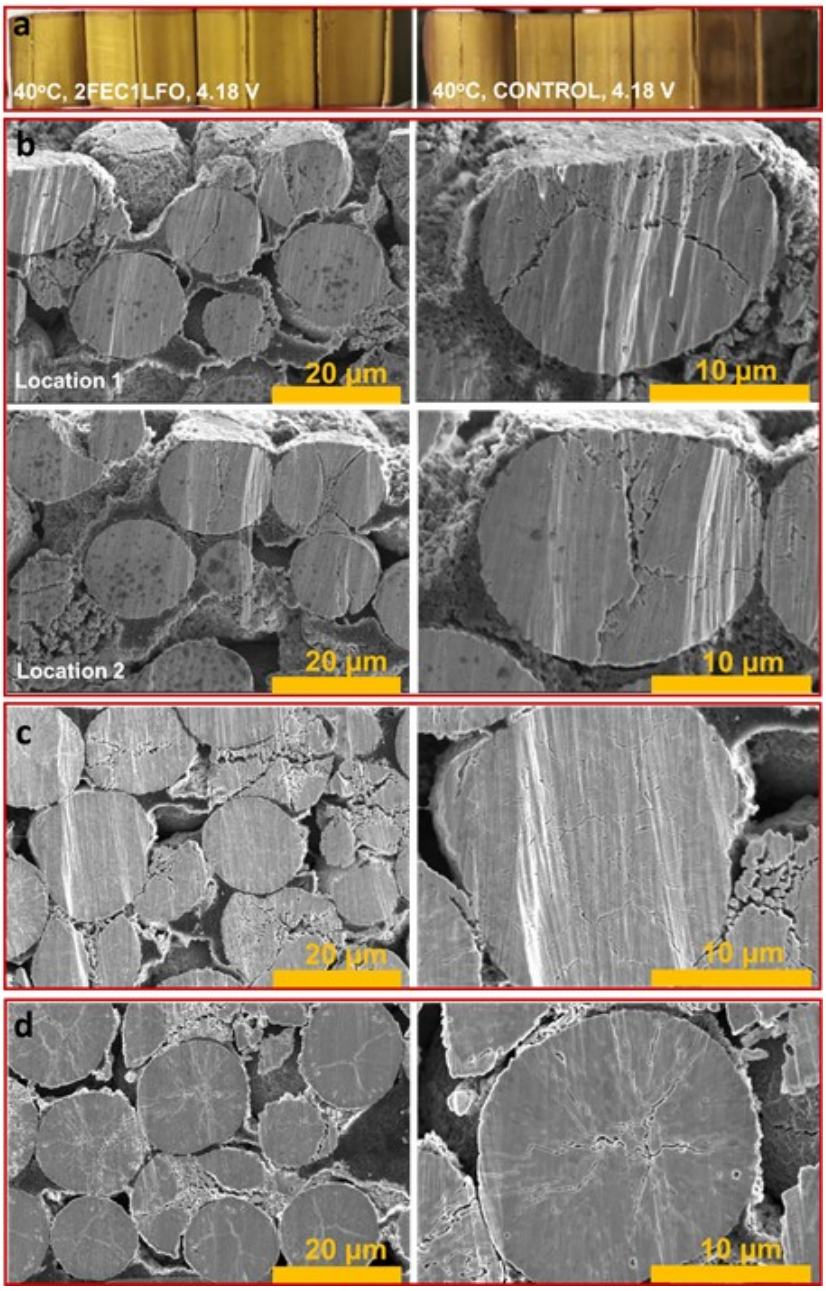

Figure 8.7 (a) The harvested graphite negative electrodes at 4.18 V from pouch cells cycled with control (290 cycles) and 2FEC1LFO (270 cycles) electrolyte at 40ºC, C/3 CCCV. (b) Cross-section SEM images of two locations of a fresh core-shell Ni94 electrode punched from a dry pouch cell. (c) Cross-section SEM images on a cycled Ni94 electrode with a 4.18 V UCV and control electrolyte (290 cycles) at 40ºC (d) Cross-section SEM images a on cycled Ni94 electrode with a 4.04 V UCV and control electrolyte (200 cycles) at 40ºC.

Figure 8.8 (a) shows the C/20 and C/5 dQ/dV curves of the core-shell Ni94 and the SC811 before and after cycling from 3 to 4.3 V vs. Li/Li^+ in coin cell half-cells at 30ºC. The C/20 dQ/dV curve of the core-shell Ni94 remains stable only up to ca. 4.1 V, whereas that of the SC811 is virtually unchanged over the entire voltage range. The significant change of the core-shell Ni94 dQ/dV curve occurs around the so-called "H2-H3 remnant" at the 4.2 V dQ/dV region where a large volume contraction occurs according to *in-situ* XRD. Half-cell cycling with C/20 ensures that impedance contributions to capacity fade are negligible. If there is any portion of the active material permanently disconnected from the conducting network, one would expect the entire area enclosed by the dQ/dV curve to decrease by that portion, instead of only influencing the "H2-H3 remnant" region. It is therefore reasonable to believe that it is only a temporary active material disconnection from the conducting network due to the lattice volume contraction over the "H2-H3 remnant" region.[39] Once the material expands again, it is reconnected to the conducting network so that the dQ/dV curve below 4.1 V remains stable. On the other hand, the SC811 half cell shows virtually no changes around its 4.2 V peak region, which may imply all the active particles are well-connected to the conducting network even though it also experiences a large lattice volume change over this region. This difference from the core-shell Ni94 is most likely due to the single crystal structure without microcracking that helps minimize electric-disconnection over the high voltage range, whereas, for the polycrystalline core-shell Ni94, the microcracking by electrode calendering might even exacerbate the electric-disconnection. In the C/5 cycling case of the core-shell Ni94 half cell, the 4.2 V peak from charging almost entirely vanishes after cycling and even the middle range of the dQ/dV curve has shifted in voltage which indicates a large impedance effect. The SC811 shows very stable C/5 cycling over the entire voltage range. The coin cell half-cell cycling data is shown in Figure C.2.

Figure 8.8(b) shows the C/3 CCCV cycling performance of a core-shell Ni94 pouch cell tested with alternating UCVs at 40ºC and 20ºC. When cycling with a 4.18 V UCV, the cell capacity decreases significantly faster compared to when the UCV is 4.04 V. In fact, at 40ºC, the capacity versus cycle number segments for the 4.04 V UCV are virtually

horizontal and all capacity loss occurs during the 4.18 V cycling. The situation is similar at 20°C. This behavior strongly suggests a recommended use mode for cells with any high Ni content positive electrode. If a large discharge capacity is not required, charging to a voltage below the "H2-H3 remnant" will help preserve cell life time. The user should only charge to a voltage beyond the "H2-H3 remnant" in cases when a large discharge capacity is needed.

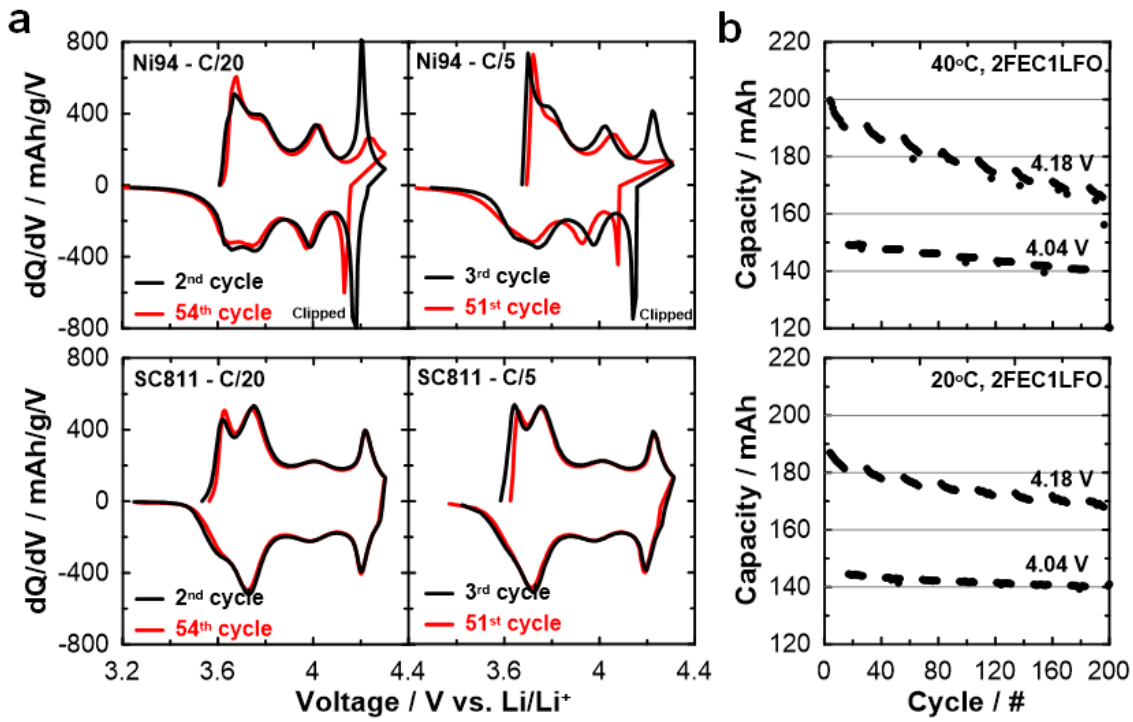

Figure 8.8 (a) The C/20 and C/5 dQ/dV curves of the core-shell Ni94 and the SC811 before and after cycling from 3 to 4.3 V vs. Li/Li$^+$ in coin cell half-cell at 30°C. (b) The capacity vs. cycle number of core-shell Ni94 pouch cells tested with alternating 4.18 V and 4.04 V UCVs at 40°C and 20°C, C/3 CCCV.

8.4 Conclusions

The cycling performances of SC532, SC811 and the washed polycrystalline Co-free core-shell Ni94 material were compared in pouch cells with artificial graphite negative electrodes. Two upper cut-off voltages (UCVs) were carefully chosen for the SC811 and

Ni94 cells based on the dQ/dV curves of the positive electrode material. The lower UCV was chosen to exclude the so-called "H2-H3 phase transition remnant" which is around 4.2 V in the dQ/dV vs. Li/Li^+ curve, whereas the higher UCV was chosen to include this "remnant".

For all five electrolyte blends tested, the SC532 cells showed the best capacity retention with both UCVs and at both temperatures. SC811 cells have lower lifetime than that of SC532 cells but better lifetime than the prototype polycrystalline Co-free core-shell Ni94 at both 20°C and 40°C. The core-shell Ni94 only has excellent life time at 20°C, 4.04 V UCV which is comparable to SC532 and SC811, at least for the first 800 cycles shown in this work with C/3 CCCV charge-discharge cycling.

The Ni94 cells showed poor capacity retention and large impedance growth when operated to 4.18 V (cycling through the "H2-H3 remnant"). However, the performance was dramatically improved, even for this apparently poor material, by limiting the upper cut-off to 4.04 V to avoid the "H2-H3 remnant". This suggests a universal strategy for obtaining the longest cell life time with high Ni-content positive electrode materials. Unless a large discharge capacity is required, limiting the charge cut-off voltage below the "H2-H3 remnant" lowers capacity degradation significantly. Figure 8.8b explored this scenario and showed that capacity loss only occurred during the 4.18 V UCV cycles.

For the core-shell Ni94, the cross-section SEM images on fresh electrodes have shown microcracks due to electrode calendaring. These microcracks are particularly detrimental to cell cycle life as the exposed Ni-rich core is expected to be very reactive with the electrolyte to induce large impedance growth from electrolyte oxidation. Half cell cycling and pouch cell cycling with alternating UCV showed the temporary loss of electric-connection of the active material happens when cycling over the so-called "H2-H3 phase transition remnant" region of the polycrystalline core-shell Ni94 positive electrode material. A large impedance increase is induced at the same time.

Chapter 9 Conclusions and Future Work

9.1 Conclusions

This thesis focused on the development of Co-free Ni-rich layer structured core-shell positive electrode materials as a potential alternative to commercially available Co-containing materials such as SC811. The layer structured Ni-rich materials with core-shell structure, where the Ni-rich core is protected by the lower Ni-content and Mn-containing shell, is expected to have long cycle life without compromising their high specific capacities as discussed in Chapter 2.

Through both electrochemical and physical evaluations of a systematic series of lithiated Co-free Ni-rich core-shell precursors, it was shown that heating temperature of the precursor/lithium hydroxide mixture during synthesis must be carefully selected. Core-shell materials made at insufficient temperature have low specific capacity due to low crystallinity and a high percentage of Ni atoms in the Li layer. Materials made at excessive temperature show interdiffusion between the shell and core compositions leading to poor capacity retention and poor safety performance. Together with the safety performance evaluation, C100_S85_8/0.5 lithiated at 700ºC from Group III and C100_S80_16/1 lithiated at 750ºC from Group IV show the most balanced performance in terms of specific capacity, cycle life and safety among all the materials studied in Table 6.1. The core-shell material C100_S80_16/1 lithiated at 750ºC displayed comparable DCR with NCA and SC811, indicating that Co is not required to attain comparable DCR.

In terms of specific capacity, capacity retention and safety performance, the core-shell materials also present a trade-off relationship similar to that of the homogeneous Ni-rich materials shown in Figure 2.1, which related primarily to the shell thickness and its Mn content. When heating to the same temperature, a core-shell material with more Mn content in the shell will have less specific capacity due to the inactive Mn and more Ni in the lithium layer, but have improved cycling performance with less Ni content exposed to the electrolyte, such as C100_S85_12/0.75 and C100_S80_12/0.75 at 750ºC from Group II, C100_S85_8/0.75 and C100_S80_8/0.75 at 750ºC from Group III, etc. Accelerating

rate calorimetry experiments show that charged core-shell materials with a thick and Mn-rich shell have the least reactivity with electrolyte at elevated temperatures, suggesting such materials will lead to the safest Li-ion cells but at a cost of specific capacity.

The material washing step was found to be detrimental to the core-shell C100_S80_16/1 material heated at 750ºC that deteriorated its electrochemical performance and physical properties. Pouch cell testing showed the cells with washed material performed worse than those with unwashed material at both 20ºC and 40ºC when cycling with both 4.04 and 4.18 V upper cut-off voltages, though the initial rate capabilities of the washed and unwashed core-shell pouch cells were virtually identical. The unwashed material also generated a significantly more gas than its washed version during charge-discharge cycling.

The washed core-shell material was also compared to commercial grade SC811 and SC532. Two upper cut-off voltages per cell type were chosen to either include or exclude the remnant of the "H2-H3 phase transition" region, if present, of each positive electrode material. The core-shell material shows comparable performance to the SC532 and better performance than the SC811 only at 20ºC and 4.04 V upper cut-off voltage. In other testing conditions, the SC532 has the best performance followed by the SC811. For the core-shell material, the particle microcracking from electrode calendaring and material washing also negatively impact its performance. The particle microcracking is particularly detrimental to its cycling performance as the exposed Ni-rich core has a high reactivity with the electrolyte which induces a large impedance increase.

The work in this thesis is unique in a way that the author had the opportunity to design a semi-optimized core-shell material using laboratory-scale methods. Then the exact material designed by the author was scaled to the 10 kg-level and incorporated into pouch-type Li-ion cells by LiFun Technology. One thousand dry pouch cells (no electrolyte) were sent by LiFun Technology to Dalhousie University which allows the author to evaluate his material with different electrolyte blends and make a comparison with other commercial materials in more realistic test vehicles.

9.2 Future work

9.2.1 Explore All Solid-state Synthesis

The core-shell precursor hydroxide used in this thesis was made by co-precipitation method. One of the major drawbacks of this method is the generation of large amount of effluent.[99,184] An all solid state synthesis method can be of great value from both economical and environmental standpoints.

A solid-state synthesis method is analogous to that proposed by L. Zheng et al.[184] The synthesis is expected to carry out in a milling device. The synthesis to make a core-shell oxide can start with nickel oxide particles such as NiO as the "core" phase. Half of the stoichiometric Li may also be milled together with the "core" phase. A pre-mixed nickel oxide and manganese oxide (electrolytic manganese dioxide, for example) with a composition of choice is used as the "shell" phase. Because the "shell" phase particles will act as a coating to the "core" phase particles, it is preferred to have a core particle to be much larger than the shell particle to facilitate the coating process. In addition, the shell phase particles may need to be slowly added to the mill to prevent their accumulation leading to self-agglomeration. Once the coating process is completed, the other half of the Li is added and milled together with the core-shell oxide precursor. This method does not generate any liquid waste nor requires complex synthesis apparatus, therefore is worth for further exploring for making core-shell materials.

9.2.2 Explore More Lithiation Conditions

Minimizing interdiffusion between the core and shell is extremely important to make a core-shell material. The author has explored extensively the impact of heating temperature for core-shell materials. However, heating duration can be equally crucial for the core/shell interdiffusion. Among all the precursors studied in Table 6.1, Group IV materials were lithiated for 20 hours whereas precursors in Group I to III were lithiated for 10 hours. If the heating time were shortened to 10 hours or even 5 hours, some of the Group IV precursors lithiated at 800^{o}C may be able to retain their core-shell structures and achieve improved capacity retentions. Additionally, shortening the synthesis time can increase the production throughput and therefore has economical value. Lithiation in air

can be another parameter to explore. Instead of synthesis in oxygen, lithiation under much cheaper atmosphere such as air allows a cost reduction during large-scale production. It would be therefore worthwhile to examine the performance of these materials lithiated under air atmosphere and compared with those lithiated in oxygen.

9.2.3 Explore Tungsten-coating

In Chapter 8, the author showed that the particle microcracking due to electrode calendaring was detrimental for the core-shell material performance due to the exposed high Ni content core. However, to obtain a high electrode density, high calender pressure is required, resulting in inevitable particle crackings that lower the capacity retention. Very recent work in the Dahn group, performed while the author was writing this thesis, has shown that including WO_3 or ammonium meta tungstate during the heat treatment of the precursor with $LiOH{\bullet}H_2O$ leads to thin layers of amorphous $Li_xW_yO_z$ phases which infuse between the primary particle grains.[185,186] Additionally, the layer of $Li_xW_yO_z$ prevents primary particle growth and greatly hinders interdiffusion between adjacent primary particles. These features of WO_3 lead to potential solutions to improve the core-shell material in pouch cells with high electrode density. Even with cracked particles, the amorphous $Li_xW_yO_z$ surface around primary particles can still prevent the Ni-rich core from exposure to the electrolyte even with high calender pressure. Because of these attractive features, tungsten coated core-shell precursors are promising materials to ultimately outperform the commercial materials such as SC811.

In addition, Divya Rathore in the Dahn group has recently shown that the $Li_xW_yO_z$ phases infused into the grain boundaries prevents the interdiffusion of the core and shell phases in materials like those studied in this thesis (unpublished). This is a very important finding because it opens the door to higher processing temperatures which will speed synthesis without the concern of destroying the core-shell structure. The impact of WO_3 and other similar materials (e.g. ZrO_2, SiO_2) coated on the core-shell precursors in preventing interdiffusion between core and shell need to be carefully and systematically studied.

9.2.4 Symmetric Cell Study on Washed and Unwashed Materials

Pouch cell cycling data of the washed and unwashed material in Chapter 7 shows different degradation behaviors such as those cycling with 4.04 V upper cut-off voltage in Figure 7.5. It is worthwhile to look into the degradation mechanism of these pouch cells more closely. However, since various degradation mechanisms have been associated with almost all its components of a lithium-ion full cell,[80,187–193] it may be difficult to use a pouch cell to unravel the reasons behind cell degradation. Additionally, electrode/electrode interactions are believed to have a strong influence on full cell performance, such as the increase of negative electrode impedance due to the "cross-over" of the dissolved transition metals from the positive electrode,[194–196] and the dramatic increase in positive electrode impedance in the absence of "cross-talk" provided by the graphite negative electrode.[42,197–199] These electrode/electrode interactions further contribute to the complexity of lithium-ion cell degradation studies.

Special electrochemical cells such as those with an embedded reference electrode, to monitor individual electrode voltage and impedance,[196,200,201] and novel electrochemical devices that physically separate each electrode have been used to study electrode/electrode interactions and products, etc.[202–205] However, these approaches are not without drawbacks. Although many are sufficiently reversible and relatively easy to produce, reference electrodes are hard to implement in various cell formats and are highly dependant on their location inside a cell.[206,207] Though novel electrochemical devices are helpful for gaining insights into degradation mechanisms, the major drawback is the limited accessibility for many other researchers and scientists. Therefore, a method with excellent accessibility that simultaneously allows the separate study of individual electrodes and the interactions between them can be highly useful for lithium-ion cell research.

Chen et al.[208] introduced a symmetric cell approach to distinguish the effects of the negative electrode and the positive electrode on the full cell impedance rise. Since a symmetric cell consists of electrolyte and only one type of electrode, one can learn more by doing charge-discharge cycling of symmetric cells. Symmetric cell cycling

performance is dictated by the type of electrode used and its interaction with the selected electrolyte. Many reports have utilized this feature to study various combinations of electrodes and electrolyte,[42,209–212] but the one difficulty of utilizing symmetric cells for cycling lies in the determination of the electrode voltage range vs. Li/Li^+ in a symmetric cell. Unlike in a lithium-ion full cell where the voltage ranges of the positive and negative electrodes are familiar to researchers, each electrode voltage vs. Li/Li^+ in a symmetric cell is not easy to determine and is also closely related to how symmetric cells are constructed. The dV/dQ method[213] can be used to determine the potentials of each electrode vs. Li/Li^+ without introducing a reference electrode. This opens the door for utilizing the symmetric cell method with common coin-cell configurations. By designing a symmetric cell that operates with electrode range identical to that in the pouch cell, a symmetric cell becomes an interesting test vehicle to simplify the study of electrolyte evolution and electrode/electrolyte interphase changes during charge-discharge cycling through cell disassembly.

Positive/positive symmetric cells can be made and cycled with washed and unwashed materials. Cycled symmetric cells can be dissembled to extract the electrodes and electrolyte. The retrieved electrodes and electrolyte can be analyzed by methods such as NMR and XPS to compare the differences in electrolyte and interphase changes between the washed and unwashed materials that tested in the absence of the graphite negative electrodes. The NMR and XPS results from symmetric cells can be further compared with the electrolyte and positive electrodes from the pouch cell with graphite negative electrodes.

9.2.5 Explore Material Washing and Reheating Conditions

Material washing/reheating plays an important role on material performance as shown in Chapter 7. Since the washing/reheating was performed by a commercial vendor, the details of this process were not revealed to the author. It is therefore worthwhile to conduct a series of washing and reheating experiments on the unwashed material simply for better understanding. Some of the washing parameters might include the choice of washing medium such as water or LiOH dissolved in water, the material to water ratio,

washing temperature and flow rate, etc. The quality of washing judged by the leftover surface lithium residual amount after washing can be quantified by acid-base titrations. For heating conditions, the impact of heating under air or oxygen can be explored. The impact of washing and reheating on the material's mechanical property can be further examined quantitively by method developed by Hamam et al.[174] instead of a simple qualitative examination like in Figure 7.1(d).

One thing that can be particularly interesting is the impact of washing/reheating on the core-shell material synthesized at different temperatures, such as C100_S80_16/1 heated at 700ºC, 750ºC, and 800ºC. Core-shell materials can be made when heating this core-shell precursor with a Li/transition metal ratio 1.02 at 700ºC and 750ºC for 20 hours in oxygen, whereas heating at 800ºC gives a homogenous material that is equivalent to $LiNi_{0.935}Mn_{0.065}O_2$. Under the same washing/reheating condition, it will be interesting to see which one of these materials is more resistant to performance degradation both mechanically and electrochemically.

9.2.6 Accelerating Rate Calorimetry Study on Washed and Unwashed Core-shell Materials

Safety performance of the washed and unwashed material will be interesting to explore. To the best of author's knowledge, very few reports have evaluated the impact of surface lithium residuals on accelerating rate calorimetry performance. It will be interesting to study the difference, if any, in safety performance between the washed and unwashed materials.

References

1. H. Budde-Meiwes, J. Drillkens, B. Lunz, J. Muennix, S. Rothgang, J. Kowal, and D. U. Sauer, *Proc. Inst. Mech. Eng. Part D J. Automob. Eng.*, **227**, 761–776 (2013).

2. A. Mahmoudzadeh Andwari, A. Pesiridis, S. Rajoo, R. Martinez-Botas, and V. Esfahanian, *Renew. Sustain. Energy Rev.*, **78**, 414–430 (2017)

3. R. Schmuch, R. Wagner, G. Hörpel, T. Placke, and M. Winter, *Nat. Energy*, **3**, 267–278 (2018)

4. L. Mauler, F. Duffner, W. G. Zeier, and J. Leker, *Energy Environ. Sci.*, **14**, 4712–4739 (2021).

5. L. Mauler, F. Duffner, and J. Leker, *Appl. Energy*, **286**, 116499 (2021)

6. K. Turcheniuk, D. Bondarev, G. G. Amatucci, and G. Yushin, *Mater. Today*, **42**, 57–72 (2021)

7. Y. Kim, W. M. Seong, and A. Manthiram, *Energy Storage Mater.*, **34**, 250–259 (2021)

8. Y. Liu, D. Ouyang, D. Rathore, H. Wu, K. Li, Y. Wang, J. Sha, S. Yin, and J. R. Dahn, *J. Electrochem. Soc.*, **168**, 090555 (2021)

9. H. J. Noh, S. Youn, C. S. Yoon, and Y. K. Sun, *J. Power Sources*, **233**, 121–130 (2013).

10. W. M. Seong, Y. Kim, and A. Manthiram, *Chem. Mater.*, **32**, 9479–9489 (2020).

11. G. J. Ross, J. F. Watts, M. P. Hill, and P. Morrissey, *Polymer (Guildf).*, **41**, 1685–1696 (2000).

12. S. Chen, X. Yang, J. Zhang, J. Ma, Y. Meng, K. Tao, F. Li, and J. Geng, *Electrochim. Acta*, **368**, 137626 (2021)

13. T. Ohzuku and R. J. Brodd, *J. Power Sources*, **174**, 449–456 (2007).

14. W. Liu, P. Oh, X. Liu, M. J. Lee, W. Cho, S. Chae, Y. Kim, and J. Cho, *Angew. Chemie - Int. Ed.*, **54**, 4440–4457 (2015).

15. J. B. Goodenough and Y. Kim, *J. Power Sources*, **196**, 6688–6694 (2011)

16. J. Zheng, W. H. Kan, and A. Manthiram, *ACS Appl. Mater. Interfaces*, **7**, 6926–6934 (2015).

17. Y. Liu, H. Wu, K. Li, H. Li, D. Ouyang, P. P. Arab, N. Phattharasupakun, D. Rathore, M. Johnson, Y. Wang, S. Yin, and J. R. Dahn, *J. Electrochem. Soc.*, **167**, 120533 (2020).

18. J. Li, L. E. Downie, L. Ma, W. Qiu, and J. R. Dahn, *J. Electrochem. Soc.*, **162**, A1401–A1408 (2015)

19. Z. Chen and J. R. Dahn, *Electrochim. Acta*, **49**, 1079–1090 (2004).

20. M. S. Whittingham, *Chem. Rev.*, **104**, 4271–4301 (2004).

21. J. N. Reimers and J. R. Dahn, *J. Electrochem. Soc.*, **139**, 2091–2097 (1992).

22. R. M. Goody, *Proc. R. Soc. London. Ser. A. Math. Phys. Sci.*, **209**, 196–218 (1951).

23. T. Zheng, J. N. Reimers, and J. R. Dahn, *Phys. Rev. B*, **51**, 734–741 (1995).

24. K. Xu, *Chem. Rev.*, **114**, 11503–11618 (2014).

25. K. Xu, *Chem. Rev.*, **104**, 4303–4417 (2004).

26. M. S. Ding, K. Xu, S. S. Zhang, K. Amine, G. L. Henriksen, and T. R. Jow, *J. Electrochem. Soc.*, **148**, A1196 (2001).

27. S. Wiemers-Meyer, S. Jeremias, M. Winter, and S. Nowak, *Electrochim. Acta*, **222**, 1267–1271 (2016)

28. S. S. Zhang, K. Xu, and T. R. Jow, *J. Electrochem. Soc.*, **149**, A586 (2002).

29. K. Xu, S. Zhang, T. R. Jow, W. Xu, and C. A. Angell, *Electrochem. Solid-State Lett.*, **5**, 0–4 (2002).

30. M. Marzantowicz, J. R. Dygas, F. Krok, J. L. Nowiński, A. Tomaszewska, Z. Florjańczyk, and E. Zygadło-Monikowska, *J. Power Sources*, **159**, 420–430 (2006).

31. M. Dahbi, F. Ghamouss, F. Tran-Van, D. Lemordant, and M. Anouti, *J. Power Sources*, **196**, 9743–9750 (2011).

32. D. S. Hall, A. Eldesoky, E. R. Logan, E. M. Tonita, X. Ma, and J. R. Dahn, *J. Electrochem. Soc.*, **165**, A2365–A2373 (2018).

33. J. Li, H. Li, X. Ma, W. Stone, S. Glazier, E. Logan, E. M. Tonita, K. L. Gering, and J. R. Dahn, *J. Electrochem. Soc.*, **165**, A1027–A1037 (2018).

34. S. Herreyre, O. Huchet, S. Barusseau, F. Perton, J. M. Bodet, and P. Biensan, *J. Power Sources*, **97**–**98**, 576–580 (2001).

35. M. C. Smart, B. V. Ratnakumar, K. B. Chin, and L. D. Whitcanack, *J. Electrochem. Soc.*, **157**, A1361 (2010).

36. S. K. Heiskanen, J. Kim, and B. L. Lucht, *Joule*, **3**, 2322–2333 (2019)

37. K. Edström, M. Herstedt, and D. P. Abraham, *J. Power Sources*, **153**, 380–384 (2006).

38. P. Verma, P. Maire, and P. Novák, *Electrochim. Acta*, **55**, 6332–6341 (2010)

39. J. B. Goodenough and K. S. Park, *J. Am. Chem. Soc.*, **135**, 1167–1176 (2013).

40. J. B. Goodenough and Y. Kim, *Chem. Mater.*, **22**, 587–603 (2010).

41. Y. Liu, L. Ma, and J. R. Dahn, *J. Electrochem. Soc.*, **168**, 080537 (2021)

42. Y. Liu, I. Hamam, and J. R. Dahn, *J. Electrochem. Soc.*, **167**, 110527 (2020).

43. J. Li, H. Li, W. Stone, S. Glazier, and J. R. Dahn, *J. Electrochem. Soc.*, **165**, A626–A635 (2018).

44. D. Y. Wang, J. Xia, L. Ma, K. J. Nelson, J. E. Harlow, D. J. Xiong, L. E. Downie, R. Petibon, J. C. Burns, A. Xiao, W. M. Lamanna, and J. R. Dahn, *J. Electrochem. Soc.*, **161**, A1818–A1827 (2014).

45. W. Song, J. Harlow, E. Logan, H. Hebecker, M. Coon, L. Molino, M. Johnson, J. Dahn, and M. Metzger, *J. Electrochem. Soc.*, **168**, 090503 (2021)

46. S. T. Myung, F. Maglia, K. J. Park, C. S. Yoon, P. Lamp, S. J. Kim, and Y. K. Sun, *ACS Energy Lett.*, **2**, 196–223 (2017).

47. A. Aishova, G. T. Park, C. S. Yoon, and Y. K. Sun, *Adv. Energy Mater.*, **10**, 1–9 (2020).

48. K.-K. Lee and K.-B. Kim, *J. Electrochem. Soc.*, **147**, 1709 (2000).

49. S. Albrecht, J. Kümpers, M. Kruft, S. Malcus, C. Vogler, M. Wahl, and M. Wohlfahrt-Mehrens, *J. Power Sources*, **119**–**121**, 178–183 (2003).

50. J. Xu, F. Lin, M. M. Doeff, and W. Tong, *J. Mater. Chem. A*, **5**, 874–901 (2017).

51. S. W. D. Gourley, T. Or, and Z. Chen, *iScience*, **23**, 101505 (2020)

52. Q. Xie, W. Li, and A. Manthiram, *Chem. Mater.*, **31**, 938–946 (2019).

53. W. Li, X. Liu, H. Celio, P. Smith, A. Dolocan, M. Chi, and A. Manthiram, *Adv. Energy Mater.*, **8**, 1–11 (2018).

54. W. Li, S. Lee, and A. Manthiram, *Adv. Mater.*, **32**, 1–6 (2020).

55. Z. Cui, Q. Xie, and A. Manthiram, *ACS Appl. Mater. Interfaces*, **13**, 15324–15332 (2021).

56. U. H. Kim, N. Y. Park, G. T. Park, H. Kim, C. S. Yoon, and Y. K. Sun, *Energy Storage Mater.*, **33**, 399–407 (2020).

57. H. Li, M. Cormier, N. Zhang, J. Inglis, J. Li, and J. R. Dahn, *J. Electrochem. Soc.*, **166**, A429–A439 (2019).

58. D. Jugović and D. Uskoković, *J. Power Sources*, **190**, 538–544 (2009).

59. T. V. S. L. Satyavani, A. Srinivas Kumar, and P. S. V. Subba Rao, *Eng. Sci. Technol. an Int. J.*, **19**, 178–188 (2016)

60. Z. Yang, Y. Dai, S. Wang, and J. Yu, *J. Mater. Chem. A*, **4**, 18210–18222 (2016).

61. H. Li, N. Zhang, J. Li, and J. R. Dahn, *J. Electrochem. Soc.*, **165**, A2985–A2993 (2018).

62. K. Liu, Y. Liu, D. Lin, A. Pei, and Y. Cui, *Sci. Adv.*, **4** (2018).

63. H. Li, A. Liu, N. Zhang, Y. Wang, S. Yin, H. Wu, and J. R. Dahn, *Chem. Mater.*, **31**, 7574–7583 (2019).

64. R. Jung, M. Metzger, F. Maglia, C. Stinner, and H. A. Gasteiger, *J. Phys. Chem. Lett.*, **8**, 4820–4825 (2017).

65. L. Ma, S. Young, L. D. Ellis, Q. Huang, X. Ma, M. Chatzidakis, H. Li, L. Thompson, A. Eldesoky, C. R. M. McFarlane, G. A. Botton, I. G. Hill, and J. R. Dahn, *ACS Appl. Energy Mater.*, **1**, 7052–7064 (2018).

66. L. Giordano, P. Karayaylali, Y. Yu, Y. Katayama, F. Maglia, S. Lux, and Y. Shao-Horn, *J. Phys. Chem. Lett.*, **8**, 3881–3887 (2017).

67. J. Li, H. Liu, J. Xia, A. R. Cameron, M. Nie, G. A. Botton, and J. R. Dahn, *J. Electrochem. Soc.*, **164**, A655–A665 (2017).

68. F. Lin, I. M. Markus, D. Nordlund, T.-C. Weng, M. D. Asta, H. L. Xin, and M. M. Doeff, *Nat. Commun.*, **5**, 1–9 (2014)

69. S. Watanabe, M. Kinoshita, T. Hosokawa, K. Morigaki, and K. Nakura, *J. Power Sources*, **260**, 50–56 (2014).

70. H. Liu, M. Wolf, K. Karki, Y. S. Yu, E. A. Stach, J. Cabana, K. W. Chapman, and P. J. Chupas, *Nano Lett.*, **17**, 3452–3457 (2017).

71. K.-J. Park, J.-Y. Hwang, H.-H. Ryu, F. Maglia, S.-J. Kim, P. Lamp, C. S. Yoon, and Y.-K. Sun, *ACS Energy Lett.*, **4**, 1394–1400 (2019)

72. H. H. Ryu, K. J. Park, C. S. Yoon, and Y. K. Sun, *Chem. Mater.*, **30**, 1155–1163 (2018).

73. Y. Makimura, S. Zheng, Y. Ikuhara, and Y. Ukyo, *J. Electrochem. Soc.*, **159**, 1070–1073 (2012).

74. U. H. Kim, D. W. Jun, K. J. Park, Q. Zhang, P. Kaghazchi, D. Aurbach, D. T. Major, G. Goobes, M. Dixit, N. Leifer, C. M. Wang, P. Yan, D. Ahn, K. H. Kim, C. S. Yoon, and Y. K. Sun, *Energy Environ. Sci.*, **11**, 1271–1279 (2018).

75. H. H. Sun and A. Manthiram, *Chem. Mater.*, **29**, 8486–8493 (2017).

76. J.-H. Kim, H.-H. Ryu, S. J. Kim, C. S. Yoon, and Y.-K. Sun, *ACS Appl. Mater. Interfaces*, **11**, 30936–30942 (2019).

77. D. J. Miller, C. Proff, J. G. Wen, D. P. Abraham, and J. Bareño, *Adv. Energy Mater.*, **3**, 1098–1103 (2013).

78. P. Yan, J. Zheng, M. Gu, J. Xiao, J.-G. Zhang, and C.-M. Wang, *Nat. Commun.*, **8**, 14101 (2017).

79. H. Kim, M. G. Kim, H. Y. Jeong, H. Nam, and J. Cho, *Nano Lett.*, **15**, 2111–2119 (2015).

80. Y. Liu, J. Harlow, and J. Dahn, *J. Electrochem. Soc.*, **167**, 020512 (2020).

81. S. Liu, H. Wu, L. Huang, M. Xiang, H. Liu, and Y. Zhang, *J. Alloys Compd.*, **674**, 447–454 (2016)

82. D. Mohanty, K. Dahlberg, D. M. King, L. A. David, A. S. Sefat, D. L. Wood, C. Daniel, S. Dhar, V. Mahajan, M. Lee, and F. Albano, *Sci. Rep.*, **6**, 1–16 (2016)

83. S. T. Myung, K. Izumi, S. Komaba, Y. K. Sun, H. Yashiro, and N. Kumagai, *Chem. Mater.*, **17**, 3695–3704 (2005).

84. N. Zhang, N. Zaker, H. Li, A. Liu, J. Inglis, L. Jing, J. Li, Y. Li, G. A. Botton, and J. R. Dahn, *Chem. Mater.*, **31**, 10150–10160 (2019).

85. S. T. Myung, K. S. Lee, D. W. Kim, B. Scrosati, and Y. K. Sun, *Energy Environ. Sci.*, **4**, 935–939 (2011).

86. B. C. Park, H. J. Bang, K. Amine, E. Jung, and Y. K. Sun, *J. Power Sources*, **174**, 658–662 (2007).

87. A. Manthiram, J. C. Knight, S. T. Myung, S. M. Oh, and Y. K. Sun, *Adv. Energy Mater.*, **6** (2016).

88. R. L. Patel, Y. B. Jiang, A. Choudhury, and X. Liang, *Sci. Rep.*, **6**, 1–11 (2016).

89. H.-H. Sun, H.-H. Ryu, U.-H. Kim, J. A. Weeks, A. Heller, Y.-K. Sun, and C. B. Mullins, *ACS Energy Lett.* (2020)

90. Z. Chen, Y. Qin, K. Amine, and Y. K. Sun, *J. Mater. Chem.*, **20**, 7606–7612 (2010).

91. D. W. Jun, C. S. Yoon, U. H. Kim, and Y. K. Sun, *Chem. Mater.*, **29**, 5048–5052 (2017).

92. J. Li, R. Doig, J. Camardese, K. Plucknett, and J. R. Dahn, *Chem. Mater.*, **27**, 7765–7773 (2015).

93. F. Zhou, X. Zhao, A. Van Bommel, A. W. Rowe, and J. R. Dahn, *Chem. Mater.*, **22**, 1015–1021 (2010).

94. W. Luo and J. R. Dahn, *Chem. Mater.*, **21**, 56–62 (2009).

95. Y. Kim and D. Kim, *ACS Appl. Mater. Interfaces*, **4**, 586–589 (2012).

96. A. Liu, N. Zhang, J. Li, T. Casagrande, C. Butcher, J. Martinez, A. Korinek, G. Botton, and J. R. Dahn, *J. Electrochem. Soc.*, **165**, A2781–A2791 (2018).

97. H. Li, J. Li, N. Zaker, N. Zhang, G. A. Botton, and J. R. Dahn, *J. Electrochem. Soc.*, **166**, A1956–A1963 (2019).

98. J. Li, N. Zhang, H. Li, A. Liu, Y. Wang, S. Yin, H. Wu, and J. R. Dahn, *J. Electrochem. Soc.*, **165**, A3544–A3557 (2018).

99. S. Ahmed, P. A. Nelson, K. G. Gallagher, N. Susarla, and D. W. Dees, *J. Power Sources*, **342**, 733–740 (2017)

100. N. Phattharasupakun, M. M. E. Cormier, E. Lyle, E. Zsoldos, A. Liu, C. Geng, Y. Liu, H. Li, M. Sawangphruk, and J. R. Dahn, *J. Electrochem. Soc.*, **168**, 090535 (2021)

101. S. E. Renfrew and B. D. McCloskey, *J. Am. Chem. Soc.*, **139**, 17853–17860 (2017).

102. L. A. Kaufman and B. D. McCloskey, *Chem. Mater.*, **33**, 4170–4176 (2021).

103. Y. Kim, *J. Solid State Electrochem.*, **17**, 1961–1965 (2013).

104. Y. Kim, H. Park, A. Dolocan, J. H. Warner, and A. Manthiram, *ACS Appl. Mater. Interfaces*, **13**, 27096–27105 (2021).

105. Y. Kim, H. Park, J. H. Warner, and A. Manthiram, *ACS Energy Lett.*, **6**, 941–948 (2021).

106. J. Kim, H. Lee, H. Cha, M. Yoon, M. Park, and J. Cho, *Adv. Energy Mater.*, **8**, 1–25 (2018).

107. X. Xiong, Z. Wang, P. Yue, H. Guo, F. Wu, J. Wang, and X. Li, *J. Power Sources*, **222**, 318–325 (2013)

108. K. Park and B. Choi, *J. Alloys Compd.*, **766**, 470–476 (2018)

109. X. Huang, J. Duan, J. He, H. Shi, Y. Li, Y. Zhang, D. Wang, and P. Dong, *Mater. Today Energy*, **17** (2020).

110. I. Hamam, N. Zhang, A. Liu, M. B. Johnson, and J. R. Dahn, *J. Electrochem. Soc.*, **167**, 130521 (2020).

111. D. Pritzl, T. Teufl, A. T. S. Freiberg, B. Strehle, J. Sicklinger, H. Sommer, P. Hartmann, and H. A. Gasteiger, *J. Electrochem. Soc.*, **166**, A4056–A4066 (2019).

112. Y. Bi, T. Wang, M. Liu, R. Du, W. Yang, Z. Liu, Z. Peng, Y. Liu, D. Wang, and X. Sun, *RSC Adv.*, **6**, 19233–19237 (2016).

113. W. Wang, L. Wu, Z. Li, K. Huang, Z. Chen, C. Lv, H. Dou, and X. Zhang, *ChemElectroChem*, **8**, 2014–2021 (2021).

114. S. Chen, T. He, Y. Su, Y. Lu, L. Bao, L. Chen, Q. Zhang, J. Wang, R. Chen, and F. Wu, *ACS Appl. Mater. Interfaces*, **9**, 29732–29743 (2017).

115. Y. You, H. Celio, J. Li, A. Dolocan, and A. Manthiram, *Angew. Chemie*, **130**, 6590–6595 (2018).

116. X. Bai, W. Li, W. Zhuang, S. Lu, and Z. Su, *Solid State Ionics*, **355**, 115418 (2020)

117. A. L. Michan, B. S. Parimalam, M. Leskes, R. N. Kerber, T. Yoon, C. P. Grey, and B. L. Lucht, *Chem. Mater.*, **28**, 8149–8159 (2016).

118. X. Ma, R. S. Young, L. D. Ellis, L. Ma, J. Li, and J. R. Dahn, *J. Electrochem. Soc.*, **166**, A2665–A2672 (2019).

119. L. Ma, L. Ellis, S. L. Glazier, X. Ma, Q. Liu, J. Li, and J. R. Dahn, *J. Electrochem. Soc.*, **165**, A891–A899 (2018).

120. L. Ma, L. Ellis, S. L. Glazier, X. Ma, and J. R. Dahn, *J. Electrochem. Soc.*, **165**, A1718–A1724 (2018).

121. W. Zhao, Y. Ji, Z. Zhang, M. Lin, Z. Wu, X. Zheng, Q. Li, and Y. Yang, *Curr. Opin. Electrochem.* (2017)

122. I. A. Shkrob, J. F. Wishart, and D. P. Abraham, *J. Phys. Chem. C*, **119**, 14954–14964 (2015).

123. D. Aurbach, K. Gamolsky, B. Markovsky, Y. Gofer, M. Schmidt, and U. Heider, *Electrochim. Acta*, **47**, 1423–1439 (2002).

124. L. El Ouatani, R. Dedryvère, C. Siret, P. Biensan, S. Reynaud, P. Iratçabal, and D. Gonbeau, *J. Electrochem. Soc.*, **156**, A103 (2009)

125. D. Xiong, J. C. Burns, A. J. Smith, N. Sinha, and J. R. Dahn, *J. Electrochem. Soc.*, **158**, A1431 (2011)

126. J. C. Burns, R. Petibon, K. J. Nelson, N. N. Sinha, A. Kassam, B. M. Way, and J. R. Dahn, *J. Electrochem. Soc.*, **160**, A1668–A1674 (2013)

127. P. Jankowski, N. Lindahl, J. Weidow, W. Wieczorek, and P. Johansson, *ACS Appl. Energy Mater.*, **1**, 2582–2591 (2018).

128. B. Tong, Z. Song, H. Wan, W. Feng, M. Armand, J. Liu, H. Zhang, and Z. Zhou, *InfoMat*, 1–29 (2021).

129. A. Sano and S. Maruyama, *J. Power Sources*, **192**, 714–718 (2009).

130. J. Xia, R. Petibon, N. N. Sinha, and J. R. Dahn, *J. Electrochem. Soc.*, **162**, A2227–A2235 (2015).

131. J. Xia, N. N. Sinha, L. P. Chen, and J. R. Dahn, *J. Electrochem. Soc.*, **161**, A264–A274 (2014).

132. C. Wang, Y. S. Meng, and K. Xu, *J. Electrochem. Soc.*, **166**, A5184–A5186 (2019).

133. R. McMillan, H. Slegr, Z. X. Shu, and W. Wang, *J. Power Sources*, **81**–**82**, 20–26 (1999).

134. C. Xu, F. Lindgren, B. Philippe, M. Gorgoi, F. Björefors, K. Edström, and T. Gustafsson, *Chem. Mater.*, **27**, 2591–2599 (2015).

135. H. Bin Son, M. Y. Jeong, J. G. Han, K. Kim, K. H. Kim, K. M. Jeong, and N. S. Choi, *J. Power Sources*, **400**, 147–156 (2018)

136. I. A. Profatilova, S. S. Kim, and N. S. Choi, *Electrochim. Acta*, **54**, 4445–4450 (2009).

137. D. Liu, K. Qian, Y. B. He, D. Luo, H. Li, M. Wu, F. Kang, and B. Li, *Electrochim. Acta*, **269**, 378–387 (2018)

138. E. Markevich, G. Salitra, K. Fridman, R. Sharabi, G. Gershinsky, A. Garsuch, G. Semrau, M. A. Schmidt, and D. Aurbach, (2014).

139. Y. Kang, J. Wang, M. Wang, X. Tang, Z. Cao, C. Wang, Q. Shi, Y. Qian, and Y. Deng, *ACS Appl. Energy Mater.*, **3**, 9989–10000 (2020).

140. G. Yang, J. Shi, C. Shen, S. Wang, L. Xia, H. Hu, H. Luo, Y. Xia, and Z. Liu, *RSC Adv.*, **7**, 26052–26059 (2017).

141. J. Chen, L. Xing, X. Yang, X. Liu, T. Li, and W. Li, *Electrochim. Acta*, **290**, 568–576 (2018)

142. J. C. Burns, N. N. Sinha, G. Jain, H. Ye, C. M. VanElzen, E. Scott, A. Xiao, W. M. Lamanna, and J. R. Dahn, *J. Electrochem. Soc.*, **160**, A2281–A2287 (2013).

143. C. Wang, L. Yu, W. Fan, J. Liu, L. Ouyang, L. Yang, and M. Zhu, *ACS Appl. Energy Mater.*, **1**, 2647–2656 (2018).

144. P. Hou, X. Wang, D. Song, X. Shi, L. Zhang, J. Guo, and J. Zhang, *J. Power Sources*, **265**, 174–181 (2014)

145. P. Hou, H. Zhang, Z. Zi, L. Zhang, and X. Xu, *J. Mater. Chem. A*, **5**, 4254–4279 (2017).

146. J. Camardese, J. Li, D. W. Abarbanel, A. T. B. Wright, and J. R. Dahn, *J. Electrochem. Soc.*, **162**, A269–A277 (2015).

147. J. Li, J. Camardese, R. Shunmugasundaram, S. Glazier, Z. Lu, and J. R. Dahn, *Chem. Mater.*, **27**, 3366–3377 (2015).

148. Y. Liu, H. Wu, Y. Wang, K. Li, S. Yin, and J. R. Dahn, *J. Electrochem. Soc.*, **167**, 160556 (2021).

149. S. R. Cullity, B.D.;Stock, *Elements of X-ray Diffraction, Third Edition*, Prentice-Hall, New York, (2001).

150. D. Kriegner, Z. Matěj, R. Kužel, and V. Holý, *J. Appl. Crystallogr.*, **48**, 613–618 (2015).

151. C. J. Hunter, B. A.; Hunger, *Aust. Nucl. Sci. Technol. X Ray Neutron LHPM, a Comput. Progr. Rietveld Anal. X-ray Neutron Powder Diffr. Patterns* (1998).

152. W. I. F. David, *J. Res. Natl. Inst. Stand. Technol.*, **109**, 107–123 (2004).

153. B. H. Toby, *Powder Diffr.*, **21**, 67–70 (2006).

154. A. Ul-Hamid, *A Beginners' Guide to Scanning Electron Microscopy*, (2018).

155. J. I. Goldstein, D. E. Newbury, J. R. Michael, N. W. M. Ritchie, J. H. J. Scott, and D. C. Joy, *Scanning electron microscopy and x-ray microanalysis*, p. 1–550, (2017).

156. D. D. MacNeil and J. R. Dahn, *J. Electrochem. Soc.*, **148**, A1205 (2001).

157. L. Ma, M. Nie, J. Xia, and J. R. Dahn, *J. Power Sources*, **327**, 145–150 (2016)

158. D. Ouyang, Y. Liu, I. Hamam, J. Wang, and J. Dahn, *J. Energy Chem.*, **60**, 523–530 (2021)

159. J. E. Harlow, X. Ma, J. Li, E. Logan, Y. Liu, N. Zhang, L. Ma, S. L. Glazier, M. M. E. Cormier, M. Genovese, S. Buteau, A. Cameron, J. E. Stark, and J. R. Dahn, *J. Electrochem. Soc.*, **166**, A3031–A3044 (2019).

160. C. P. Aiken, J. Xia, D. Y. Wang, D. A. Stevens, S. Trussler, and J. R. Dahn, *J. Electrochem. Soc.*, **161**, A1548–A1554 (2014).

161. R. D. Shannon, *Acta Crystallogr. Sect. A Cryst. physics, diffraction, Theor. Gen. Crystallogr.*, **32**, 751–767 (1976).

162. L. de Biasi, A. Schiele, M. Roca-Ayats, G. Garcia, T. Brezesinski, P. Hartmann, and J. Janek, *ChemSusChem*, **12**, 2240–2250 (2019).

163. Y. Kobayashi, M. Tabuchi, H. Miyashiro, and N. Kuriyama, *J. Power Sources*, **364**, 156–162 (2017)

164. J. R. Mueller-Neuhaus, R. A. Dunlap, and J. R. Dahn, *J. Electrochem. Soc.*, **147**, 3598 (2000)

165. J. Li, R. Shunmugasundaram, R. Doig, and J. R. Dahn, *Chem. Mater.*, **28**, 162–171 (2016).

166. H. Li, J. Li, X. Ma, and J. R. Dahn, *J. Electrochem. Soc.*, **165**, A1038–A1045 (2018)

167. J. Li, H. Li, W. Stone, R. Weber, S. Hy, and J. R. Dahn, *J. Electrochem. Soc.*, **164**, A3529–A3537 (2017)

168. E. McCalla, A. W. Rowe, R. Shunmugasundaram, and J. R. Dahn, *Chem. Mater.*, **25**, 989–999 (2013).

169. X. Ma, J. E. Harlow, J. Li, L. Ma, D. S. Hall, S. Buteau, M. Genovese, M. Cormier, and J. R. Dahn, *J. Electrochem. Soc.*, **166**, A711–A724 (2019).

170. Y.-K. Sun, H.-J. Noh, and C. S. Yoon, *J. Electrochem. Soc.*, **159**, A1–A5 (2011).

171. Y. Jiang, Z. Liu, Y. Zhang, H. Hu, X. Teng, D. Wang, P. Gao, and Y. Zhu, *Electrochim. Acta*, **309**, 74–85 (2019)

172. K. J. Kreder and A. Manthiram, *ACS Energy Lett.*, **2**, 64–69 (2017).

173. S. Pajot, P. Feydi, F. Weill, M. Ménétrier, G. Yildirim, L. Simonin, and L. Croguennec, *J. Electrochem. Soc.*, **165**, A425–A433 (2018).

174. I. Hamam, R. Omessi, D. Rathore, C. Geng, R. Cooke, K. Plucknett, D. P. Bishop, N. Zaker, G. A. Botton, C. Yang, and J. R. Dahn, *Cell Reports Phys. Sci.*, 100714 (2022)

175. P. Lu, C. Li, E. W. Schneider, and S. J. Harris, *J. Phys. Chem. C*, **118**, 896–903 (2014).

176. Q. Q. Liu, R. Petibon, C. Y. Du, and J. R. Dahn, *J. Electrochem. Soc.*, **164**, A1173–A1183 (2017).

177. Y. Preger, H. M. Barkholtz, A. Fresquez, D. L. Campbell, B. W. Juba, J. Romàn-Kustas, S. R. Ferreira, and B. Chalamala, *J. Electrochem. Soc.*, **167**, 120532 (2020).

178. S. S. Choi and H. S. Lim, *J. Power Sources*, **111**, 130–136 (2002).

179. A. Liu, N. Phattharasupakun, M. M. E. Cormier, E. Zsoldos, N. Zhang, E. Lyle, P. Arab, M. Sawangphruk, and J. R. Dahn, *J. Electrochem. Soc.*, **168**, 070503 (2021)

180. N. Phattharasupakun, M. M. E. Cormier, C. Geng, M. Sawangphruk, and J. R. Dahn, *J. Electrochem. Soc.*, **168**, 090564 (2021)

181. H. M. Dahn, A. J. Smith, J. C. Burns, D. A. Stevens, and J. R. Dahn, *J. Electrochem. Soc.*, **159**, A1405–A1409 (2012).

182. R. Jung, M. Metzger, F. Maglia, C. Stinner, and H. A. Gasteiger, *J. Electrochem. Soc.*, **164**, A1361–A1377 (2017).

183. S. Watanabe, M. Kinoshita, T. Hosokawa, K. Morigaki, and K. Nakura, *J. Power Sources*, **258**, 210–217 (2014).

184. L. Zheng, J. C. Bennett, and M. N. Obrovac, *J. Electrochem. Soc.*, **167**, 130536 (2020).

185. C. Geng, D. Rathore, D. Heino, N. Zhang, I. Hamam, N. Zaker, G. A. Botton, R. Omessi, N. Phattharasupakun, T. Bond, C. Yang, and J. R. Dahn, *Adv. Energy Mater.*, **2103067**, 2103067 (2021).

186. D. Rathore, C. Geng, N. Zaker, I. Hamam, Y. Liu, P. Xiao, G. A. Botton, J. Dahn, and C. Yang, *J. Electrochem. Soc.*, **168**, 120514 (2021).

187. X. Zhang, J. Zhu, and E. Sahraei, *RSC Adv.*, **7**, 56099–56107 (2017).

188. S. T. Myung, Y. Hitoshi, and Y. K. Sun, *J. Mater. Chem.*, **21**, 9891–9911 (2011).

189. A. M. Grillet, T. Humplik, E. K. Stirrup, S. A. Roberts, D. A. Barringer, C. M. Snyder, M. R. Janvrin, and C. A. Apblett, *J. Electrochem. Soc.*, **163**, A1859–A1871 (2016).

190. H. Haruna, S. Takahashi, and Y. Tanaka, *J. Electrochem. Soc.*, **164**, A6278–A6280 (2017).

191. R. Weber, M. Genovese, A. J. Louli, S. Hames, C. Martin, I. G. Hill, and J. R. Dahn, *Nat. Energy*, **4**, 683–689 (2019)

192. M. N. Obrovac and L. Christensen, *Electrochem. Solid-State Lett.*, **7** (2004).

193. J. Sieg, M. Storch, J. Fath, A. Nuhic, J. Bandlow, B. Spier, and D. U. Sauer, *J. Energy Storage*, **30**, 101582 (2020)

194. A. Eldesoky, E. R. Logan, M. B. Johnson, C. R. M. McFarlane, and J. R. Dahn, *J. Electrochem. Soc.*, **167**, 130539 (2020).

195. N. P. W. Pieczonka, Z. Liu, P. Lu, K. L. Olson, J. Moote, B. R. Powell, and J. H. Kim, *J. Phys. Chem. C*, **117**, 15947–15957 (2013).

196. N. V. Faenza, Z. W. Lebens-Higgins, P. Mukherjee, S. Sallis, N. Pereira, F. Badway, A. Halajko, G. Ceder, F. Cosandey, L. F. J. Piper, and G. G. Amatucci, *Langmuir*, **33**, 9333–9353 (2017).

197. D. J. Xiong, L. D. Ellis, R. Petibon, T. Hynes, Q. Q. Liu, and J. R. Dahn, *J. Electrochem. Soc.*, **164**, A340–A347 (2017).

198. M.-T. F. Rodrigues, K. Kalaga, S. E. Trask, I. A. Shkrob, and D. P. Abraham, *J. Electrochem. Soc.*, **165**, A1697–A1705 (2018).

199. C. Mao, R. E. Ruther, L. Geng, Z. Li, D. N. Leonard, H. M. Meyer, R. L. Sacci, and D. L. Wood, *ACS Appl. Mater. Interfaces*, **11**, 43235–43243 (2019).

200. J. A. Gilbert, I. A. Shkrob, and D. P. Abraham, *J. Electrochem. Soc.*, **164**, A389–A399 (2017).

201. S. Solchenbach, D. Pritzl, E. J. Y. Kong, J. Landesfeind, and H. A. Gasteiger, *J. Electrochem. Soc.*, **163**, A2265–A2272 (2016).

202. B. Aktekin, M. J. Lacey, T. Nordh, R. Younesi, C. Tengstedt, W. Zipprich, D. Brandell, and K. Edström, *J. Phys. Chem. C*, **122**, 11234–11248 (2018).

203. R. Sahore, F. Dogan, and I. D. Bloom, *Chem. Mater.*, **31**, 2884–2891 (2019).

204. N. R. Vadivel, S. Ha, M. He, D. Dees, S. Trask, B. Polzin, and K. G. Gallagher, *J. Electrochem. Soc.*, **164**, A508–A517 (2017).

205. M. Metzger, B. Strehle, S. Solchenbach, and H. A. Gasteiger, *J. Electrochem. Soc.*, **163**, A798–A809 (2016).

206. G. Hsieh, T. O. Mason, E. J. Garboczi, and L. R. Pederson, *Solid State Ionics*, **96**, 153–172 (1997).

207. Y. Hoshi, Y. Narita, K. Honda, T. Ohtaki, I. Shitanda, and M. Itagaki, *J. Power Sources*, **288**, 168–175 (2015)

208. C. H. Chen, J. Liu, and K. Amine, *Electrochem. commun.*, **3**, 44–47 (2001).

209. L. S. Plashnitsa, E. Kobayashi, S. Okada, and J. I. Yamaki, *Electrochim. Acta*, **56**, 1344–1351 (2011)

210. D. Applestone and A. Manthiram, *J. Power Sources*, **217**, 1–5 (2012)

211. P. Ping, Q. S. Wang, J. H. Sun, X. Xia, and J. R. Dahn, *J. Electrochem. Soc.*, **159**, A1467–A1473 (2012).

212. C. Shen, D. Xiong, L. D. Ellis, K. L. Gering, L. Huang, and J. R. Dahn, *J. Electrochem. Soc.*, **164**, A3349–A3356 (2017).

213. H. M. Dahn, A. J. Smith, J. C. Burns, D. A. Stevens, and J. R. Dahn, *J. Electrochem. Soc.*, **159**, 0–4 (2012).

Appendix A

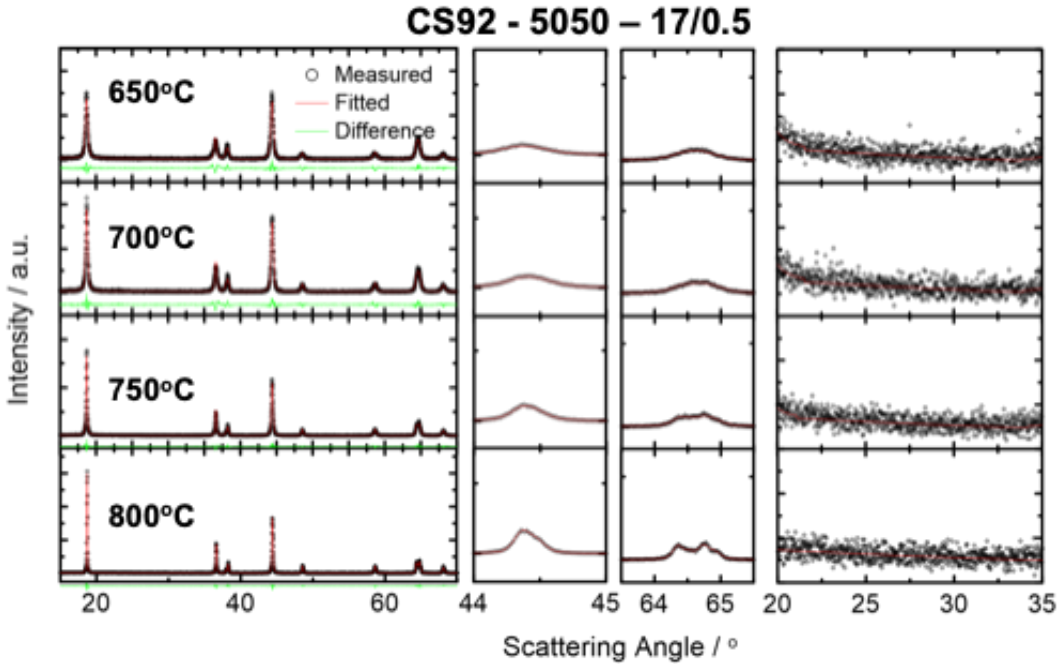
CS92 - 5050 – 17/0.5
650°C
700°C
750°C
800°C
Measured
Fitted
Difference
Intensity / a.u.
20
40
60
44
45
64
65
20
25
30
35
Scattering Angle / °

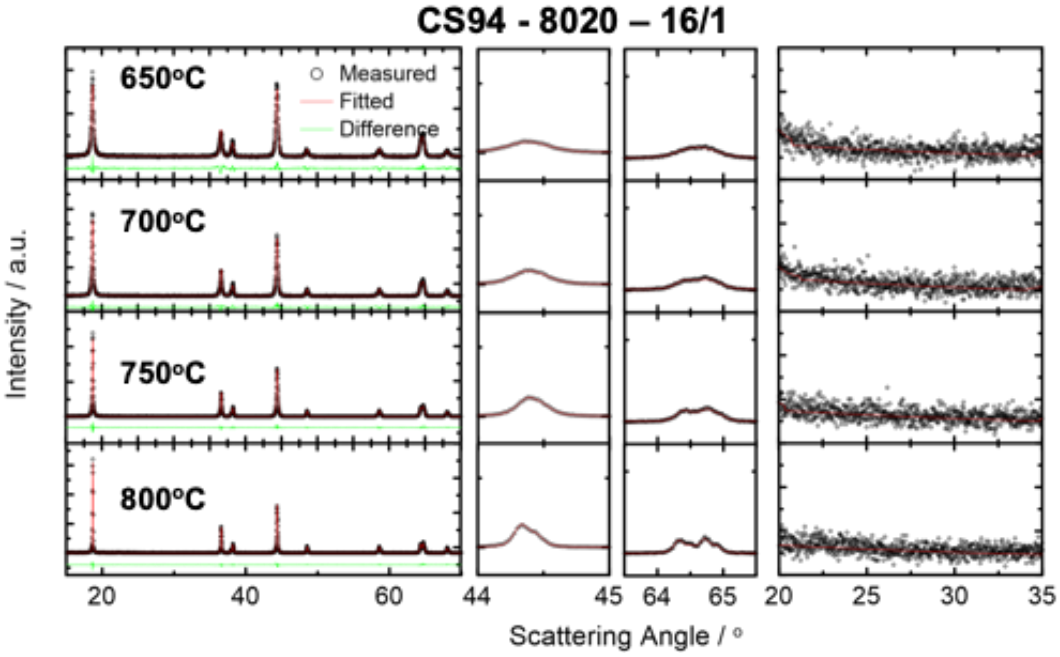
CS94 - 8020 – 16/1
650°C
700°C
750°C
800°C
Measured
Fitted
Difference
Intensity / a.u.
20
40
60
44
45
64
65
20
25
30
35
Scattering Angle / °

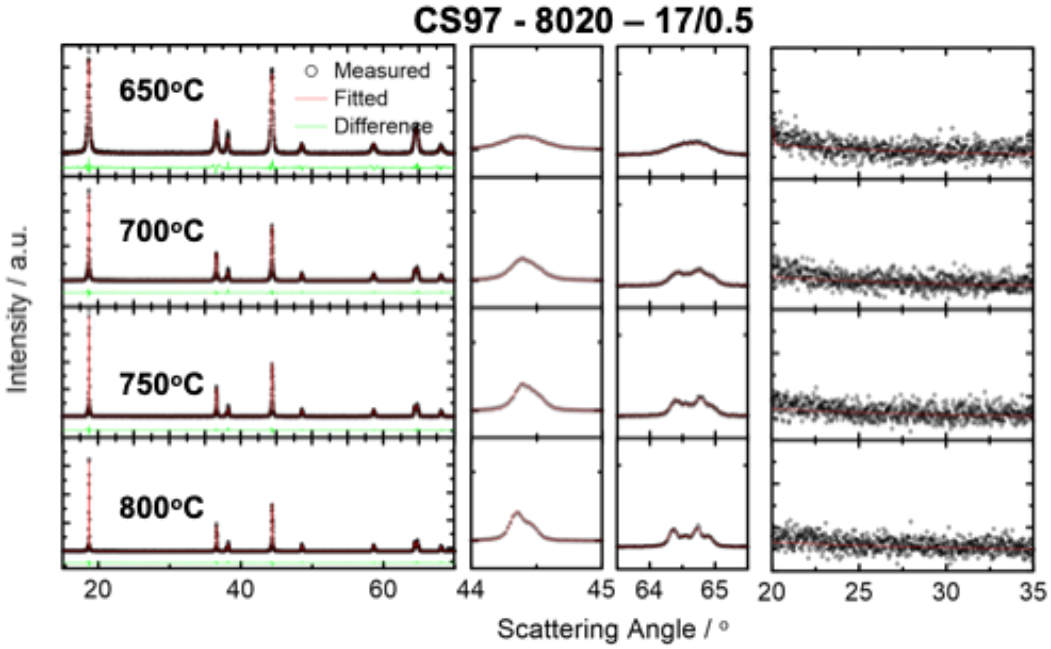
CS97 - 8020 – 17/0.5
650°C
700°C
750°C
800°C
Measured
Fitted
Difference
Intensity / a.u.
Scattering Angle / °

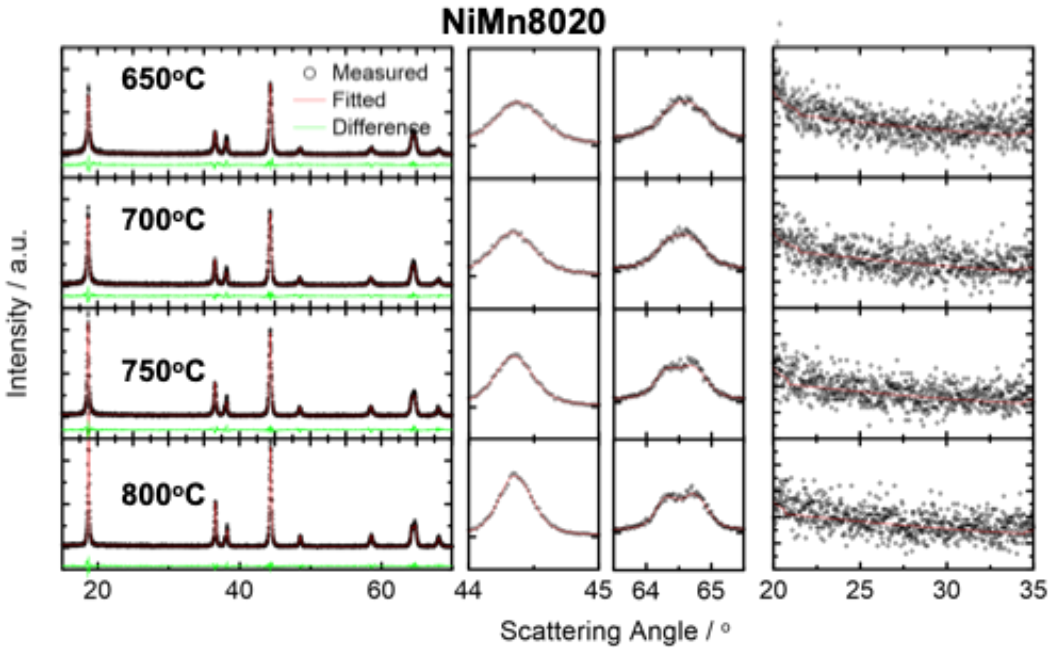
NiMn8020
650°C
700°C
750°C
800°C
Measured
Fitted
Difference
Intensity / a.u.
Scattering Angle / °

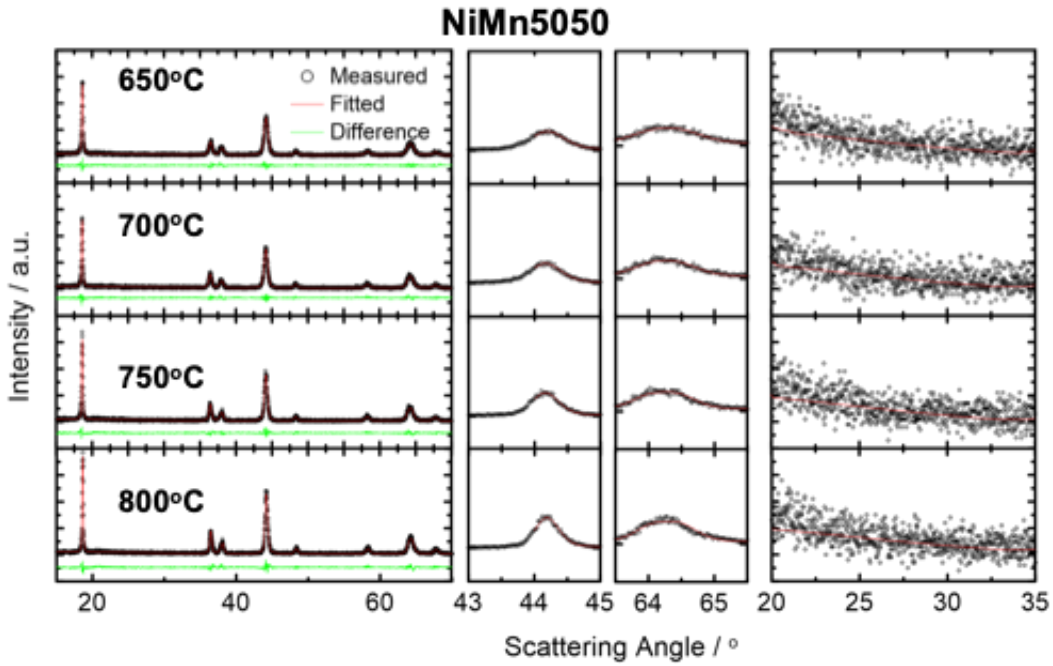

Figure A.1 Rietveld-refined XRD patterns of all lithiated materials. From left to right column: full XRD pattern from 15° to 70°, the corresponding expanded views of (104) Bragg peak, and (108)/(110) Bragg peaks, and the impurity region. "Shell" materials $LiNi_{0.8}Mn_{0.2}O_2$ and $LiNi_{0.5}Mn_{0.5}O_2$ are denoted as NiMn8020 and NiMn5050, respectively.

Table A.1 Specific capacities of the first 2 cycles (C/20) and 1st cycle irreversible capacity of CS92 – 5050 – 17/0.5 lithiated at each temperature. (1) and (2) refer to a pair cell #1 and #2.

mAh/g	1st Charge		1st Discharge		2nd Charge		2nd Discharge		1st Irreversible	
°C	(1)	(2)	(1)	(2)	(1)	(2)	(1)	(2)	(1)	(2)
800	241	240	214	213	217	217	208*	206*	27	27
750	216	215	175	174	172	171	180	178	41	42
700	209	208	144	143	140	136	141	137	65	65
650	184	202	126	133	127	134	127	133	58	70

* 2nd C/20 discharge was interrupted by power outage. 3rd discharge (C/5) is reported herein.

Table A.2 Specific capacities of the first 2 cycles (C/20) and 1st cycle irreversible capacity of CS94 – 8020 – 16/1 lithiated at each temperature. (1) and (2) refer to a pair cell #1 and #2.

mAh/g	1st Charge		1st Discharge		2nd Charge		2nd Discharge		1st Irreversible	
°C	(1)	(2)	(1)	(2)	(1)	(2)	(1)	(2)	(1)	(2)
800	246	247	226	225	228	227	213*	211*	20	22
750	233	241	208	214	205	215	219	223	25	27
700	221	220	180	179	181	176	184	178	41	40
650	209	204	153	152	159	157	164	162	56	52

* 2nd C/20 discharge was interrupted by power outage. 3rd discharge (C/5) is reported herein.

Table A.3 Specific capacities of the first 2 cycles (C/20) and 1st cycle irreversible capacity of CS97 – 8020 – 17/0.5 lithiated at each temperature. (1) and (2) refer to a pair cell #1 and #2.

mAh/g / °C	1st Charge		1st Discharge		2nd Charge		2nd Discharge		1st Irreversible	
	(1)	(2)	(1)	(2)	(1)	(2)	(1)	(2)	(1)	(2)
800	254	253	232	230	232	230	230	206*	22	22
750	246	246	241	242	235	235	242	242	5	5
700	239	239	201	202	205	203	211	208	38	38
650	223	209	178	156	181	158	185	161	45	53

*2nd C/20 discharge was interrupted by power outage. 3rd discharge (C/5) is reported herein.

Table A.4 Specific capacities of the first 2 cycles (C/20) and 1st cycle irreversible capacity of $LiNi_{0.8}Mn_{0.2}O_2$ lithiated at each temperature. (1) and (2) refer to a pair cell #1 and #2.

mAh/g / °C	1st Charge		1st Discharge		2nd Charge		2nd Discharge		1st Irreversible	
	(1)	(2)	(1)	(2)	(1)	(2)	(1)	(2)	(1)	(2)
800	211	210	181	179	183	181	182	180	30	30
750	206	208	176	178	177	179	176	178	30	30
700	200	201	170	171	171	173	170	172	30	30
650	194	193	164	162	165	163	165	162	30	31

Table A.5 Specific capacities of the first 2 cycles (C/20) and 1st cycle irreversible capacity of $LiNi_{0.5}Mn_{0.5}O_2$ lithiated at each temperature. (1) and (2) refer to a pair cell #1 and #2.

mAh/g / °C	1st Charge		1st Discharge		2nd Charge		2nd Discharge		1st Irreversible	
	(1)	(2)	(1)	(2)	(1)	(2)	(1)	(2)	(1)	(2)
800	158	157	138	136	140	137	139	138	20	21
750	154	154	133	132	135	133	135	133	21	22
700	153	153	137	138	139	140	139	139	16	15
650	150	149	133	132	134	134	134	133	17	17

Appendix B

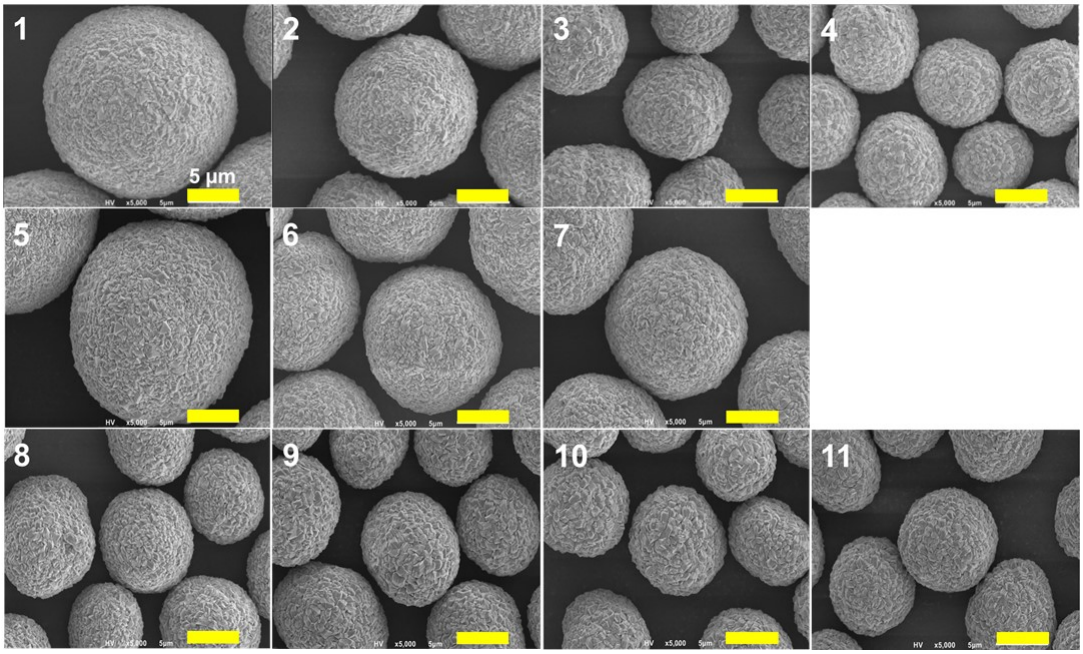

Figure B.1 SEM images of precursors #1 to 11. Scale bar is 5 µm

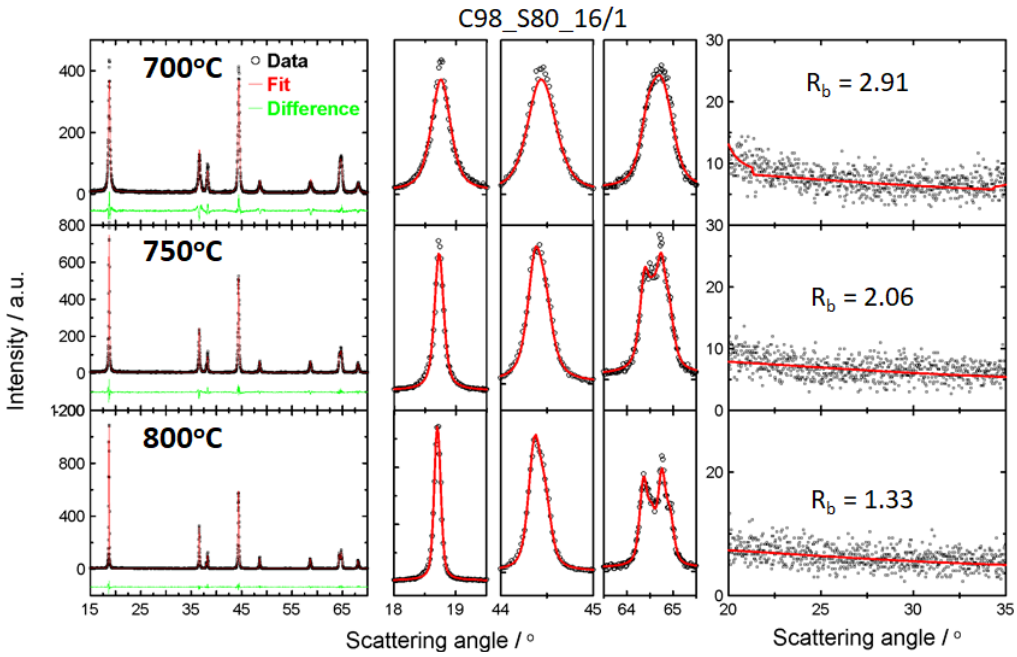
C98_S80_16/1
700°C
Data
Fit
Difference
750°C
800°C
Intensity / a.u.
Scattering angle / °
Scattering angle / °
R_b = 2.91
R_b = 2.06
R_b = 1.33

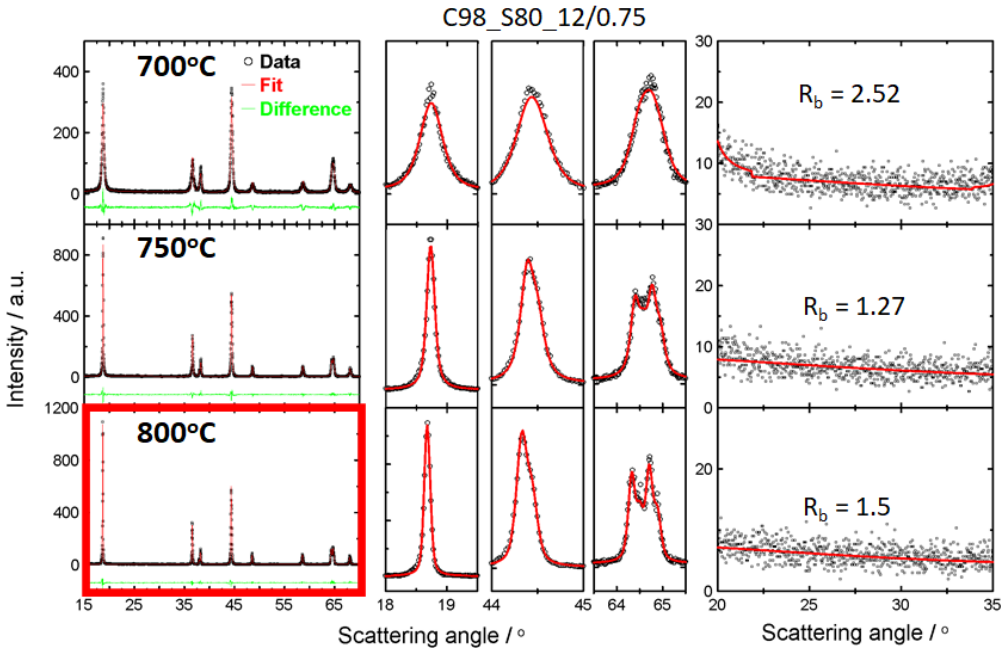
C98_S80_12/0.75
700°C
Data
Fit
Difference
750°C
800°C
Intensity / a.u.
Scattering angle / °
Scattering angle / °
R_b = 2.52
R_b = 1.27
R_b = 1.5

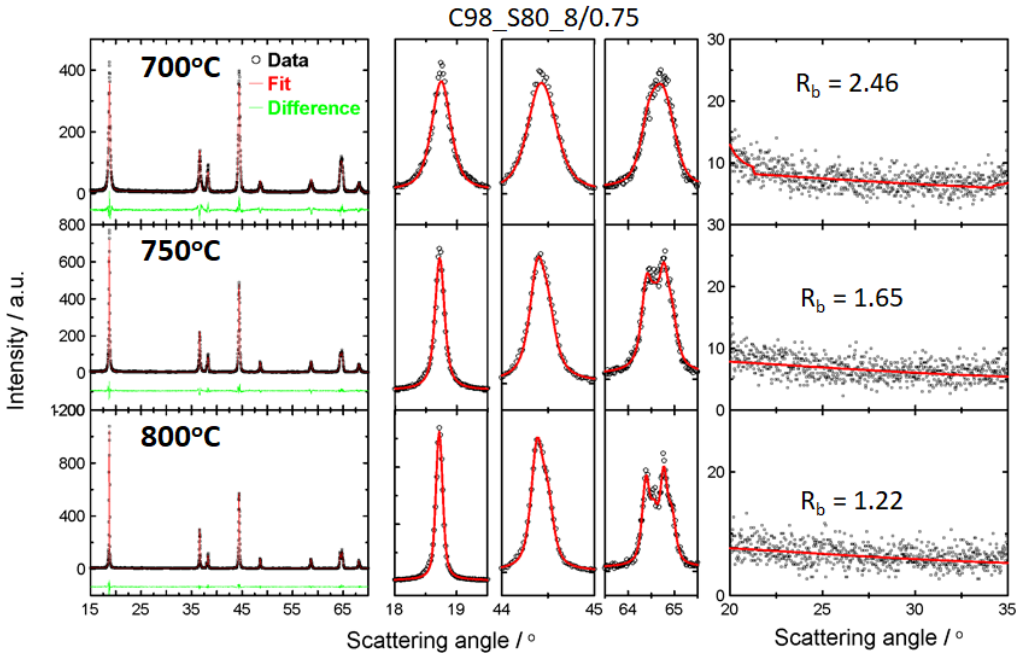
C98_S80_8/0.75
700°C
Data
Fit
Difference
750°C
800°C
Intensity / a.u.
Scattering angle / °
R_b = 2.46
R_b = 1.65
R_b = 1.22

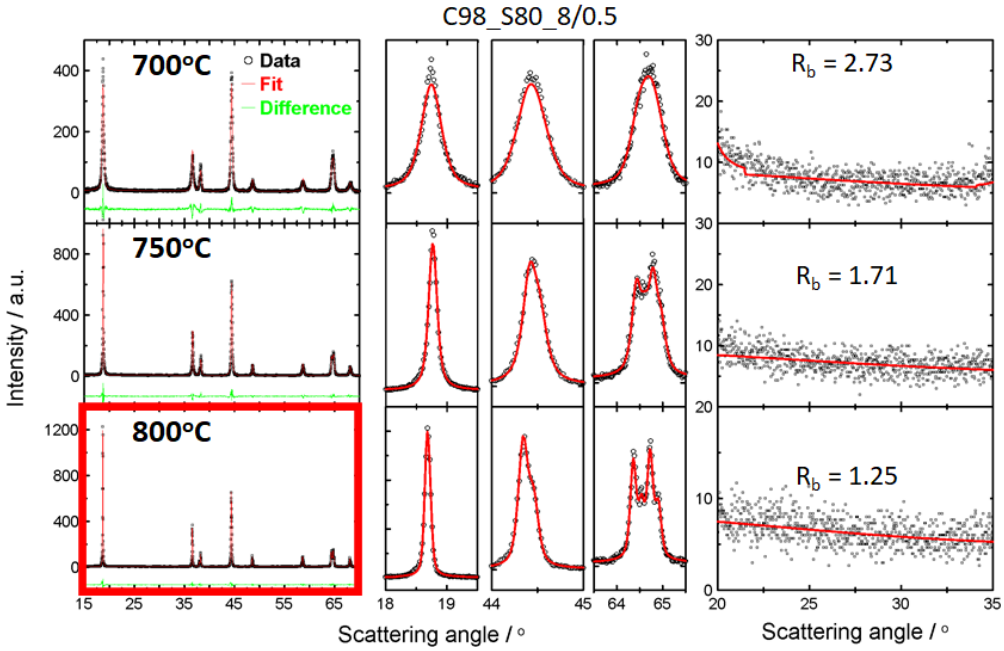
C98_S80_8/0.5
700°C
Data
Fit
Difference
750°C
800°C
Intensity / a.u.
Scattering angle / °
R_b = 2.73
R_b = 1.71
R_b = 1.25

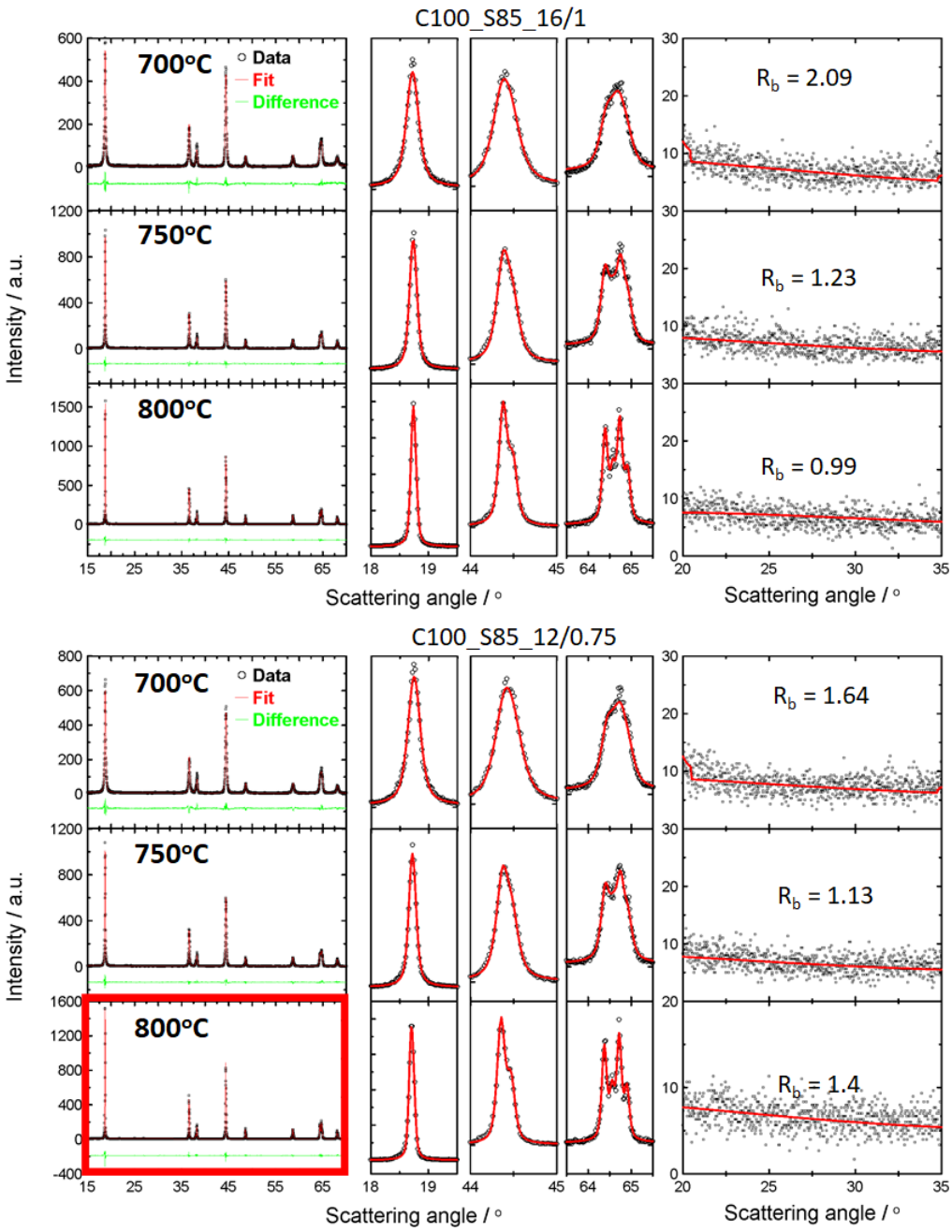
C100_S85_16/1
700°C
Data
Fit
Difference
750°C
800°C
R_b = 2.09
R_b = 1.23
R_b = 0.99
Intensity / a.u.
Scattering angle / °
C100_S85_12/0.75
700°C
Data
Fit
Difference
750°C
800°C
R_b = 1.64
R_b = 1.13
R_b = 1.4
Intensity / a.u.
Scattering angle / °

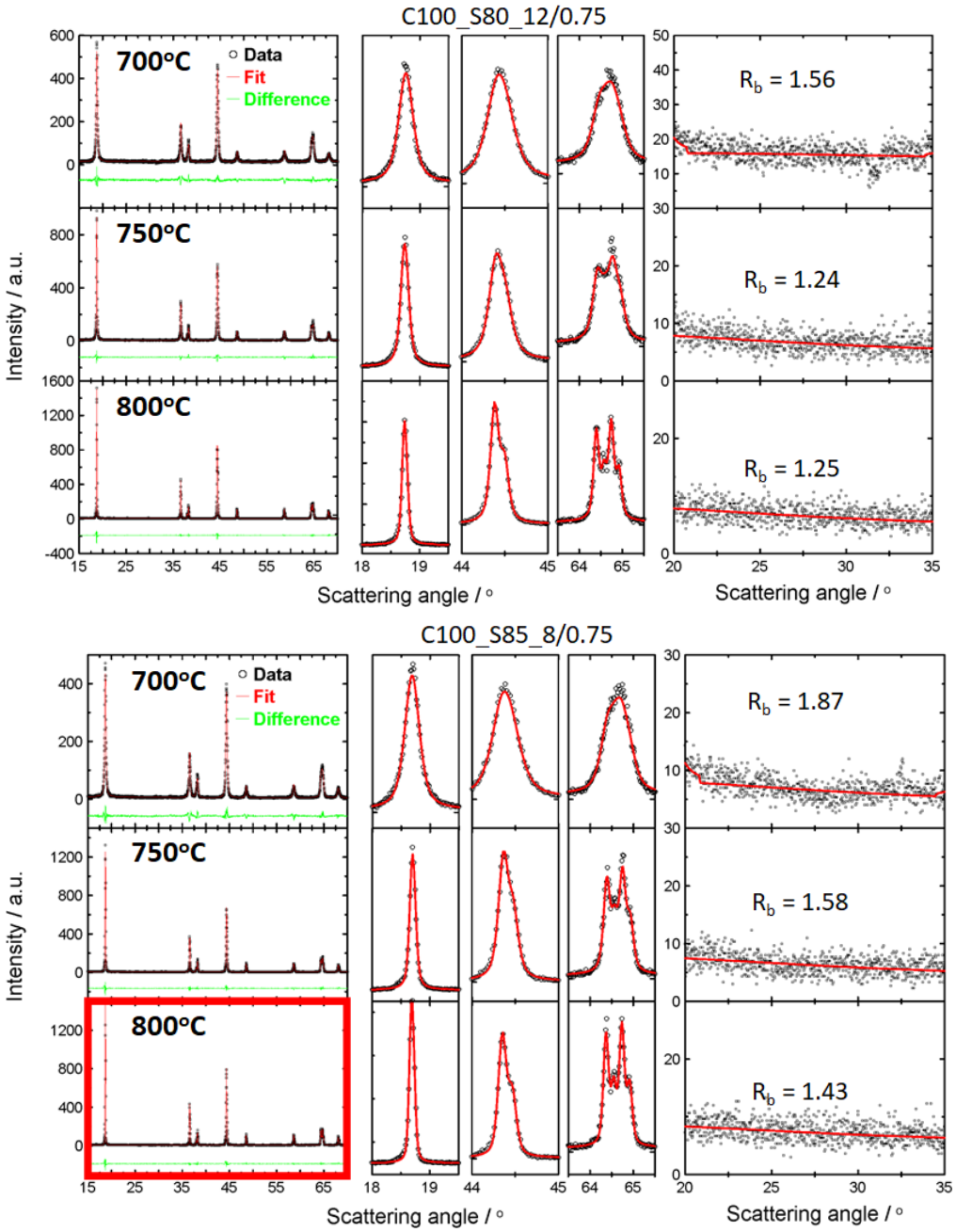
C100_S80_12/0.75
700°C
Data
Fit
Difference
750°C
800°C
Intensity / a.u.
Scattering angle / °
R_b = 1.56
R_b = 1.24
R_b = 1.25
C100_S85_8/0.75
700°C
Data
Fit
Difference
750°C
800°C
Intensity / a.u.
Scattering angle / °
R_b = 1.87
R_b = 1.58
R_b = 1.43

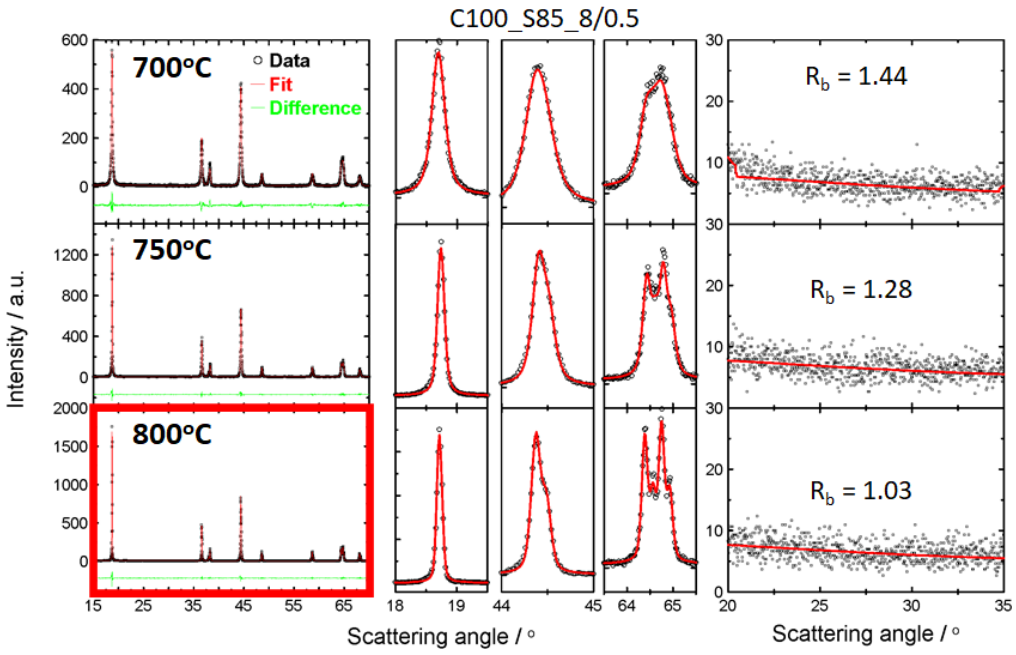
C100_S85_8/0.5
700°C
Data
Fit
Difference
750°C
800°C
Intensity / a.u.
Scattering angle / °
R_b = 1.44
R_b = 1.28
R_b = 1.03
Scattering angle / °

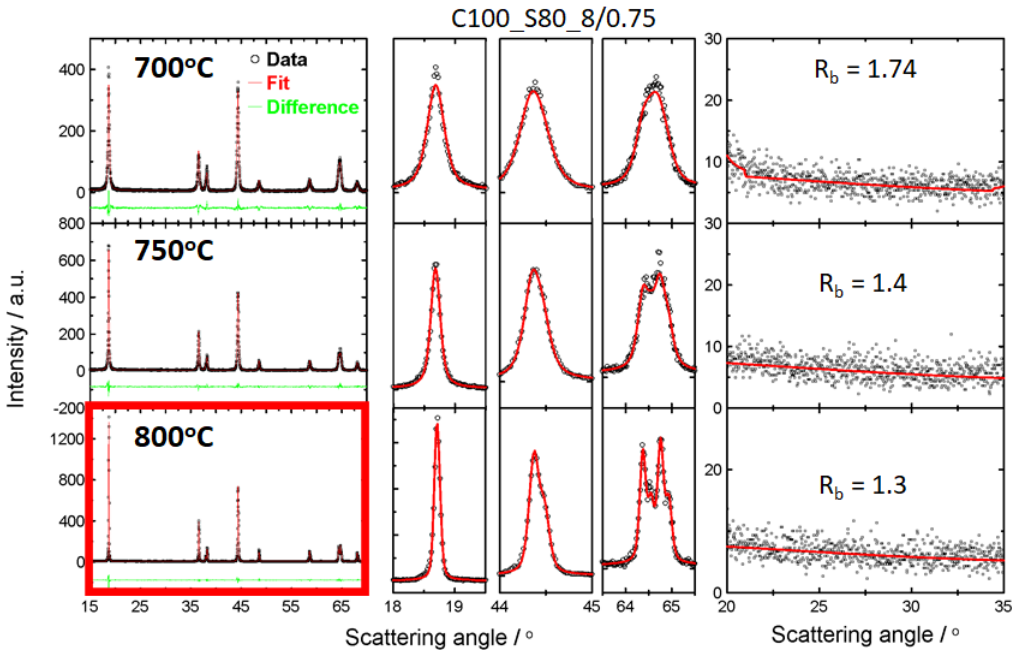
C100_S80_8/0.75
700°C
Data
Fit
Difference
750°C
800°C
Intensity / a.u.
Scattering angle / °
R_b = 1.74
R_b = 1.4
R_b = 1.3
Scattering angle / °

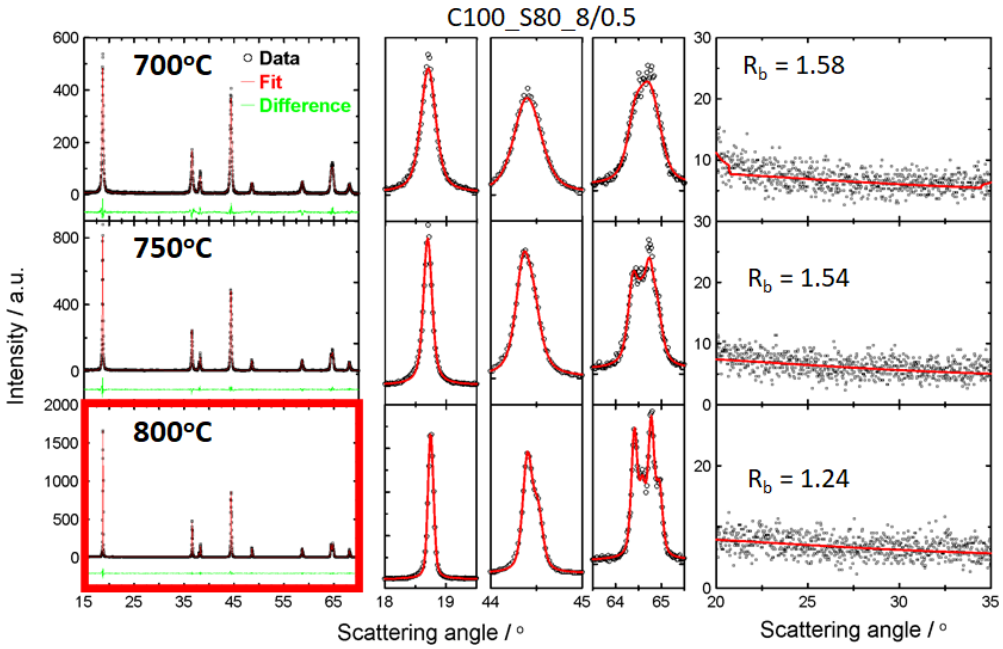

Figure B.2 XRD patterns of precursors #1 to 11 heated with LiOH•H_2O at 700°C to 800°C. The quality of fit (Bragg R) is shown. The red enclosed XRD patterns are no longer core-shell materials as a result of Mn interdiffusion.

Table B.1 Specific capacities of the first 2 cycles (C/20) and 1st cycle irreversible capacity of C98_S80_16/1 lithiated at each temperature. (1) and (2) refer to a pair cell #1 and #2.

mAh/g / °C	1st Charge		1st Discharge		2nd Charge		2nd Discharge		1st Irreversible	
	(1)	(2)	(1)	(2)	(1)	(2)	(1)	(2)	(1)	(2)
800	239	237	215	215	215	214	222	221	23	22
750	231	230	205	204	205	204	212	211	27	25
725	222	226	187	190	187	190	190	193	35	36
700	217	216	183	181	184	182	188	187	34	35

Note: 2nd C/20 discharge was interrupted by power outage. 3rd discharge (C/5) is reported herein.

Table B.2 Specific capacities of the first 2 cycles (C/20) and 1st cycle irreversible capacity of C98_S80_12/0.75 lithiated at each temperature. (1) and (2) refer to a pair cell #1 and #2.

mAh/g / °C	1st Charge		1st Discharge		2nd Charge		2nd Discharge		1st Irreversible	
	(1)	(2)	(1)	(2)	(1)	(2)	(1)	(2)	(1)	(2)
800*	238	239	214	215	215	217	217	218	24	24
750	234	233	206	206	204	206	211	212	28	27
725	224	225	189	192	189	191	194	196	36	33
700	212	215	176	182	174	182	180	188	36	32

* This is no longer core-shell material as a result of Mn interdiffusion.

Table B.3 Specific capacities of the first 2 cycles (C/20) and 1st cycle irreversible capacity of C98_S80_8/0.75 lithiated at each temperature. (1) and (2) refer to a pair cell #1 and #2.

mAh/g / °C	1st Charge		1st Discharge		2nd Charge		2nd Discharge		1st Irreversible	
	(1)	(2)	(1)	(2)	(1)	(2)	(1)	(2)	(1)	(2)
800	233	234	214	215	214	214	219	219	19	19
750	227	228	204	206	200	203	204	207	23	22
725	217	220	177	177	177	177	179	181	40	43
700	218	218	190	194	190	194	197	200	28	25

Table B.4 Specific capacities of the first 2 cycles (C/20) and 1st cycle irreversible capacity of C98_S80_8/0.5 lithiated at each temperature. (1) and (2) refer to a pair cell #1 and #2.

mAh/g / °C	1st Charge		1st Discharge		2nd Charge		2nd Discharge		1st Irreversible	
	(1)	(2)	(1)	(2)	(1)	(2)	(1)	(2)	(1)	(2)
800*	237	237	215	215	216	215	216	214.8	21	22
750	233	234	212	212	211	213	217	217.2	21	21
725	225	226	185	189	184	188	188	191.4	40	37
700	217	219	188	187	188	189	196	190.6	28	32

* This is no longer core-shell material as a result of Mn interdiffusion.

Table B.5 Specific capacities of the first 2 cycles (C/20) and 1st cycle irreversible capacity of C100_S85_16/1 lithiated at each temperature. (1) and (2) refer to a pair cell #1 and #2.

mAh/g / °C	1st Charge		1st Discharge		2nd Charge		2nd Discharge		1st Irreversible	
	(1)	(2)	(1)	(2)	(1)	(2)	(1)	(2)	(1)	(2)
800	235	253	212	227	212	225	215	225	23	25
750	237	239	205	207	206	208	211	215	33	33
725	228	223	192	180	195	185	205	196	36	43
700	214		145		146		147		69	

Note: 2nd C/20 discharge was interrupted by power outage. 3rd discharge (C/5) is reported herein.

Table B.6 Specific capacities of the first 2 cycles (C/20) and 1st cycle irreversible capacity of C100_S85_12/0.75 lithiated at each temperature. (1) and (2) refer to a pair cell #1 and #2.

mAh/g / °C	1st Charge		1st Discharge		2nd Charge		2nd Discharge		1st Irreversible	
	(1)	(2)	(1)	(2)	(1)	(2)	(1)	(2)	(1)	(2)
800*	249	249	227	228	226	228	227	228	23	21
750	242	243	214	217	213	219	216	223	28	27
725	226		197		200		210		29	
700	215	220	158	167	160	169	164	175	57	53

* This is no longer core-shell material as a result of Mn interdiffusion.

Table B.7 Specific capacities of the first 2 cycles (C/20) and 1st cycle irreversible capacity of C100_S80_12/0.75 lithiated at each temperature. (1) and (2) refer to a pair cell #1 and #2.

mAh/g / °C	1st Charge		1st Discharge		2nd Charge		2nd Discharge		1st Irreversible	
	(1)	(2)	(1)	(2)	(1)	(2)	(1)	(2)	(1)	(2)
800	245	244	225	225	226	225	220	226	19	19
750	238	240	210	211	210	209	215	213	29	29
725	227	228	193	192	195	195	203	202	34	36
700	221	222	175	177	176	179	181	183	46	46

Table B.8 Specific capacities of the first 2 cycles (C/20) and 1st cycle irreversible capacity of C100_S80_8/0.5 lithiated at each temperature. (1) and (2) refer to a pair cell #1 and #2.

mAh/g / °C	1st Charge		1st Discharge		2nd Charge		2nd Discharge		1st Irreversible	
	(1)	(2)	(1)	(2)	(1)	(2)	(1)	(2)	(1)	(2)
800*	241	240	224	223	222	221	225	223	17	18
750	239	238	222	222	221	220	224	224	18	16
700	227	227	200	194	201	198	177	161	27	34

* This is no longer core-shell material as a result of Mn interdiffusion.
Note: 2nd C/20 discharge was interrupted by power outage. 3rd discharge (C/5) is reported herein.

Table B.9 Specific capacities of the first 2 cycles (C/20) and 1st cycle irreversible capacity of C100_S80_8/0.75 lithiated at each temperature. (1) and (2) refer to a pair cell #1 and #2.

mAh/g / °C	1st Charge		1st Discharge		2nd Charge		2nd Discharge		1st Irreversible	
	(1)	(2)	(1)	(2)	(1)	(2)	(1)	(2)	(1)	(2)
800*	237	236	220	219	219	215	222	218	17	17
750	232	234	212	212	211	211	216	217	20	22
700	220	221	188	198	189	196	120	145	32	23

* This is no longer core-shell material as a result of Mn interdiffusion.

Table B.10 Specific capacities of the first 2 cycles (C/20) and 1st cycle irreversible capacity of C100_S85_8/0.5 lithiated at each temperature. (1) and (2) refer to a pair cell #1 and #2.

mAh/g / °C	1st Charge		1st Discharge		2nd Charge		2nd Discharge		1st Irreversible	
	(1)	(2)	(1)	(2)	(1)	(2)	(1)	(2)	(1)	(2)
800*	240	244	221	225	217	222	220	223	18	19
750	244	246	230	232	229	232	234	235	14	14
700	232	231	207	208	207	208	202	207	25	23

* This is no longer core-shell material as a result of Mn interdiffusion.

Table B.11 Specific capacities of the first 2 cycles (C/20) and 1st cycle irreversible capacity of C100_S85_8/0.75 lithiated at each temperature. (1) and (2) refer to a pair cell #1 and #2.

mAh/g / °C	1st Charge		1st Discharge		2nd Charge		2nd Discharge		1st Irreversible	
	(1)	(2)	(1)	(2)	(1)	(2)	(1)	(2)	(1)	(2)
800*	247	245	230	228	228	225	229	228	17	17
750	244	244	229	227	228	227	234	234	16	16
700	223	221	182	181	181	177	111	173	41	40

* This is no longer core-shell material as a result of Mn interdiffusion.

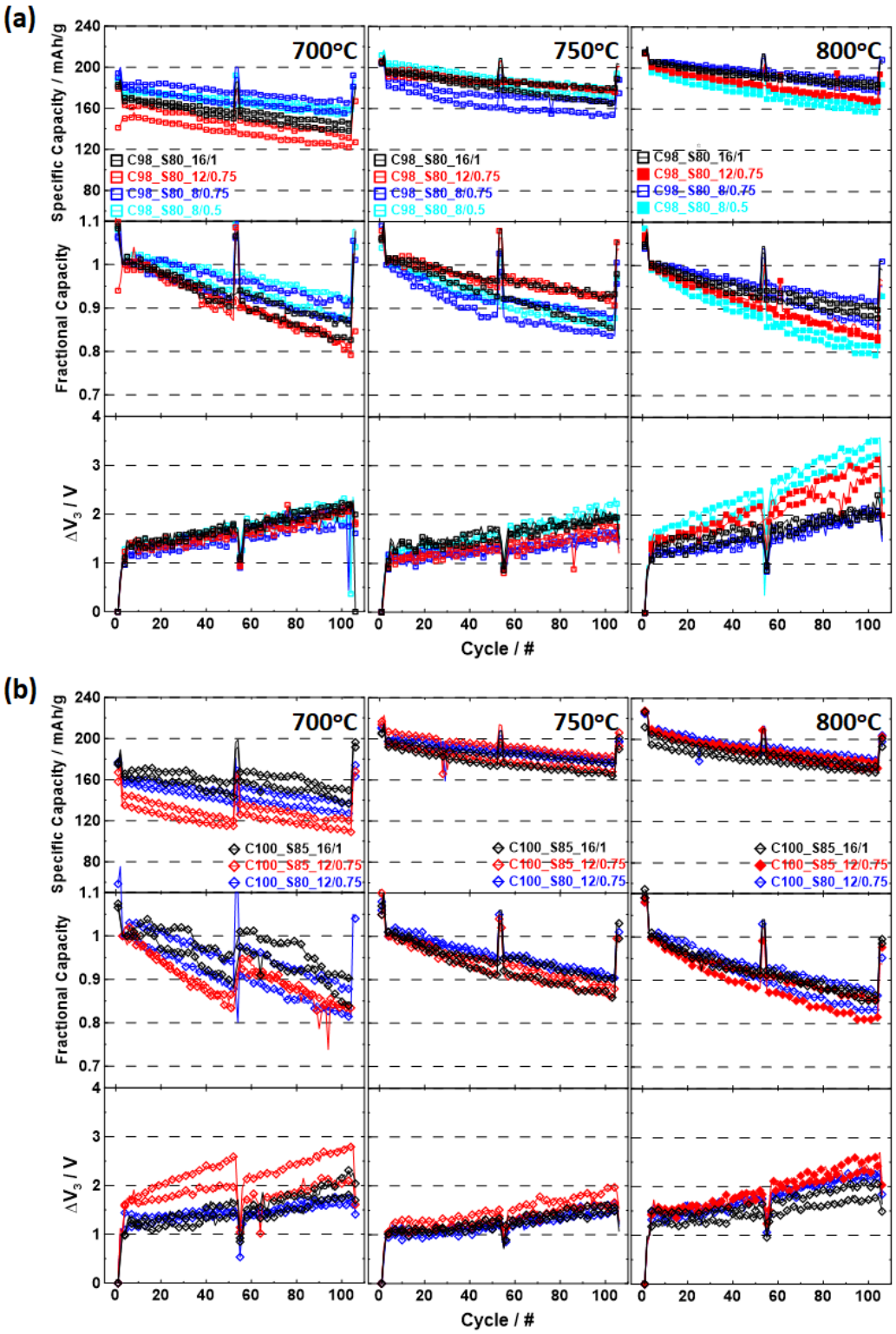
(a)
700°C
750°C
800°C
Specific Capacity / mAh/g
Fractional Capacity
ΔV3 / V
Cycle / #
C98_S80_16/1
C98_S80_12/0.75
C98_S80_8/0.75
C98_S80_8/0.5
(b)
700°C
750°C
800°C
Specific Capacity / mAh/g
Fractional Capacity
ΔV3 / V
Cycle / #
C100_S85_16/1
C100_S85_12/0.75
C100_S80_12/0.75

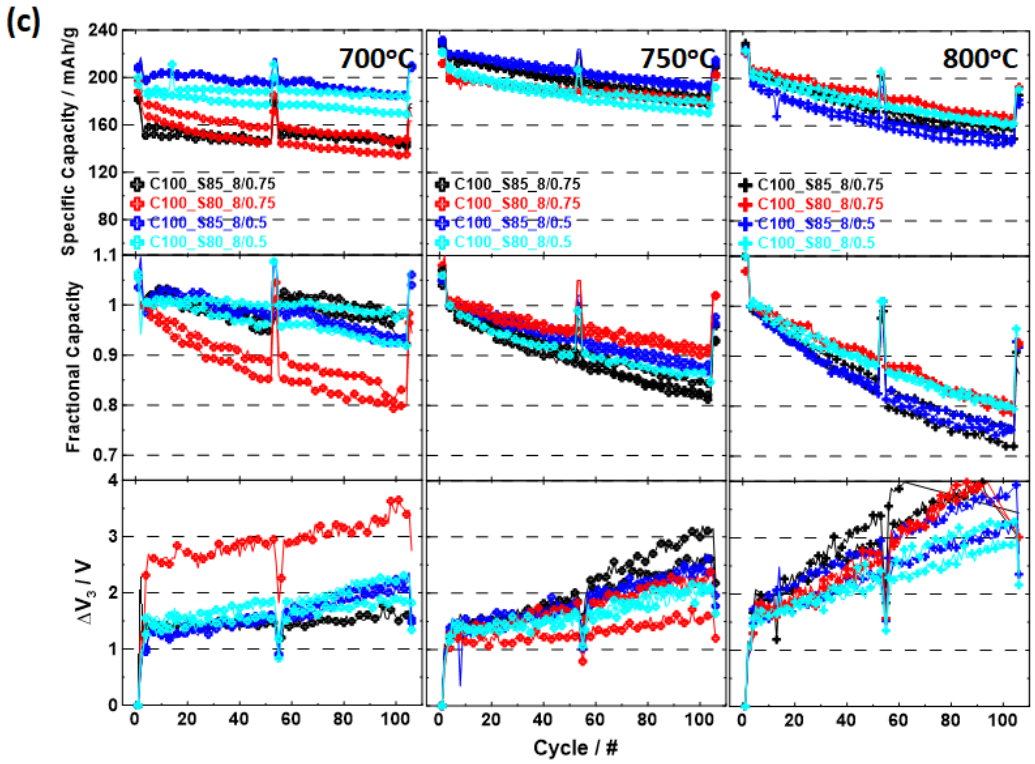

Figure B.3 The specific capacity, fractional capacity and normalized voltage polarization (ΔV_3) for samples synthesized at 700ºC, 750ºC and 800ºC. Group I (a) to Group III (c) materials were tested at 30ºC to 4.3 V vs. Li/Li^+. The 1st C/5 discharge (3rd discharge) is taken as 100% in the fractional capacity plots. The ΔV of the 1st C/5 cycle (3rd cycle) is taken as 100%. Hollow symbols denote core-shell materials. Solid symbols denote homogenous samples due to Mn interdiffusion.

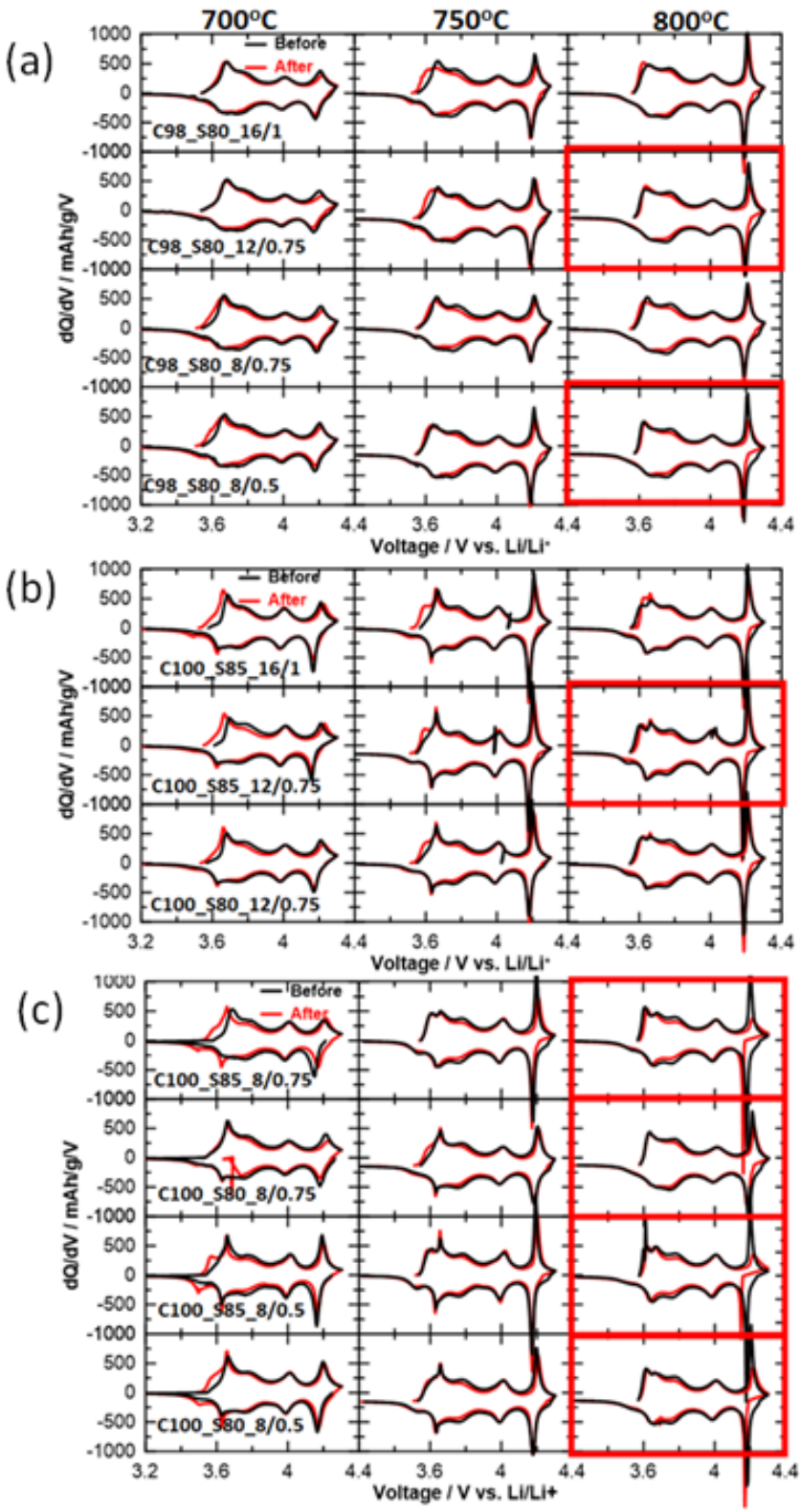

Figure B.4 The C/20 dQ/dV vs V evolution from before (2nd cycle) to after (105th cycle) cycling for Group I (a) to Group III (c) materials at 700°C, 750°C and 800°C. The red enclosed plots are not core-shell materials.

Appendix C

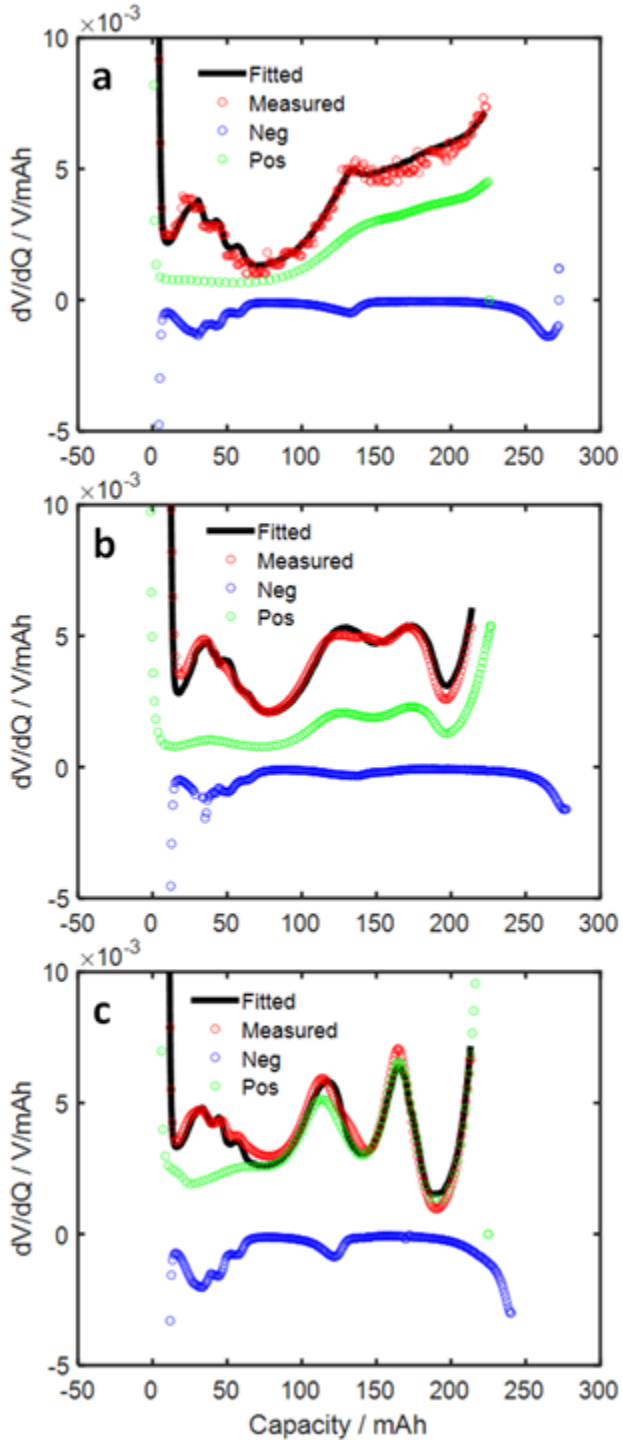

Figure C.1 The goodness-of-fit of the dV/dQ method for cell balancing. a) SC532/graphite cells; b) SC811/graphite cells; c) Ni94/graphite cells.

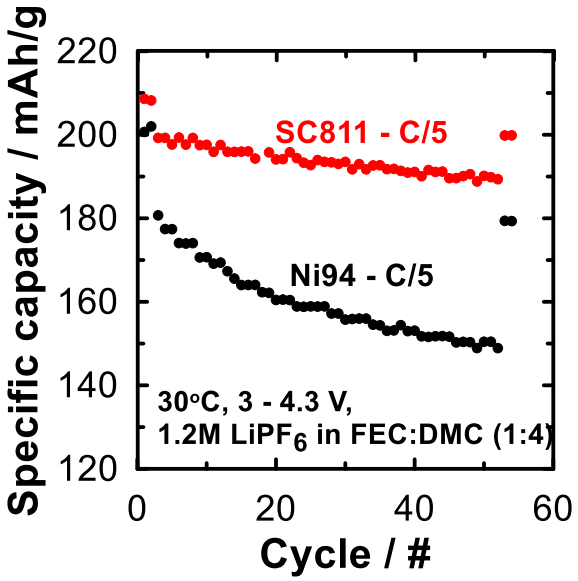

Figure C.2 The core-shell Ni94 and the SC811 cycled from 3 to 4.3 V vs. Li/Li^+ in coin cell half-cells at 30°C. The first 2 cycles are C/20 cycles followed by 50 cycles of C/5 and 2 cycles of C/20.